





# **The microscopic origin of surface slip: A neutron and x-ray scattering study on the near surface structure of flowing liquids**

**Dissertation zur Erlangung des Grades eines Doktors der Naturwissenschaften in  
der Fakultät für Physik und Astronomie der Ruhr-Universität Bochum**

vorgelegt von

Philipp Gutfreund

aus

Frankfurt am Main

Bochum, den

25. März 2011

1. Gutachter: Prof. Dr. Dr. h. c. H. Zabel

2. Gutachter: Dr. M. Wolff

Tag der Disputation: 23. Mai 2011

# List of Papers

This thesis is based on the following papers which are included in the appendix.

**A Depletion at Solid-Liquid Interfaces: Flowing Hexadecane on Functionalized Surfaces**

P. Gutfreund, M. Wolff, M. Maccarini, S. Gerth, J. F. Ankner, J. Browning, C. E. Halbert, H. Wacklin, and H. Zabel

*Journal of Chemical Physics* **134**, 64711 (2011)

**B Surface Correlation Affects Liquid Order and Slip in a Newtonian Liquid**

P. Gutfreund, O. Bäumchen, D. van der Grinten, R. Fetzer, M. Maccarini, K. Jacobs, H. Zabel, and M. Wolff

*submitted to Physical Review Letters*

**C Shear Induced Relaxation of Polymer Micelles at the Solid-Liquid Interface**

M. Wolff, R. Steitz, P. Gutfreund, N. Voss, S. Gerth, M. Walz, A. Magerl, and H. Zabel

*Langmuir* **24**, 11331-11333 (2008)

**D Nanoscale Discontinuities at the Boundary of Flowing Liquids: A Look into Structure**

M. Wolff, P. Gutfreund, A. Rühm, B. Akgun, and H. Zabel

*Journal of Physics: Condensed Matter*, **23**, 184102 (2011)



# Contents

<b>1. Introduction</b>	<b>7</b>
1.1. Motivation . . . . .	7
1.2. Classical hydrodynamics and surface slip . . . . .	7
1.2.1. Classical hydrodynamics . . . . .	7
1.2.2. Rheology . . . . .	10
1.2.3. Surface Slip . . . . .	12
1.3. X-ray and neutron scattering . . . . .	15
1.3.1. X-ray radiation . . . . .	15
1.3.2. Neutron radiation . . . . .	17
1.3.3. Scattering theory . . . . .	19
1.3.4. Reflectometry and Grazing Incidence Diffraction . . . . .	28
<b>2. Experimental</b>	<b>41</b>
2.1. Experimental considerations . . . . .	41
2.1.1. Resolution . . . . .	41
2.1.2. Data correction . . . . .	43
2.1.3. Data fitting . . . . .	45
2.2. Angle dispersive reflectometers . . . . .	47
2.2.1. Beamline BL9 . . . . .	47
2.2.2. ADAM . . . . .	48
2.2.3. V6 Horizontal Reflectometer . . . . .	48
2.2.4. N-Rex <sup>+</sup> . . . . .	50
2.3. Time-of-flight reflectometers . . . . .	50
2.3.1. FIGARO . . . . .	51
2.3.2. Liquids Reflectometer . . . . .	54
2.4. Comparison of the neutron reflectometers . . . . .	54
2.5. Laboratory reflectometers . . . . .	57
2.6. Contact angle measurements . . . . .	57
<b>3. Results and Discussion</b>	<b>59</b>
3.1. Hexadecane on functionalized surfaces . . . . .	59
3.2. Polystyrene on silanized surfaces . . . . .	60
3.3. Complex Liquid . . . . .	61
3.4. First GID experiments on crystalline hexadecane . . . . .	61

<b>4. Conclusion and Summary</b>	<b>63</b>
4.1. Conclusion . . . . .	63
4.2. Summary . . . . .	64
<b>5. Outlook</b>	<b>65</b>
5.1. Depletion layer . . . . .	65
5.2. Thin polymer films . . . . .	65
5.3. <i>In situ</i> rheometry . . . . .	66
<b>6. Zusammenfassung</b>	<b>67</b>
<b>Bibliography</b>	<b>69</b>
<b>A. Depletion at Solid-Liquid Interfaces: Flowing Hexadecane on Functionalized Surfaces</b>	<b>77</b>
<b>B. Surface Correlation Affects Liquid Order and Slip in a Newtonian Liquid</b>	<b>87</b>
<b>C. Shear Induced Relaxation of Polymer Micelles at the Solid-Liquid Interface</b>	<b>93</b>
<b>D. Nanoscale Discontinuities at the Boundary of Flowing Liquids: A Look into Structure</b>	<b>97</b>
<b>Acknowledgments</b>	<b>107</b>
<b>Curriculum Vitæ</b>	<b>109</b>

# 1. Introduction

## 1.1. Motivation

When downsizing technology, confinement and interface effects grow enormously in importance. Especially in the context of microfluidic devices [1], surface induced effects, such as friction, may dramatically impact hydrodynamics in these systems. The controlled motion of microscopic amounts of liquid open completely new perspectives for research as well as for applications, like e.g. lab-on-chip devices [2] in pharmaceuticals, chemistry or the food industry. But also from a scientific point of view, the solid/liquid boundary of flowing liquids has further highly interesting properties. Shear impinges anisotropy to a liquid and may induce inhomogeneities, which may have their origin close to the solid interface. In the last twenty years the classical boundary condition (BC) of flowing liquids, assuming the molecules in contact to a solid boundary to be stationary relatively to the solid, has been revised on a microscopic length scale due to numerous reports on surface slip in simple liquids [3, 4]. Today it is accepted that slippage of liquids on smooth homogeneous non-wetting surfaces may lead to deviations from classical hydrodynamics on a nanometer length scale. Nevertheless, the microscopic origin of surface slip in newtonian liquids remains unclear, also hindered by the fact that most experimental techniques used to determine microscopic slippage are invasive or indirect. The present work is intended to further proceed in the understanding of the BC at liquid/solid interfaces by resolving the interfacial structure of some prominent cases of slipping liquids with non-disturbing neutron and x-ray scattering techniques.

## 1.2. Classical hydrodynamics and surface slip

### 1.2.1. Classical hydrodynamics

The mechanics of fluids can be described by considering the liquid as a continuum and by calculating the macroscopic properties of an infinite ensemble of microscopic particles, i.e. molecules or atoms [5]. Accordingly, mechanical properties like the velocity  $\vec{v}(\vec{r}, t)$  do not correspond to distinct particles, but to the ensemble of fluid particles. Furthermore, one can use thermodynamic parameters as the pressure  $\vec{p}(\vec{r}, t)$  and the density  $\rho(\vec{r}, t)$  to describe the given system. In the course of this section an infinitesimal volume element  $dV$  is small in comparison with the sample volume, but comprises enough particles to be considered as a continuum.

In analogy to conventional mechanics, some fundamental conservation principles can be adapted, like the conservation of mass. The amount of liquid escaping a sample volume

## 1. Introduction

$V_0$  along the directions  $\vec{n}$  normal to the surface is equivalent to the surface integral

$$\oint_{V_0} \rho \vec{v} d\vec{n}. \quad (1.1)$$

On the other hand, the change of material in the same volume can be described by a density decrease:

$$-\frac{\partial}{\partial t} \int_{V_0} \rho d^3\vec{r}. \quad (1.2)$$

Equalizing these both expressions and transforming the surface integral into a volume integral one finds the following condition:

$$\frac{\partial \rho}{\partial t} + \text{div}(\rho \vec{v}) = 0. \quad (1.3)$$

This is known as the *continuity equation*. If the liquid is supposed to be incompressible this reduces to:

$$\text{div } \vec{v} = 0. \quad (1.4)$$

In order to describe the dynamics of a fluid, one has to calculate the force acting on a sample volume. This can be done by integrating the pressure on its surface:

$$-\oint_{V_0} \vec{p} d\vec{n}, \quad (1.5)$$

which can be transformed into a volume integral:

$$-\int_{V_0} \text{grad } \vec{p} d^3\vec{r}. \quad (1.6)$$

Thus, the force acting on a volume element  $dV$  is  $-\text{grad } \vec{p}$  and, just as in ordinary mechanics, equals the product of the mass density and the acceleration:

$$\rho \frac{d\vec{v}(\vec{r}, t)}{dt} = -\text{grad } \vec{p}(\vec{r}, t). \quad (1.7)$$

It is noted, that in this case the time derivative is absolute and thus it consists of:

$$\frac{d\vec{v}}{dt} = \frac{\partial \vec{v}}{\partial t} + \frac{\partial \vec{v}}{\partial \vec{r}} \frac{d\vec{r}}{dt} = \frac{\partial \vec{v}}{\partial t} + (\vec{v} \nabla) \vec{v}. \quad (1.8)$$

Inserting this into eq. (1.7) one finds:

$$\frac{\partial \vec{v}}{\partial t} + (\vec{v} \nabla) \vec{v} = -\frac{1}{\rho} \text{grad } \vec{p}. \quad (1.9)$$

This describes the dynamics of liquids and is known as the *Euler equation*.

The Euler equation is valid for ideal fluids, which means, that the energy flow in the liquid is reversible. In reality, there is friction between the particles and irreversible

energy dissipation occurs in flowing liquids. Thus, one has to apply a force to deform real liquids, which are called viscous liquids. If one assumes that the friction force is proportional to the velocity of the liquid particles and that the friction coefficient is constant, one can modify the Euler equation, by introducing the *dynamic viscosity*  $\eta$ . By adding an irreversible part to the momentum flow of the liquid one can derive the *Navier-Stokes equation* which has the following form for incompressible fluids [5]:

$$\frac{\partial \vec{v}}{\partial t} + (\vec{v} \nabla) \vec{v} = -\frac{1}{\rho} \text{grad } \vec{p} + \frac{\eta}{\rho} \nabla^2 \vec{v}. \quad (1.10)$$

The quotient of the dynamic viscosity and the density is called *kinematic viscosity*

$$\nu = \frac{\eta}{\rho}. \quad (1.11)$$

An intrinsic property of continua is the parity concerning a change of the absolute dimension, upon condition that the relative proportions stay the same. Thus, assuming that the proportions of the fluid system are known, there is only one parameter needed to define the dimensions of the system. This is the typical length of the system  $l$  perpendicular to the flow direction. In case of stationary flow, the velocity of the fluid does not change with time  $\vec{v}(\vec{r}, t) = \vec{v}(\vec{r})$ . Consequently, one can describe the system at a distinct point  $\vec{r}$  by three parameters, namely the velocity  $v$ , the typical length  $l$  and the kinematic viscosity  $\nu$ . Out of these parameters one can form a dimensionless number called *Reynolds number*  $Re$ :

$$Re = \frac{vl}{\nu}. \quad (1.12)$$

Systems with the same Reynolds number behave similar.

In general the Navier-Stokes equations can be solved for any Reynolds number. However, in some cases the solutions are not analytical and may be unstable. For small Reynolds numbers ( $Re < 1000$  [6]) the Navier-Stokes equation can be simplified and always yields stable solutions. For stationary flow the Navier-Stokes equation is:

$$(\vec{v} \nabla) \vec{v} = -\frac{1}{\rho} \text{grad } \vec{p} + \frac{\eta}{\rho} \nabla^2 \vec{v}. \quad (1.13)$$

If  $Re$  is small, the term  $(\vec{v} \nabla) \vec{v}$  can be neglected in comparison with  $\frac{\eta}{\rho} \nabla^2 \vec{v}$  [5] and eq. (1.13) boils down to:

$$\eta \nabla^2 \vec{v} - \text{grad } \vec{p} = 0. \quad (1.14)$$

Forming of the rotation of this equation yields:

$$\nabla^2 \text{rot } \vec{v} = 0, \quad (1.15)$$

which means that there are no curls present in the flow profile. The flow at small Reynolds numbers is therefore called *laminar*, in contrast to *turbulent* flow, where velocities normal to the flow direction occur.

## 1. Introduction

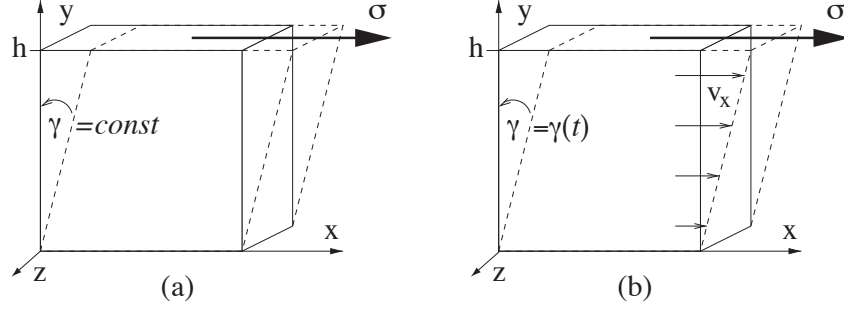


Figure 1.1.: Sketch of a sample enclosed by two plates in the  $xz$ -plane located at  $y = 0$  and  $y = h$ . The lower plate is fixed, whereas the upper plate is forced by a constant stress  $\sigma$  in the  $y$ -direction. For elastic samples this results in a constant deformation angle  $\gamma$  (a) and for viscous liquids in a constant shear rate  $\dot{\gamma}$  (b).

As an example the flow profile of a liquid between two plates separated by the distance  $h$  is shown in fig. 1.1. The upper plate is moved in  $x$ -direction with a velocity  $v_0$  and the lower plate is fixed. If one supposes no pressure change in the  $x$ -direction, all parameters will depend only on  $y$  and eq. (1.14) will give two equations:

$$\frac{dp}{dy} = 0, \quad \frac{d^2v}{dy^2} = 0. \quad (1.16)$$

Consequently, the pressure must be constant:  $p(y) = \text{const.}$ , and the velocity function must be linear:  $v(y) = a * y + b$ . The assumption that the liquid adjacent to the boundaries has the same velocity as the boundary itself, leads to two boundary conditions:

$$v(0) = 0, \quad v(h) = v_0. \quad (1.17)$$

Thus, one can obtain the resulting velocity profile:

$$v(y) = \frac{v_0}{h} * y = \dot{\gamma} * y \quad (1.18)$$

The quotient of the upper plate velocity and the plate distance is called shear rate  $\dot{\gamma}$ .

### 1.2.2. Rheology

The sheared system mentioned above is the simplest form of a rheometry experiment. A shear force is applied to the sample and the response is measured. Due to the definition of the viscosity  $\eta$  in the previous section, it is related to the shear stress  $\sigma$  via [5]:

$$\sigma = \eta \dot{\gamma}. \quad (1.19)$$

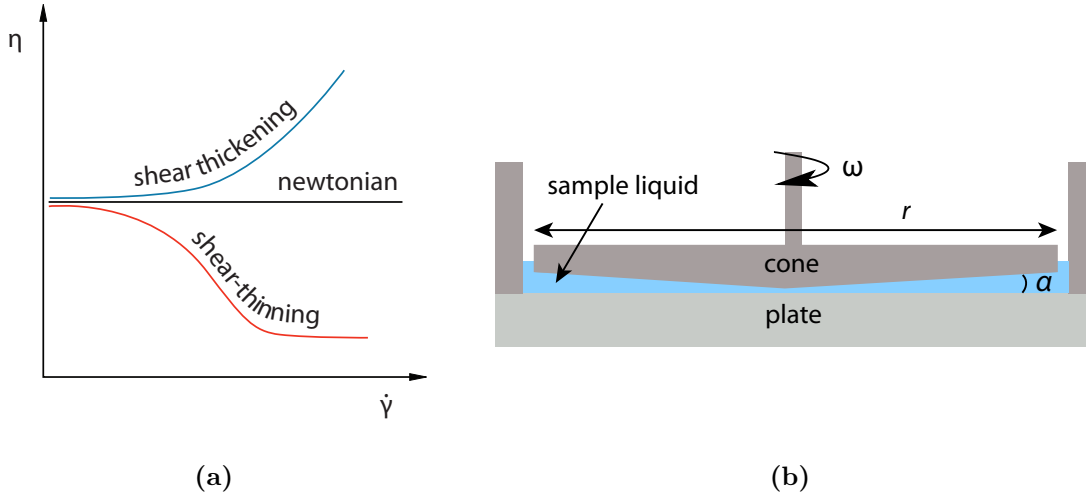


Figure 1.2.: (a) Schematic graph of different viscosity curves. A newtonian liquid shows a constant viscosity, whereas for other liquids the viscosity may depend on the shear rate. (b) Cone-plate geometry in a rheology experiment.

If the viscosity is independent from the shear rate, the liquid is called *newtonian*. In some more complex liquids the viscosity may depend on the shear rate. It is distinguished between shear-thinning and shear thickening as depicted in fig. 1.2(a). The reason for a non-constant viscosity at high shear rates may be a shear-induced structural change within the liquid. Entangled polymer melts are thought to disentangle at a certain shear stress, which leads to shear-thinning. On the other hand, in aqueous starch solutions, for example, the viscosity rises with higher shear rate. At low shear rates the starch particles are surrounded by water, which acts like a lubricant. For higher shear rates the water is not able to fill the gaps anymore and the friction between the particles rises dramatically, which leads to shear thickening.

Several set-ups are possible to measure the viscosity of a liquid. A very simple one is the cone-plate geometry. The liquid is enclosed by a cone and a plate as shown in fig. 1.2(b), which ensures a constant shear rate over the whole gap:

$$\dot{\gamma} = \frac{\omega}{\tan \alpha}, \quad (1.20)$$

with the angular frequency  $\omega$  and the cone angle  $\alpha$ . In the course of this work, cone-plate shear devices were used to provide a constant shear rate, while neutron reflectivity curves were recorded *in situ*. The cone angle used in sec. A is  $\alpha = 1.5^\circ$  with a radius of  $r = 2.5$  cm. The liquid used there is n-hexadecane, which has a kinematic viscosity of  $\nu = 2 * 10^{-6}$  m<sup>2</sup>/s at 60°C, which was the highest temperature applied. According to equation (1.12), the Reynolds number is given by:

$$Re = \frac{vl}{\nu} = \frac{\omega * r^2 * \tan \alpha}{\nu}. \quad (1.21)$$

## 1. Introduction

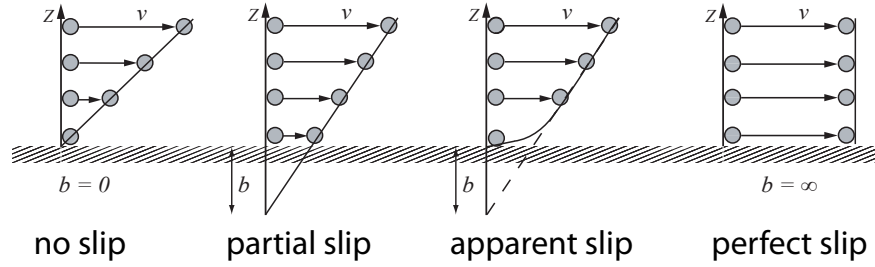


Figure 1.3.: Flow profiles for different boundary conditions and the resultant slip length  $b$  [3].

This leads to  $Re = 106$  for the highest angular frequency used  $\omega = 13 \text{ s}^{-1}$ . This is the highest Reynolds number investigated in this study and since it is still below 1000 laminar flow can be assumed. In sec. C the maximal shear rate was lower and the viscosity higher, hence the Reynolds number was even smaller.

### 1.2.3. Surface Slip

The boundary condition that the liquid in contact with a solid boundary sticks to it, is called no-slip BC. It was empirically introduced by Bernoulli in the 18th century [7] and is in agreement with many macroscopic experimental observations [8]. In 1823 though, Navier supposed that a liquid may slip over a solid surface [9] and introduced the slip length  $b$ , which is defined as the distance  $z$  from the interface where the velocity profile  $v(z)$  of the liquid extrapolates to zero:

$$b = v(0)(\partial v(z)/\partial z)^{-1}|_{z=0}. \quad (1.22)$$

The influence of different boundary conditions on the flow profile is shown in fig. 1.3. The BC at solid/liquid interfaces was subsequently intensely discussed, but since the 1840s the no-slip BC had been generally favored again. Today, fluid dynamics textbooks assume the no-slip BC, sometimes without even mentioning its empirical origin. Experimental evidence of the failure of the no-slip BC was often attributed to parasitic effects or the lack of resolution, until de Gennes theoretically predicted large slip of entangled polymers in capillaries in the late 1970s [10]. This provoked many investigations in this field and today the slippage of entangled polymer melts is a well-known phenomenon [11, 12]. In the late 1990s slip was predicted by molecular dynamics (MD) simulations [13, 14] of simple liquids as well, and shortly after that it was experimentally detected in many newtonian liquids [3, 4]. Although interfacial slip developed to a well-recognized phenomenon, its microscopic origin is still unclear, also hindered by the fact that most experimental techniques used to determine the slip length are invasive or indirect and almost no non-disturbing experiments probing the structure or dynamics on the molecular scale are present.

The first matter of debate is the magnitude of the slip length in newtonian liquids [4]. Most surface force apparatus (SFA) or atomic force microscopy (AFM) based studies, as well as flow measurements through thin capillaries, report either no slip or slip lengths on the order of some tenth of nm. This is in accordance with molecular dynamics (MD) simulation studies, where slip lengths on the order of several particle diameters are reported [13, 15, 16, 17, 18, 19, 20]. Other techniques, like sedimentation experiments, dewetting scenarios [21, 22, 23, 24, 25, 26] and local observations of the flow profile through tracer particles, report slip lengths in the  $\mu\text{m}$  range. So a search for general parameters controlling the slip length has started.

The first parameter that may affect slippage is the roughness of the solid surface. Intuitively a higher roughness should suppress slippage, which was confirmed by most studies [27], but the opposite effect was also observed [3, 4]. One problem of these studies is the difficulty to change the roughness of the surface without changing other properties, like for example the surface energy. Another important parameter is the correlation length of the roughness (see fig. 1.15), which has to be varied in a controlled manner [27].

The next parameter that should alter surface slip is the interfacial energy of the system. If the liquid tends to cover the surface, which corresponds to a high interfacial energy, slippage should be suppressed in comparison with a non-wetting system. Indeed, the majority of systems, where slippage is observed, are low energy interfaces. However, slippage was also detected on completely wetted surfaces [3, 4, 27]. In most cases, where the interfacial energy was systematically changed, the slip length decreased with increasing interfacial energy as can be seen in fig. 1.4(a) for different alkanes in contact with self-assembled monolayers (SAM). The same conclusion was drawn in a recent MD simulation study, where slippage of water was investigated [18]. On the other hand, in an SFA study of different liquids in contact with hexadecyl-trichlorosilane (HTS) it was shown that the relation between the interfacial energy and surface slip does only hold for non-polar liquids (see fig. 1.4(b)). It is noted that in most studies exploring the influence of interfacial energy on slippage, only the contact angle of the liquid (see sec. 2.6) was assumed to be the crucial parameter. But this is only valid, if the same liquid is used, as the surface tension of the liquid influences the contact angle. Therefore, caution has to be exercised when comparing these studies. In summary, all investigations involving only one type of liquid show the same trend of slippage suppression with higher interfacial energy. If different liquids are compared, this relation is not true anymore, even if the interfacial energy is compared. Thus the interfacial energy seems to play an important role in slippage, but does not explain all the results.

Intuitively, high shear rate could lead to a rise in slippage or slip could occur only above a critical shear rate. This corresponds to several observations, but in general no influence of shear rate on the slip length is observed [4]. Consistency is only achieved among MD simulations, where a dramatic slip length increase is found for shear rates close to the relaxation time of the liquid molecules.

Other possible influences on slip include pressure, electric properties or viscosity of the liquid. But none of these parameters can explain the considerable slip length differences observed for the same experimental conditions. Since slippage is influenced by many different parameters, lucidity can be solely achieved, if only one parameter is varied at

## 1. Introduction

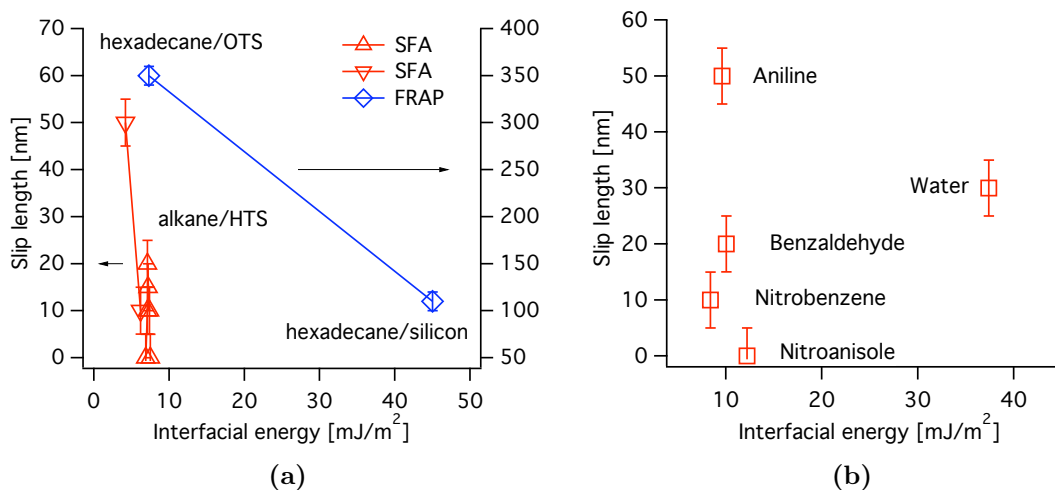


Figure 1.4.: (a) Slip length for different alkanes. Octadecyl-trichlorosilane (OTS) covered surfaces and bare silicon surfaces were investigated by fluorescence recovery after photobleaching (FRAP) [28], and the hexadecyl-trichlorosilane (HTS) interfaces were measured with the SFA [29]. (b) Slip length for different polar liquids in contact with HTS measured in the same SFA study [29].

the same time. All other parameters have to be determined and kept fixed in studies related to slip.

A currently discussed explanation of surface slip assumes the presence of a viscosity-reduced microscopic layer between the solid surface and the bulk liquid. This would lead to an observation of surface slip on a larger length scale, although the no-slip BC may still microscopically hold true [30]. This so-called *apparent slip* [31] could explain the discrepancy between *real slip* lengths on the molecular scale and large effective slip lengths observed experimentally. Theoretically the viscosity change in this layer can be due to alignment [32] or layering [33] of the near surface molecules. Such molecular ordering phenomena at solid boundaries are frequently observed in MD simulations [34, 13, 15, 16, 33, 17, 18, 19, 20], but the simulations are restricted to very high shear rates above  $10^9 \text{ s}^{-1}$ . Experimentally layering was revealed by AFM measurements after quenching sheared eicosane [35], but as the cooling process took roughly 5 s in this case, crystallization effects cannot be excluded. Another SFA study reports shear induced layering of propanol [36]. Though in this study the liquid was squeezed between atomically smooth surfaces, confinement effects cannot be excluded. In a fluorescence recovery after photobleaching (FRAP) study a larger slip length was measured for hexadecane than for squalane on the same substrate [28]. This was explained by the more roundish form of the squalane molecule contrasting to more orientational degrees of freedom in hexadecane, implying an alignment of the latter. For complex liquids, on the other hand, shear-induced order is a well-known phenomenon and is observed in aqueous solutions of polymer micelles [37] for instance.

A second possibility to produce reduced viscosity at the interface is a density depletion of the liquid at the surface. Indeed, density depleted layers were found by various x-ray and neutron reflectometry (XRR and NR) studies, investigating water/solid interfaces [38, 39, 40, 41, 42, 43], and for other liquid/solid interfaces as well [44, 45]. The origin of this density depletion was originally attributed to nanobubbles [46], but it could be shown that these were not intrinsic, but introduced by the AFM tip in stepping mode [47]. Another suggestion claimed dissolved gas to be the origin of the depletion layer [48], but the influence was not systematic and the following study with improved resolution ruled out the influence of residual gases on the depletion layer [49]. A disadvantage of the reflectometry technique is that only the density profile normal to the interface is obtained and the spatial structure of the interfacial layer usually cannot be revealed.

A link between the depletion layer and surface slip was recently established in a MD study of water close to solid walls [18], where a systematic increase of the depletion layer and slip length was seen for lower surface energies. Experimentally the depletion layer at hexadecane/solid interfaces was recorded *in situ* under shear load [45] with NR. The resulting depletion layer did not change with shear stress and was certainly too thin to explain the large slippage observed for hexadecane on OTS [28]. These very few studies are expanded by this work. In appendices A and B new findings about the origin of the depletion layer and its influence on surface slip are presented.

## 1.3. X-ray and neutron scattering

X-rays were discovered in 1895 by Wilhelm Conrad Röntgen [50] and neutrons in 1932 by Sir James Chadwick [51]. Since their discovery, they have played a crucial role in condensed matter research. Their particular character in terms of wavelength and energy makes them a perfect scientific probe to investigate the atomic and molecular structure as well as dynamics of materials. X-rays interact with shell electrons of the atom, whereas neutrons interact with the nuclei. This leads to different sensitivities of x-ray and neutron radiation and makes them complementary in material science research. Besides x-rays and neutrons, other scientific probes are used to investigate the various properties of condensed matter such as visible light, electrons or muons. In this section the basics of x-ray and neutron scattering are described and a deeper insight into reflectometry, which is the main scattering method used in this work, is given.

### 1.3.1. X-ray radiation

X-ray radiation is an electromagnetic wave in the wavelengths range from 0.01 - 10 nm, which is about the size of an atom or a molecule [6]. X-rays are produced by bending of the trajectory of energetic electrons. This may be achieved by striking a solid target in a lab source due to the Coulomb forces of the nuclei, or by strong magnets as done in a synchrotron. Initially, x-rays were produced by stopping electrons from a cold cathode in glass under vacuum. Today's lab sources use accelerated electrons (keV) collimated on a heavy metal anode, such as molybdenum, copper or tungsten. Apart from the

## 1. Introduction

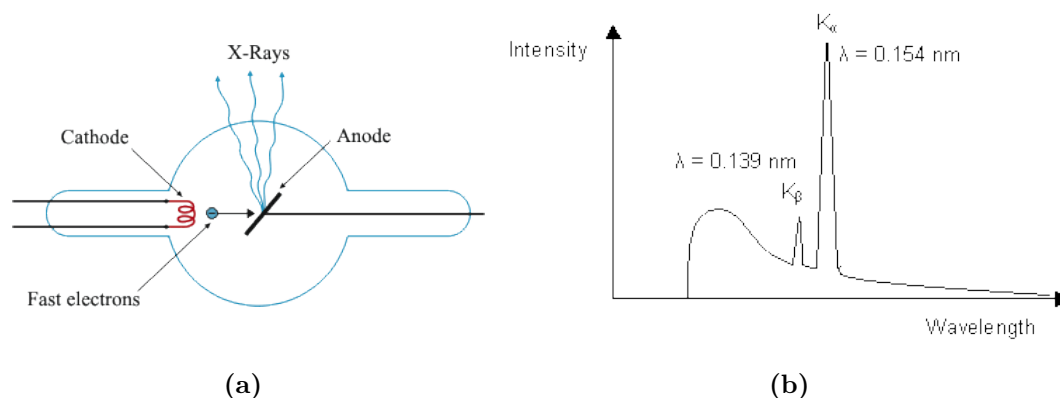


Figure 1.5.: (a) Sketch of the x-ray tube and (b) a schematic spectrum of a copper anode.

usual bremsstrahlung due to energy loss of electrons, these materials show characteristic x-ray spectra that may be much more intense than the bremsstrahlung. The origin of this characteristic wavelengths is the knocking out of a deep-lying orbital electron in the target by an energetic electron. The remaining vacancy in the inner shell is filled by a bounded electron from a higher orbit emitting the energy difference by x-rays with the characteristic wavelength. A sketch of a typical x-ray tube and the corresponding spectrum emitted by a copper anode is shown in fig. 1.5. By adjusting the electron energy to the anode material and by using special materials for the x-ray window, which absorb low energy photons, one can produce a quasi monochromatic beam as one can see in figure 1.6. It shows the intensity of the 400 Bragg reflection of single crystalline silicon versus the incoming angle (Rocking scan), measured on the laboratory reflectometer with a copper anode. The resulting peak can be perfectly reproduced by assuming two Gaussian distributions corresponding to the  $K\alpha_1$  and  $K\alpha_2$  line of copper.

Another source of x-rays is a synchrotron, where electrons are accelerated almost to the speed of light (GeV) and then deflected with magnets, which results in x-ray radiation. The first synchrotron radiation, yet in the optical spectrum, was observed in 1945 and originated from the centripetal acceleration of the electrons on the circuit [53]. Today's synchrotrons use a storage ring, where electrons are filled in from an accelerator and circuit in bunches at a relativistic speed. Bending magnets are used to force the electrons on a circular trajectory giving rise to x-ray radiation. Due to their relativistic speed the electrons emit the radiation within a narrow cone collimated in the direction of their movement as can be seen in fig. 1.7(b). This is very useful as the beam is already collimated at the source in contrast to an x-ray tube. To further improve the brightness of the beam, wigglers or undulators are used, which wiggle the electrons by a series of alternating magnetic fields (fig. 1.7(b)). Depending on the strength of the magnetic field and the distance between the magnets, the emitted x-rays may interfere with each, producing a quasi-coherent x-ray beam in the undulator. In a wiggler the magnetic field is considerably stronger and the magnets are further apart, which leads to a broader beam and consequently coherence effects are suppressed. This results in a

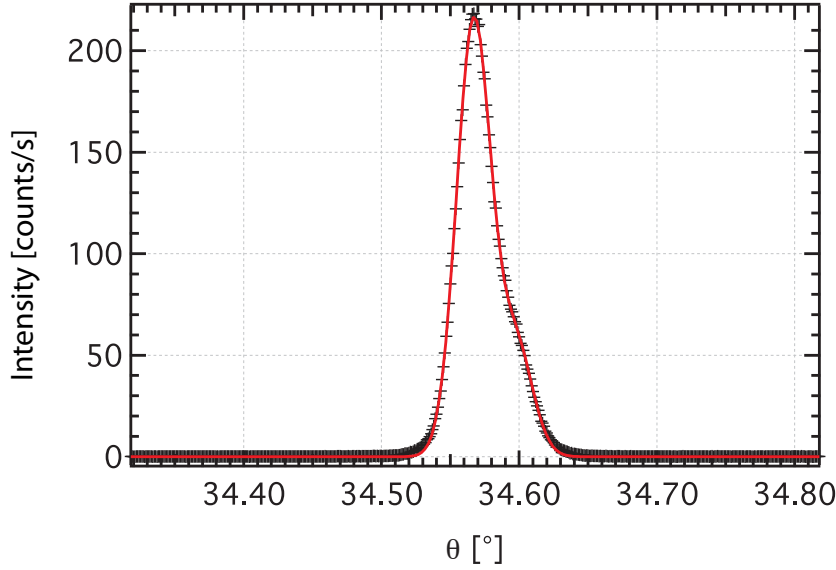


Figure 1.6.: Rocking scan of the 400 Bragg reflection of a silicon single crystal measured on a Panalytical XPert Pro laboratory reflectometer [52]. The straight line is a fit consisting of two Gaussians with the same width.

polychromatic beam. The spectral brightness, which is the photon flux per unit phase space volume, is summarized in fig. 1.7(a) for different x-ray sources.

### 1.3.2. Neutron radiation

The neutron forms, together with the proton, the elementary building blocks of nuclei. It consists of one up- and two down-quarks and hence it is electrically neutral. The fundamental properties of neutrons are listed in table 1.1. A free neutron has a lifetime

Table 1.1.: Neutron properties [56].  $\hbar$  is related to the Planck constant  $h = 2\pi\hbar$ .

Mass	$m_n = 1.675 * 10^{-27}$ kg
Spin	$s = \hbar/2$
Magnetic moment	$\mu = -9.649 * 10^{-27}$ JT <sup>-1</sup>
Lifetime ( $\beta$ -decay)	$\tau = 886$ s
Electric charge	$Q = 0$

of  $886 \pm 50$  s and decays into a proton, an electron and an antineutrino. Since it has no charge the neutron penetrates deep into matter. The only potential experienced by

# 1. Introduction

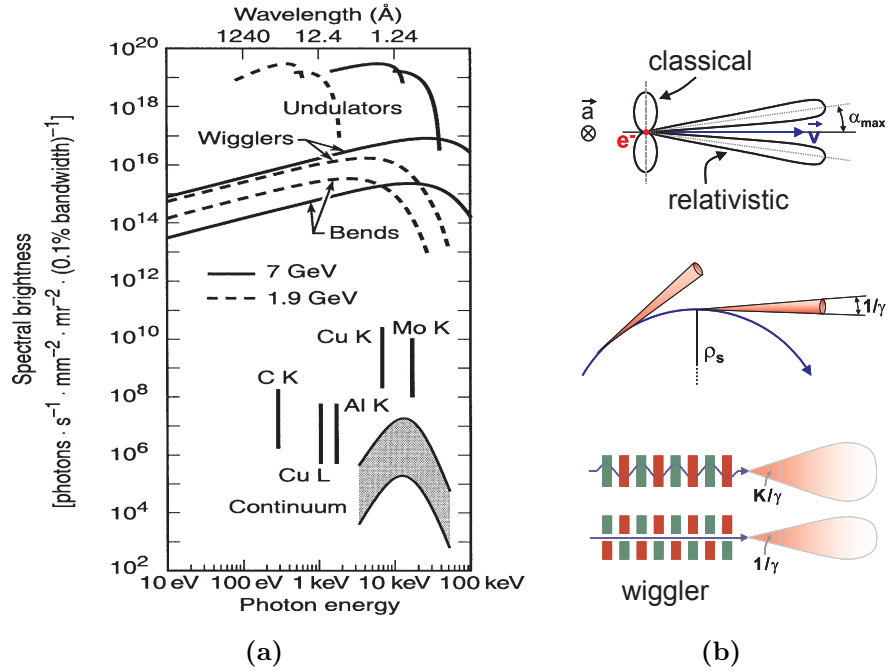


Figure 1.7.: (a) Spectral brightness for several x-ray sources [54]. The continuum spectrum corresponds to the bremsstrahlung of usual x-ray tubes, whereas the indicated two-order-of-magnitude ranges indicate the approximate variation among the characteristic radiation for different materials. (b) Radiation directions for classical and relativistic electrons and their radiation cone in a synchrotron.  $\vec{a}$  denotes the acceleration and  $\vec{v}$  the velocity. On the lower right, the top and side view of the electron trajectory in a wiggler is shown. Figure adapted from [55].

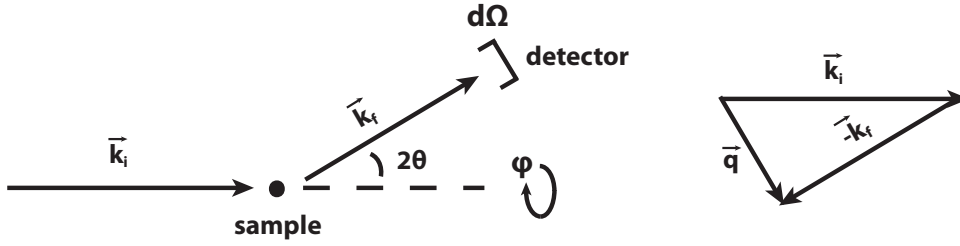


Figure 1.8.: Geometry of a scattering experiment.  $\vec{k}_i$  and  $\vec{k}_f$  denote the incoming and outgoing wave vector and  $d\Omega$  represents the solid angle covered by the detector at a scattering angle  $2\theta$  and azimuth angle  $\phi$ . The momentum transfer  $\vec{q}$  can be calculated by subtracting  $\vec{k}_f$  from  $\vec{k}_i$ .

a neutron in scattering experiments is the strong interaction of nuclei and the magnetic interaction due to its spin. Thus neutrons are ideal probes to study matter encapsulated into complex surroundings.

Neutrons for research purposes are nowadays produced in reactors by fission of Uranium-235 or in spallation sources by bombarding a target with high energy particles produced by an accelerator. Subsequently, the neutrons are cooled in a moderator to acquire the required energy band for the neutron experiment. In such a way, the fully equilibrated neutrons obtain the same energy spread as the moderator itself, namely a *Maxwell-Boltzmann* distribution with the average energy

$$E = \frac{3}{2}k_B T, \quad (1.23)$$

with  $k_B$  being the Boltzmann constant and  $T$  the temperature of the moderator. Recalling de Broglie, neutrons can be considered as a matter wave with the wavelength

$$\lambda = \frac{h}{\sqrt{2m_n E}}. \quad (1.24)$$

A typical temperature of a moderator for cold neutrons is 20 K, which corresponds to an energy of 2.6 meV. This corresponds to an average velocity  $v$  of:

$$v = \sqrt{\frac{2E}{m_n}} = \sqrt{\frac{3k_B T}{m_n}} \approx 700 \frac{\text{m}}{\text{s}}. \quad (1.25)$$

And by using eq. (1.24) one gets the average wavelength of  $\lambda = 5.6 \text{ \AA}$ .

### 1.3.3. Scattering theory

In a scattering experiment the intensity of a wave with a certain energy  $E_f$  scattered into an appointed solid angle  $\Delta\Omega$  by a sample is measured as a function of the incident

## 1. Introduction

intensity and the wavelength  $\lambda$ . The geometry of such a scattering experiment is shown in fig. 1.8. In the following only elastic scattering will be considered, as all of the measurements performed in this study assume no energy transfer between the scattered particles and the sample, and the energy spectrum of the scattered wave is not resolved. It is noted that this approximation only holds valid for small momentum transfers and for static samples. For larger scattering angles, collective excitations of the sample, e.g. phonons, may interact with the scattered wave and lead to an energy transfer. For small momentum transfers however, phonon energies are close to zero and thus only excited near reciprocal lattice vectors, which are much smaller than the momentum transfers used in this study. Another possible inelastic process is the *Doppler effect*, which arises if the collective motion of the sample is in the range of the wave velocity. As the present work includes shear experiments, this possibility has to be considered. The maximum flow speed reached with the shear device explained in sec. 1.2.2 is 0.3 m/s and is thus much less than the cold neutron velocity calculated in eq. (1.25). The resulting Doppler shift is much smaller than the momentum transfer resolution in the presented experiments and is thus not visible.

Possible inelastic contributions of single particle excitations, like diffusion, lead to even scattering in all directions (incoherent) and are modeled as a constant background. Hence one can suppose that the quantity measured in this work is the differential elastic cross section

$$\frac{d\sigma}{d\Omega} = \int \frac{d^2\sigma}{d\Omega dE_f} dE_f, \quad (1.26)$$

which gives the proportion of the wave intensity with an incident wave number  $|k_i| = \frac{2\pi}{\lambda}$  scattered into the solid angle  $d\Omega$ . As a scattering experiment is a quantum-mechanical process one has to solve the Schrödinger-equation [57]

$$(\hat{H}_0 + \hat{V})|\psi\rangle = E|\psi\rangle, \quad (1.27)$$

with the Hamiltonian consisting of the kinetic energy  $\hat{H}_0$  of the neutron or x-ray and the sample potential  $\hat{V}$  that act on the wave function  $|\psi\rangle$ . Assuming the potential to be a radial function  $\hat{V}(r)$ , as it is the case for a point scatterer, the asymptotic solution of eq. (1.27) for large distances ( $r \rightarrow \infty$ ) will be a superposition of a plane wave and a radial wave

$$\psi \sim e^{ikz} + \frac{f(\theta)}{r} e^{ikr}, \quad (1.28)$$

with  $f(\theta)$  being some function dependent on the scattering angle, which is called *scattering amplitude*. The number of particles passing through the area segment  $dS = r^2 d\Omega$  is proportional to  $|\psi|^2$ . The differential cross section is thus

$$d\sigma = |\psi|^2 dS = |\psi|^2 r^2 d\Omega. \quad (1.29)$$

If one assumes the incoming plane wave to be spatially restricted orthogonal to the propagation direction, as it is done in scattering experiments using slits, the cross section can be approximated for large distances from the scattering center, by discarding cross

terms arising from eq. (1.28):

$$\frac{d\sigma}{d\Omega} = |f(\theta)|^2. \quad (1.30)$$

If the potential  $\hat{V}$  is small compared to the kinetic energy  $\hat{H}_0$  one can solve the Schrödinger-equation using perturbation theory [57]. In this case the solution function is

$$\psi = \psi_0 + \psi_1 \quad (1.31)$$

where  $\psi_0(\vec{r})$  is the solution of the unperturbed Schrödinger-equation, namely a plane wave  $e^{i\vec{k}\vec{r}}$ , and

$$\psi_1(\vec{r}) = -\frac{m}{2\pi\hbar^2} \int V(\vec{r}') e^{i(\vec{k}\vec{r}' + \vec{k}(\vec{r}-\vec{r}'))} \frac{d\vec{r}'}{|\vec{r}-\vec{r}'|} \quad (1.32)$$

being the first-order correction for particles with the mass  $m$ . The vectors used here are sketched in fig. 1.9.

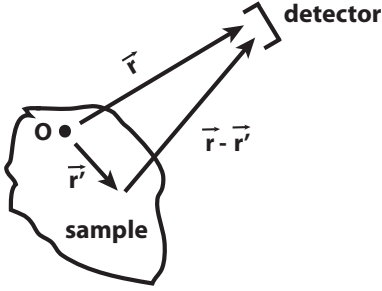


Figure 1.9.: Sketch of the vectors used in eq. (1.32). O denotes the origin of our coordinate system and  $\vec{r}'$  is an arbitrary vector inside the sample.

This formalism is known as *first-order Born approximation* or *kinematical approximation* in scattering theory. Usually typical sample sizes are on the cm scale, whereas the distance from the sample to detector is in the m range. Consequently, one can assume  $r \gg r'$ , and approximate

$$|\vec{r}-\vec{r}'| \approx |\vec{r}| = r \quad \text{and} \quad \vec{k}(\vec{r}-\vec{r}') \approx \vec{k}'\vec{r}. \quad (1.33)$$

Using this in eq. (1.31) and introducing the momentum transfer vector

$$\vec{q} = \vec{k}' - \vec{k} \quad (1.34)$$

with its length

$$q = 2k \sin \theta \quad (1.35)$$

one gets

$$\psi_1(\vec{r}) \approx -\frac{m}{2\pi\hbar^2} \frac{e^{i\vec{k}'\vec{r}}}{r} \int V(\vec{r}') e^{i\vec{q}\vec{r}'} d\vec{r}'. \quad (1.36)$$

Comparing now equations (1.31) and (1.36) with eq. (1.28) one can identify the scattering amplitude:

$$f = -\frac{m}{2\pi\hbar^2} \int V(\vec{r}') e^{i\vec{q}\vec{r}'} d\vec{r}'. \quad (1.37)$$

Mathematically, the scattering amplitude is a *Fourier transformation* of the scattering potential  $V(\vec{r})$  into the momentum transfer space, which is one of the main results of scattering theory.

## 1. Introduction

In order to calculate the scattered intensity (eq. (1.30)) one has to build the conjugate-complex scattering amplitude:

$$\frac{d\sigma}{d\Omega} = |f(\vec{q})|^2 = \left(\frac{m}{2\pi\hbar^2}\right)^2 \int V(\vec{r}') e^{i\vec{q}\vec{r}'} d\vec{r}' * \int V(\vec{r}) e^{-i\vec{q}\vec{r}} d\vec{r}. \quad (1.38)$$

If one substitutes  $\vec{r}$  by  $\vec{r}' - \vec{r}$  this can be rewritten into

$$\frac{d\sigma}{d\Omega} = \left(\frac{m}{2\pi\hbar^2}\right)^2 \int p(\vec{r}) e^{i\vec{q}\vec{r}} d\vec{r} \quad (1.39)$$

with  $p(\vec{r})$  being the *pair correlation function*

$$p(\vec{r}) = \int V(\vec{r} - \vec{r}') V(\vec{r}') d\vec{r}'. \quad (1.40)$$

Hence, according to the first-order Born approximation, the measured intensity in a scattering experiment is the Fourier transformation into  $q$ -space of the pair correlation function of the scattering potential.

### Neutron scattering

The next step is to find an appropriate potential to describe a scattering process. The scattering experiments in this work were exclusively performed by using neutron and x-ray radiation with wavelengths on the Å-lengthscale. As neutrons interact via the strong interaction, which has a typical range of fm, the appropriate potential for neutron radiation has to consist of point scatterers. The potential function for one single nucleus would thus be  $V(\vec{r}) = a\delta(\vec{r})$ , with  $\delta(\vec{r})$  being the three-dimensional Dirac delta function and  $a$  some prefactor, which is connected to the strength of the scatterer. Putting this potential into eq. (1.37) one can compute the absolute square of the scattering amplitude:

$$|f|^2 = \left| \frac{m}{2\pi\hbar^2} \int a\delta(\vec{r}) e^{i\vec{q}\vec{r}} d\vec{r} \right|^2 = \left| \frac{m}{2\pi\hbar^2} a \right|^2. \quad (1.41)$$

The total scattering strength of a single nucleus can therefore be specified by a single parameter and one defines

$$\frac{d\sigma}{d\Omega} \equiv b^2, \quad (1.42)$$

where  $b$  has the unit of length and is consequently called the *scattering length*. The scattering length for neutrons is an empirical isotope parameter and is on the order of fm. It can be negative or positive, which corresponds to an attractive or repulsive potential respectively. In the following I will consider  $b$  exclusively as the bound scattering length, which means that the scatterer is sterically fixed.

Inserting the resulting scattering amplitude from eq. (1.41) into eq. (1.30) and comparing with the definition (1.42) one can identify the prefactor  $a = \frac{2\pi\hbar^2}{m}b$  and the resulting potential

$$V(\vec{r}) = \frac{2\pi\hbar^2}{m}b\delta(\vec{r}) \quad (1.43)$$

is called *Fermi pseudopotential*. In reality the classical assumption of a Fermi pseudopotential is not sufficient. Two quantum-mechanical interactions between the neutron and the nucleus have to be considered as well, namely absorption and the spin interaction. The absorption of neutrons by nuclei depends on the energy of neutrons and is particularly strong if the compound energy of the neutron and the nucleus corresponds to a resonance energy, where nuclear reactions take place [58]. For cold or thermal neutrons only few isotopes (e.g.  $^{10}\text{B}$ ,  $^{113}\text{Cd}$ ,  $^{149}\text{Sm}$ ,  $^{157}\text{Gd}$ ) show resonance absorption of neutrons. The elements used in this study do not have any resonance absorption peaks in the energy range used and the absorption is negligibly small. Nevertheless the small amount of absorption was considered in the data analysis (see sec. 1.3.4).

The second quantum-mechanical correction in neutron scattering is the spin interaction between the neutron and the nucleus. As the neutron has a spin of  $-\hbar/2$ , the overall spin system, consisting of the neutron spin and the nuclear angular momentum  $j$ , can have up to two different total spin states  $j - \hbar/2$  or  $j + \hbar/2$  with a probability factor  $g^+$  and  $g^-$  respectively, determined by possible spin configurations of the system [59]. Each of this spin combinations results in a different scattering length  $b^+$  and  $b^-$ . The average scattering length  $\langle b \rangle$  of a system consisting of one sort of isotopes with random spins relatively to the neutrons is hence:

$$\langle b \rangle = g^+ b^+ + g^- b^- \equiv b_c. \quad (1.44)$$

$b_c$  is the mean resulting scattering length of two sorts of scatterers, which scatter in phase and is therefore called *coherent scattering length*. The standard variation of scattering lengths

$$\sqrt{\langle b^2 \rangle - \langle b \rangle^2} \equiv b_i \quad (1.45)$$

corresponds to the mean deviation from the average scattering length and thus matches with the fraction of out-of-phase scattering and is consequently called *incoherent scattering length*. If a distribution of different isotopes is present, as it is the case in the natural composition of elements, an additional distribution of effective scattering lengths must be considered. The total cross section  $\sigma_{tot}$  according to eq. (1.42) can be divided into three parts:

$$\sigma_{total} = \int \frac{d\sigma}{d\Omega} d\Omega = 4\pi b^2 \equiv 4\pi b_c^2 + 4\pi b_i^2 + \sigma_{abs} \equiv \sigma_{coh} + \sigma_{inc} + \sigma_{abs}, \quad (1.46)$$

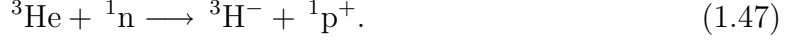
with  $\sigma_{coh}$ ,  $\sigma_{inc}$  and  $\sigma_{abs}$  being the coherent, incoherent and absorption cross sections respectively. In table 1.2 neutron scattering lengths and cross sections for some light elements and their isotopes with mass number  $A$  are listed. The scattering lengths for various nuclei may differ significantly, even when comparing two isotopes of the same element. This allows selective isotope replacement tuning the cross sections in a neutron scattering experiment. The exchange of protons by deuterons is a common approach for contrast variation, especially in the case of organic materials. Another isotope extensively used in neutron scattering is  $^3\text{He}$ . Due to its high absorption cross-section it is used for the detection of neutrons. The helium captures the neutron  $^1_0\text{n}$  and

## 1. Introduction

Table 1.2.: Neutron scattering lengths (in fm) and cross sections (in barn = 100 fm<sup>2</sup>) for some light elements with atomic number  $Z$  in their natural composition and for their isotopes with mass number  $A$  [56]. The absorption cross sections are given for a neutron energy of 25.3 meV. For unstable nuclei their half life time  $T_{1/2}$  is given.

	$Z$	$A$	abundance (%)	$b_c$	$\sigma_{coh}$	$\sigma_{inc}$	$\sigma_{abs}$
H	1			-3.74	1.76	80.27	0.33
		1	99.985	-3.74	1.76	80.28	0.33
		2	0.015	6.67	5.59	2.05	$5 \cdot 10^{-4}$
		3	$T_{1/2} = 12.3$ y	4.79	2.89	0.14	$< 10^{-6}$
He	2			3.26	1.34	0	$7.5 \cdot 10^{-3}$
		3	0.013	5.75	4.42	1.53	5333
		4	99.987	3.26	1.34	0	0
Li	3			-1.9	0.45	0.92	70.5
		6	7.5	2.01	0.52	0.47	940
		7	92.5	-2.22	0.62	0.78	0.05
B	5			5.3	3.55	1.7	767
		10	19.4	-0.24	0.14	3.04	3835
		11	80.2	6.65	5.57	0.22	$5.5 \cdot 10^{-3}$
C	6			6.65	5.55	0.001	$3.5 \cdot 10^{-3}$
		12	98.89	6.65	5.56	0	$3.5 \cdot 10^{-3}$
		13	1.11	6.2	4.81	0.034	$1.4 \cdot 10^{-3}$
N	7			9.36	11	0.5	1.9
		14	99.635	9.37	11	0.5	1.91
		15	0.365	6.44	5.22	$5 \cdot 10^{-5}$	$2.5 \cdot 10^{-5}$
O	8			5.81	4.23	$8 \cdot 10^{-4}$	$1.9 \cdot 10^{-4}$
		16	99.75	5.81	4.23	0	$1.0 \cdot 10^{-4}$
		17	0.039	5.65	4.2	0.004	0.24
		18	0.208	5.85	4.29	0	$1.6 \cdot 10^{-4}$
Al	13	27	100	3.45	1.5	0.008	0.23
Si	14			4.15	2.16	0.005	0.17
		28	92.2	4.11	2.12	0	0.18
		29	4.7	4.71	2.78	0.001	0.1
		30	3.1	4.59	2.65	0	0.11

subsequently decomposes into tritium and a proton:



The charged fission products produce electron-ion pairs in the surrounding gas, which are collected in electrodes via a strong electric field, and the resulting current can be measured.

Note that the interference effects, which cause the diffraction or reflection patterns observed in this study, are exclusively due to coherent scattering, as incoherent scattering is not phase preservative. The incoherent neutron scattering was thus put on a level with absorption in the data analysis.

Now a certain distribution  $\rho_n(\vec{r})$  of nuclei will be considered. In a crystal for example the nuclei are distributed on a three-dimensional lattice with basis vectors  $\vec{a}$ ,  $\vec{b}$  and  $\vec{c}$ . If it consists of only one type of nuclei, their distribution can be written as:

$$\rho_n(\vec{r}) = \sum_{n,m,l=0}^N \delta(\vec{r} - (n\vec{a} + m\vec{b} + l\vec{c})), \quad (1.48)$$

with  $n, m, l$  being positive integers and  $N$  the number of nuclei in our sample. Inserting this distribution as a sum of Fermi pseudopotentials (eq. (1.43)) into the scattering function (eq. (1.41)) one can calculate the resulting differential cross section (1.30):

$$\frac{d\sigma}{d\Omega} = \left| \int b\rho_n(\vec{r})e^{i\vec{q}\vec{r}}d\vec{r} \right|^2 = \left| b \int \sum_{n,m,l=0}^N \delta(\vec{r} - (n\vec{a} + m\vec{b} + l\vec{c}))e^{i\vec{q}\vec{r}}d\vec{r} \right|^2. \quad (1.49)$$

This boils down to

$$\frac{d\sigma}{d\Omega} = \left| b \sum_{n,m,l=0}^N e^{in\vec{q}\vec{a}}e^{im\vec{q}\vec{b}}e^{il\vec{q}\vec{c}} \right|^2. \quad (1.50)$$

This is a product of three geometric progressions and for  $N > 1$  they can be simplified:

$$\left| \sum_{n=0}^N e^{in\vec{q}\vec{a}} \right|^2 = \left| \frac{1 - (e^{in\vec{q}\vec{a}})^{N+1}}{1 - e^{in\vec{q}\vec{a}}} \right|^2 = \frac{1 - \cos(N\vec{q}\vec{a})}{1 - \cos(\vec{q}\vec{a})} = \left( \frac{\sin(N\frac{\vec{q}\vec{a}}{2})}{\sin(\frac{\vec{q}\vec{a}}{2})} \right)^2. \quad (1.51)$$

For the last simplification the identity  $1 - \cos 2\alpha = 2\sin^2 \alpha$  was used. This function peaks for momentum transfers  $\vec{q}_a$  which obey:

$$\vec{q}_a\vec{a} = 2\pi n, \quad (1.52)$$

and is known as the *Laue condition*. These peaks are sharper for larger  $N$  and are called *Bragg peaks*.

### X-ray scattering

As mentioned before, x-rays are scattered by electrons and the easiest scattering process is the elastic scattering by a single free electron, called *Thomson scattering*. As an x-ray beam is an electromagnetic wave it induces an oscillation of the electron, which leads to an emitted electromagnetic wave as shown in fig. 1.10. By assuming the oscillating electron to behave like a Hertz-dipole one can calculate the emitted wave intensity and thus the differential cross section out of the Maxwell equations and one gets [60]:

$$\frac{d\sigma}{d\Omega} = r_0^2 P, \quad (1.53)$$

where  $r_0$  is the classical electron radius and  $P$  the polarization factor which depends on the projection of the polarization of the incoming wave on the detector:

$$P = \begin{cases} 1 & \text{out of the plane of linear polarization} \\ \cos^2 \phi & \text{in the plane of linear polarization} \\ \frac{1}{2}(1 + \cos^2 \theta) & \text{no linear polarization.} \end{cases} \quad (1.54)$$

Apart from the polarization factor, the result (1.53) is very similar to the scattering cross section for neutrons ((1.42)), thus  $r_0$  is often called the *Thomson scattering length*. A lab source usually emits unpolarized x-rays, due to their statistical production, whereupon synchrotron sources produce photons, which are polarized in the bending plane. However, the synchrotron measurements performed in this work were recorded perpendicular to the polarization plane and thus no polarization correction had to be applied.

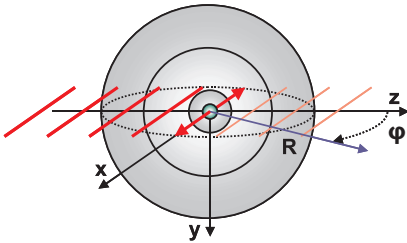


Figure 1.10.: Emission of an electromagnetic wave by an oscillating electron induced by an incoming wave with a polarization in the x-plane (red lines) [60].

Now the case of a cloud of  $Z$  free electrons will be considered: the classical approximation of an atom shell. If the electron distribution in the atom is given by  $\rho_e(\vec{r})$  one can calculate the scattering cross section analogically to neutrons via the left side of eq. (1.49):

$$\frac{d\sigma}{d\Omega} = \left| \sqrt{P} \int -r_0 \rho_e(\vec{r}) e^{i\vec{q}\vec{r}} d\vec{r} \right|^2 = \left| -r_0 \sqrt{P} f^0(\vec{q}) \right|^2. \quad (1.55)$$

The minus comes from the fact that a phase shift of  $\pi$  occurs as soon as the x-ray is scattered by the oscillating electron. The Fourier transformation of the electron distribution within the atom  $f^0(\vec{q})$  is called *atomic form factor*.

Of course if one assumes a more realistic model, the electrons are not free, but bound in orbits. Consequently, there is a correction of the atomic form factor by  $f'(E)$  which depends on the energy  $E$  of incoming x-rays as the electron oscillation is damped in a certain energy range. Moreover, absorption or inelastic

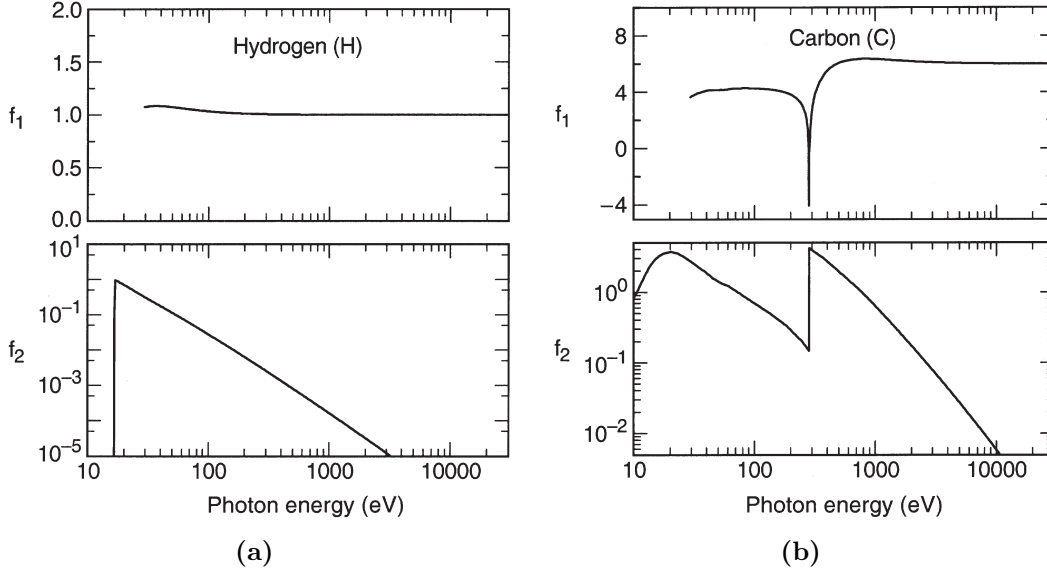


Figure 1.11.: Atomic scattering functions for natural (a) hydrogen and (b) carbon [54].

scattering of x-rays may happen as well, which can be considered by introducing an imaginary part  $if''(E)$ . Thus the resulting atomic form factor with quantum-mechanical dispersion corrections can be written as:

$$f(\vec{q}, E) = f^0(\vec{q}) + f'(E) + if''(E). \quad (1.56)$$

The resulting atomic scattering function for the forward scattering  $f(\vec{q} = 0, E) = f_1(E) + if_2(E)$  is determined by experiments and a result for hydrogen and carbon is plotted in fig. 1.11. The real part of the carbon scattering function can be divided into three parts. In the high energy limit the scattering is energy independent and the scattering function  $f_1$  equals the classical case  $f^0$ . All electrons can be considered as free and they scatter in phase into the forward direction, leading to  $f^0(\vec{q} = 0) = Z$ . For energies of about 300 eV the scattering function of carbon has a minimum. This is due to resonance between the x-ray energy and the electron binding energies. Hence, most of the photons are scattered inelastically and this process is called *resonant scattering*. In the case of low energies the influence of bounded electrons lowers the resulting scattering length and this regime is called *Raleigh scattering*.

The x-ray absorption  $f_2$  for energies less than 40 keV is governed by the *photoelectric effect* [6]. In this case, the x-ray photon is absorbed by an electron from the inner shell, which consequently leaves the atom. This process is energy dependent and shows huge changes at a resonance as can be seen in fig. 1.11(b). The x-ray energies used in this work ranged from 8 - 15 keV and were in the Thomson scattering limit for all materials involved. For the detection of x-rays a variety of techniques is available [54]. A simple and commonly used detector is the scintillation crystal, which converts x-rays into photons that are afterwards detected by a photo diode.

### 1.3.4. Reflectometry and Grazing Incidence Diffraction

In a scattering experiment, where a well-collimated incident beam impinges on the sample surface under a shallow angle, the approximation that the incoming wave is not altered by the sample does generally not hold anymore. This is crucial to solve the Schrödinger equation (1.27) by using the first-order Born approximation as it was done in sec. 1.3.3. Consequently, one has to adopt another formalism to describe this kind of experiments. As the momentum transfers in grazing incidence scattering experiments are usually small, the interferences from individual atoms are not observed and the appropriate potential to describe the interaction between the incoming wave and the sample is a mean field of scatterers  $V_0$ .

If one assumes a step potential  $\langle V(\vec{r}) \rangle$  which is 0 for negative  $z$ -values and equals  $V_0$  for the positive semi-space along the  $z$ -axis, the Schrödinger equation (1.27) can be formulated as:

$$\nabla^2\psi(\vec{r}) + k^2\psi(\vec{r}) = 0 \quad \text{with} \quad k^2 = \frac{2m}{\hbar^2}(E - \langle V(\vec{r}) \rangle), \quad (1.57)$$

which resembles the *Helmholtz equation*, describing the propagation of an electromagnetic wave in classical optics [61]. The solution of this equation is:

$$\psi(\vec{r}) = \begin{cases} a_i e^{i\vec{k}_i \vec{r}} + a_f e^{i\vec{k}_f \vec{r}} & \text{for } z < 0 \\ a' e^{i\vec{k}' \vec{r}} & \text{for } z > 0. \end{cases} \quad (1.58)$$

The wavevectors  $\vec{k}_i$ ,  $\vec{k}_f$  and  $\vec{k}'$  can be identified with the incoming, reflected and transmitted wave respectively. Furthermore, one can calculate the index of refraction  $n$  inside the medium, which is defined as [61]:

$$n^2 = \frac{k^2}{k_0^2} = 1 - \frac{V_0}{E}. \quad (1.59)$$

The appropriate potential to choose in this case is a distribution of Fermi pseudopotentials (1.43) with an average density  $\rho$ :

$$V_0 = \frac{2\pi\hbar^2}{m} b\rho = \frac{2\pi\hbar^2}{m} N_b. \quad (1.60)$$

$N_b$  is called *scattering length density* (SLD) and corresponds to the average coherent nuclear scattering length density  $\rho_0 \langle b_{coh} \rangle$  in the case of neutron radiation and to the Thomson scattering length density  $\rho_e r_0$  for x-rays. When inserting this into equation (1.59) and calculating the energy of the radiation via de Broglie (1.24) one gets

$$n^2 = 1 - \frac{\lambda^2}{\pi} N_b. \quad (1.61)$$

In order to take absorption into account, the so-called absorption coefficient  $\mu$  is introduced via the absorption law [6]:

$$I(z) = I(0)e^{-\mu z} \quad (1.62)$$

where  $z_{1/e} = \mu^{-1}$  matches the thickness of the material after which the incoming intensity  $I$  is attenuated by a factor of  $e$ . For neutrons the absorption coefficient is  $\mu = \rho_0(\langle \sigma_{abs} \rangle + \langle \sigma_{inc} \rangle)$  and for x-rays [60]:  $\mu = -2\lambda\rho_a r_0 \langle f'' \rangle$  with  $\rho_a$  being the average atom density. Therefore, one has to add an imaginary part to the refraction index, which corresponds to the absorption:

$$n^2 = 1 - \frac{\lambda^2}{\pi} N_b - i \frac{\mu}{k_0} = 1 - \frac{\lambda^2}{\pi} N_b - i \frac{\lambda}{2\pi} \mu. \quad (1.63)$$

The term  $\frac{\lambda^2}{\pi} N_b$  is typically on the order of  $10^{-5}$  and the refractive index for x-rays and neutrons is very close to one. The absorption is usually even smaller, thus the refractive index can be approximated by:

$$n \approx 1 - \frac{\lambda^2}{2\pi} N_b - i \frac{\lambda}{4\pi} \mu. \quad (1.64)$$

If the scattering length density is positive, as it is always the case for x-rays and also for most materials investigated by neutron radiation (see tab. 1.2), the resulting refraction index is smaller than one, which means that these materials appear optically less dense than vacuum for these types of radiation. This is connected with the phase shift during the scattering process and may lead to *total external reflection* of the incoming wave under a shallow angle. In the quantum-mechanical approach (eq. (1.58)) this happens if the component of the kinetic energy in z-direction of the incoming wave is smaller than the potential  $V_0$ . In order to calculate the critical angle of total external reflection  $\theta_c$  the Snellius law is used:

$$\frac{\cos(\theta)}{\cos(\theta')} = \frac{n_1}{n_2}. \quad (1.65)$$

Using  $n_1 = 0$  for vacuum and  $n_2$  from eq. (1.64) one gets:

$$\sin \theta_c \approx \theta_c = \lambda \sqrt{\frac{N_b}{\pi}}, \quad (1.66)$$

where the small angle approximation was used, as the critical angles for neutrons and x-rays are very small.

## Reflectometry

In a reflectometry set-up, the intensity of a wave, reflected from the surface of a sample is measured. In the simplest case only the specular signal is detected, meaning that the glancing angle  $\theta_i$  equals the reflection angle  $\theta_f$  resulting in a momentum transfer vector  $\vec{q}$  which is normal to the surface as can be seen in fig. 1.12. The reflected and refracted intensities can be calculated by imposing the boundary condition that the wave function  $\psi(\vec{r})$  and its derivative  $\nabla\psi(\vec{r})$  must be continuous at the interface  $z = 0$ . This leads to the following requirements for the (complex) amplitudes:

$$a_i + a_f = a' \quad (1.67)$$

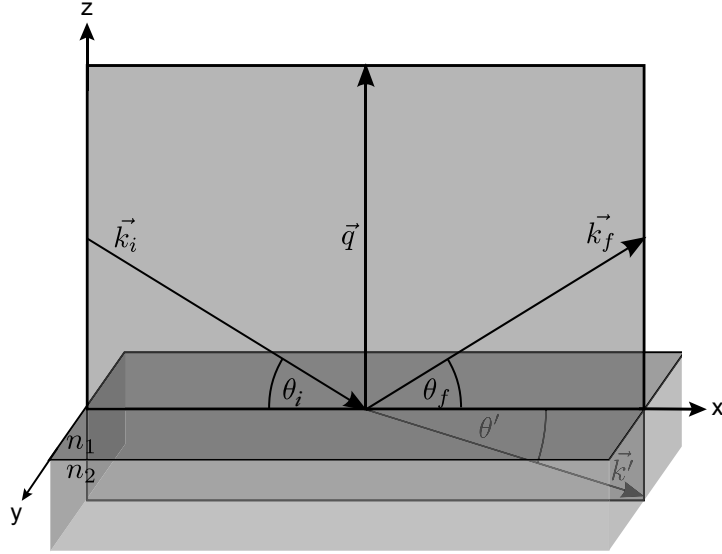


Figure 1.12.: Reflection geometry (fig. from [52]). Details are explained in the text.

and

$$a_i \vec{k}_i + a_f \vec{k}_f = a' \vec{k}' \quad (1.68)$$

With the wave number in vacuum  $k = |\vec{k}_i| = |\vec{k}_f|$  and the resulting wave vector in the material [60]  $nk = |\vec{k}'|$ , this yields for the components parallel and perpendicular to the surface respectively

$$a_i k \cos \theta + a_f k \cos \theta = a' (nk) \cos \theta' \quad (1.69)$$

and

$$(a_i - a_f) k \sin \theta = a' (nk) \sin \theta'. \quad (1.70)$$

The parallel projection (1.69) together with eq. (1.67) reproduce the Snellius law (1.65), whereas the projection perpendicular to the surface (1.70) together with eq. (1.67) yields the amplitude of the reflectivity  $r$  and transmittivity  $t$ :

$$r \equiv \frac{a_f}{a_i} = \frac{\sin \theta - n \sin \theta'}{\sin \theta + n \sin \theta'} \quad (1.71)$$

$$t \equiv \frac{a'}{a_i} = \frac{2 \sin \theta}{\sin \theta + n \sin \theta'}, \quad (1.72)$$

which are known as the Fresnel equations in classical optics [61]. Applying the Snellius law (1.65) one can transform the reflected amplitude:

$$r = \frac{\sin \theta - \sqrt{n^2 - \cos^2 \theta}}{\sin \theta + \sqrt{n^2 - \cos^2 \theta}}. \quad (1.73)$$

If one now assumes only small angles and little absorption, one can approximate the square of the refractive index (1.64) by omitting the quadratic terms:

$$n^2 \approx 1 - 2\frac{\lambda^2}{2\pi}N_b - 2i\frac{\lambda}{4\pi}\mu = 1 - \theta_c^2 - i\frac{\lambda}{2\pi}\mu, \quad (1.74)$$

with the critical angle  $\theta_c$  from eq. (1.66). Thus one can further transform the reflected amplitude for small angles:

$$r = \frac{\theta - \sqrt{\theta^2 - \theta_c^2 - i\frac{\lambda}{2\pi}\mu}}{\theta + \sqrt{\theta^2 - \theta_c^2 - i\frac{\lambda}{2\pi}\mu}}. \quad (1.75)$$

In the following the angles can be converted into momentum transfers  $q$  via eq. (1.35), as usual in scattering geometry, and the reflected intensity is

$$R_F \equiv |r|^2 = \left| \frac{q - \sqrt{q^2 - q_c^2 - i\frac{8\pi}{\lambda}\mu}}{q + \sqrt{q^2 - q_c^2 - i\frac{8\pi}{\lambda}\mu}} \right|^2, \quad (1.76)$$

which is the reflectivity from a sharp interface and known as the *Fresnel reflectivity*. For large momentum transfers  $q \gg q_c$  this reduces to

$$R_F \approx \frac{q_c^4}{16q^4}. \quad (1.77)$$

The Fresnel reflectivity of an ideal silicon substrate investigated by neutrons is plotted in fig. 1.13(a).

Now the reflectivity from a stratified sample, consisting of  $N$  slabs with thicknesses  $d_j$  and refractive indices  $n_j$  as it is sketched in fig. 1.14 will be considered. As the resulting momentum transfers in a specular reflectivity experiment are always normal to the interface, one has to consider only the  $z$ -component of the wave. The wave function in this direction can be written as a superposition of an upwards and downwards traveling wave:

$$\psi(z) = a_j^+ e^{ik_{z,j}z} + a_j^- e^{-ik_{z,j}z}, \quad (1.78)$$

where  $k_{z,j}$  is the projection perpendicular to the interface of the incident wave vector  $k$

$$k_{z,j} = kn_j \sin \theta_j. \quad (1.79)$$

Due to the continuity requirement of  $\psi$  and  $\frac{d}{dz}\psi$  at the depth  $z_{j,j+1}$  between two phases  $j$  and  $j+1$  one derives

$$a_j^+ e^{ik_{z,j}z_{j+1}} + a_j^- e^{-ik_{z,j}z_{j+1}} = a_{j+1}^+ e^{ik_{z,j+1}z_{j+1}} + a_{j+1}^- e^{-ik_{z,j+1}z_{j+1}} \quad (1.80)$$

and

$$k_{z,j}[a_j^+ e^{ik_{z,j}z_{j+1}} - a_j^- e^{-ik_{z,j}z_{j+1}}] = k_{z,j+1}[a_{j+1}^+ e^{ik_{z,j+1}z_{j+1}} - a_{j+1}^- e^{-ik_{z,j+1}z_{j+1}}]. \quad (1.81)$$

1. Introduction

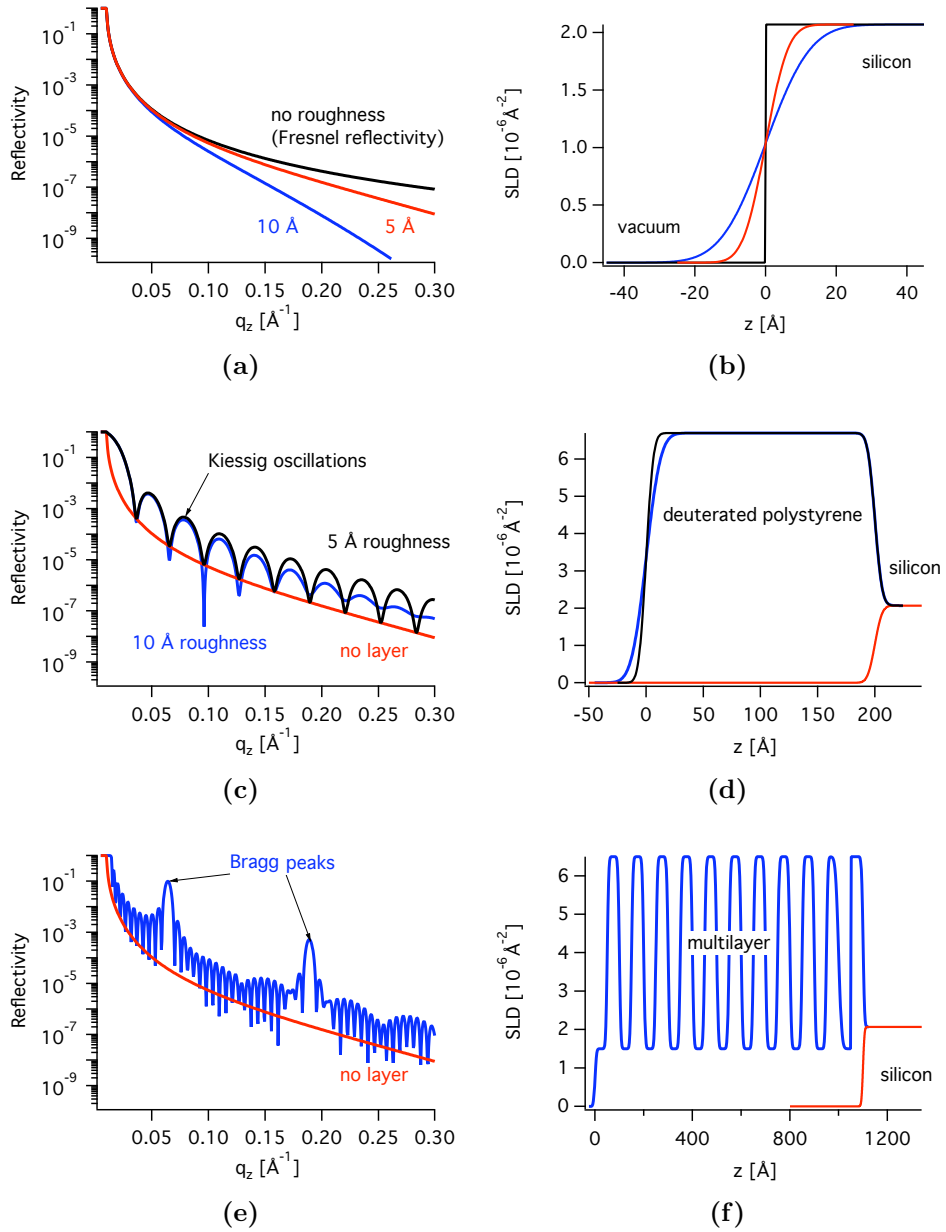


Figure 1.13.: Neutron reflectivities on a logarithmic scale for different sample systems explained in the SLD profile on the right.

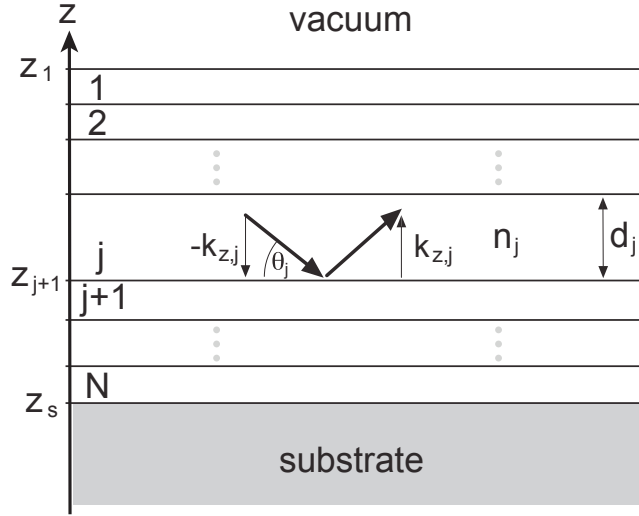


Figure 1.14.: Schematic drawing of a stratified medium. Details are explained in the text.

The combination of these two equations can be written in a matrix form:

$$\begin{pmatrix} a_j^+ e^{ik_{z,j}z_{j+1}} \\ a_j^- e^{-ik_{z,j}z_{j+1}} \end{pmatrix} = \begin{pmatrix} p_{j,j+1} & m_{j,j+1} \\ m_{j,j+1} & p_{j,j+1} \end{pmatrix} * \begin{pmatrix} a_{j+1}^+ e^{ik_{z,j+1}z_{j+1}} \\ a_{j+1}^- e^{-ik_{z,j+1}z_{j+1}} \end{pmatrix}, \quad (1.82)$$

with matrix elements

$$\begin{aligned} p_{j,j+1} &= \frac{k_{z,j} + k_{z,j+1}}{2k_{z,j}}, \\ m_{j,j+1} &= \frac{k_{z,j} - k_{z,j+1}}{2k_{z,j}}. \end{aligned} \quad (1.83)$$

This matrix transforms the wave amplitudes from the medium  $j$  to the medium  $j + 1$  and is called refraction matrix  $\mathcal{R}_{j,j+1}$ . Furthermore there is a phase shift due to the thickness  $d_j$  of the layer and this can be presented in matrix form as well:

$$\begin{pmatrix} a_j^+ e^{ik_{z,j}z_j} \\ a_j^- e^{-ik_{z,j}z_j} \end{pmatrix} = \begin{pmatrix} e^{-ik_{z,j}d_j} & 0 \\ 0 & e^{ik_{z,j}d_j} \end{pmatrix} * \begin{pmatrix} a_j^+ e^{ik_{z,j}z_{j+1}} \\ a_j^- e^{-ik_{z,j}z_{j+1}} \end{pmatrix}. \quad (1.84)$$

This matrix is called the transition matrix  $\mathcal{T}_j$ . Combining the two matrices one can compute the wave amplitude at the surface ( $z = z_1$ ) out of the amplitudes at the substrate interface ( $z = z_s$ ):

$$\begin{pmatrix} a_0^+ e^{ik_{z,0}z_1} \\ a_0^- e^{-ik_{z,0}z_1} \end{pmatrix} = \mathcal{R}_{0,1} \mathcal{T}_1 \dots \mathcal{T}_N \mathcal{R}_{N,s} * \begin{pmatrix} a_s^+ e^{ik_{z,s}z_s} \\ a_s^- e^{-ik_{z,s}z_s} \end{pmatrix}. \quad (1.85)$$

The resulting matrix out of this product is again a  $2 \times 2$  matrix and is called the transfer matrix:

$$\begin{pmatrix} a_0^+ e^{ik_{z,0}z_1} \\ a_0^- e^{-ik_{z,0}z_1} \end{pmatrix} = \begin{pmatrix} M_{11} & M_{12} \\ M_{21} & M_{22} \end{pmatrix} * \begin{pmatrix} a_s^+ e^{ik_{z,s}z_s} \\ a_s^- e^{-ik_{z,s}z_s} \end{pmatrix}. \quad (1.86)$$

## 1. Introduction

The reflection coefficient  $r$  is defined as the ratio of the reflected wave to the incoming wave:

$$r = \frac{a_0^+ e^{ik_{z,0}z_1}}{a_0^- e^{-ik_{z,0}z_1}} = \frac{M_{11}a_s^+ e^{ik_{z,s}z_s} + M_{12}a_s^- e^{-ik_{z,s}z_s}}{M_{21}a_s^+ e^{ik_{z,s}z_s} + M_{22}a_s^- e^{-ik_{z,s}z_s}}. \quad (1.87)$$

If the substrate is sufficiently thick ( $> 0.1$  mm), so that there is no reflected beam from the backside of the substrate, one may assume:

$$a_s^+ e^{ik_{z,s}z_s} = 0, \quad (1.88)$$

and the reflectivity  $R$  can be calculated:

$$R = |r|^2 = \left| \frac{M_{12}}{M_{22}} \right|^2. \quad (1.89)$$

This method is known as the optical matrix method [62]. It is a recursive method to calculate the exact reflectivity and is used in most fitting routines [63, 64]. For large angles ( $q_z \gg q_c$ ) the reflectivity can be approximated by the first-order Born approximation. Looking at the sample curves in fig. 1.13 one can observe some features that can be explained in the kinematic approximation, namely interference minima due to the layered structure, which lead to so-called *Kiessig oscillations* and Bragg peaks in case of multilayers.

Up until now perfectly sharp interfaces were assumed. This is obviously not the case for real systems. If one assumes for example diffusion from one phase into the other, then there will be a graded interface between them (see fig. 1.15). For simplicity in the following only large momentum transfers will be considered ( $q_z \gg q_c$ ), where the Born approximation is valid. It can be shown, that the same result may be achieved by dividing the rough interface into a series of thin slabs, and calculating the reflectivity by the exact optical matrix method. In the Born approximation, however, the reflection coefficient from a graded interface, with the interfacial density function  $f(z)$ , which is 0 for  $x = +\infty$  and 1 for  $x = -\infty$ , is given by the Fourier transformation of the gradient of this function (derivative) and thus the reflectivity from a graded interface is [60] :

$$R(q_z) = R_F(q_z) \left| \int_0^\infty \left( \frac{df}{dz} \right) e^{iq_z z} dz \right|^2, \quad (1.90)$$

which is referred to as the master equation. If a Gaussian distribution between two phases is assumed, then the resulting interfacial density function is an error function  $\text{erf}(z)$ :

$$f(z) = \text{erf} \left( \frac{z}{\sqrt{2}\sigma} \right), \quad (1.91)$$

with the Gaussian width  $\sigma$  as depicted in fig. 1.15. The derivative of the error function is a Gauss curve which is Fourier transformed into another Gaussian distribution and thus the reflected intensity for a statistical interface is:

$$R(q_z) = R_F(q_z) e^{-q_z^2 \sigma^2}, \quad (1.92)$$

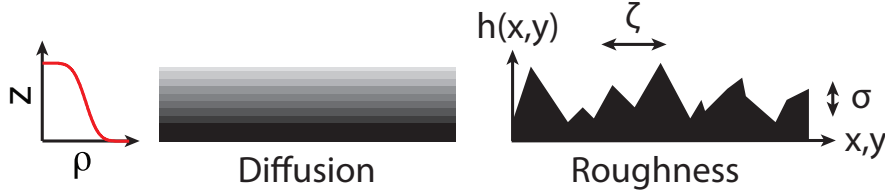


Figure 1.15.: Diffusive and rough interface [65].  $\sigma$  corresponds to the Gaussian width of the Error function plotted on the left.  $h(x, y)$  denotes the height function and  $\zeta$  shows the lateral correlation length.

which has the same effect as the *Debye-Waller factor* on the measured intensity. It causes a steeper drop-off of the reflectivity as can be seen in fig. 1.13(a). A more accurate calculation of the reflectivity of a rough interface can be achieved by using the *distorted wave Born approximation* (DWBA). Doing so, one can show that the Debye-Waller factor holds valid only if the lateral correlation length  $\zeta$  (see fig. 1.15) is much larger than the corresponding coherence length of the impinging wave, i.e. the maximal distance within the beam with a well-defined phase relation [62]. At the other extreme, if  $\zeta$  is much smaller than the correlation length, the roughness leads to a slightly changed reflectivity:

$$R(q_z) = R_F(q_z)e^{-q_z q_z' \sigma^2}, \quad (1.93)$$

which is known as the *Nevot-Croce factor* [66].

### Off-specular scattering

It is worth mentioning at this point, that the reflected intensity is restricted to the specular condition, i.e. where the momentum transfer is normal to the interface, as no density correlations parallel to the surface are present. If one assumes a rough interface as can be seen in fig. 1.15 on the right, there will be lateral correlations on some length scale  $\zeta$ . Consequently, there will be some non-vanishing signal in the off-specular directions, which is also called *diffuse scattering*. In order to calculate the scattering cross section in this case, the Born approximation is applied again. Note that this ansatz is valid only far from total reflections. In the other case the DWBA has to be applied. Nevertheless, for a coarse derivation of the diffuse scattering, the Born approximation leads to the scattering amplitude given by eq. (1.37). The ultimate information about the surface is given by the height function  $h(x, y)$  as shown in fig. 1.15 and the scattering potential can be formulated as  $V(\vec{r}) = \Delta N_b H(z - h(x, y))$ , with the SLD difference  $\Delta N_b$  between two adjacent layers.  $H(z)$  is the step function, which is 0 for negative  $z$ -values and 1 for  $z \geq 0$ . One consequently gets:

$$f(\vec{r}) = \int_V \Delta N_b H(z - h(x, y)) e^{i\vec{q}\vec{r}}. \quad (1.94)$$

## 1. Introduction

Transformation from a volume integral into a surface integral using Gauss' theorem and calculation of the conjugate-complex scattering intensity result in:

$$\frac{d\sigma}{d\Omega} = \left( \frac{\Delta N_b}{q_z} \right)^2 \int_S \int_{S'} e^{iq_z[h(x,y)-h(x',y')]} e^{iq_x(x-x')} e^{iq_y(y-y')} dx dx' dy dy'. \quad (1.95)$$

If one assumes that the height function  $h(x, y)$  is symmetric and depends only on the distance  $(x - x', y - y')$  between two points on the surface, one can simplify this equation and calculate one independent surface integral which just introduces the illuminated area of the sample surface  $A$ :

$$\frac{d\sigma}{d\Omega} = \left( \frac{\Delta N_b}{q_z} \right)^2 \frac{A}{\sin \theta} \int_S \langle e^{iq_z[h(0,0)-h(x,y)]} \rangle e^{i(q_x x + q_y y)} dx dy, \quad (1.96)$$

where the angular brackets denote an ensemble average. If one further assumes that the statistics of the height variations are Gaussian one can show that this equals to [60]:

$$\frac{d\sigma}{d\Omega} = \left( \frac{\Delta N_b}{q_z} \right)^2 \frac{A}{\sin \theta} \int_S e^{q_z^2 \langle [h(0,0)-h(x,y)]^2 \rangle / 2} e^{i(q_x x + q_y y)} dx dy. \quad (1.97)$$

The expression  $\langle [h(0,0) - h(x, y)]^2 \rangle$  can be written as

$$\langle [h(0,0) - h(x, y)]^2 \rangle = 2 \langle h^2 \rangle - 2 \langle h(0,0) - h(x, y) \rangle = 2\sigma^2 - 2C(x, y), \quad (1.98)$$

with the *height-height correlation function*  $C(x, y)$ . With this notation the scattering cross section can be divided into a specular and a diffuse part:

$$\frac{d\sigma}{d\Omega} = \left( \frac{d\sigma}{d\Omega} \right)_{spec} * \left( \frac{d\sigma}{d\Omega} \right)_{diff} = \left( \frac{\Delta N_b}{q_z} \right)^2 \frac{A}{\sin \theta} e^{q_z^2 \sigma^2} * \int_S e^{q_z^2 C(x,y)} e^{i(q_x x + q_y y)} dx dy. \quad (1.99)$$

It can be shown by integrating over the solid angle, that the first part resembles the Fresnel reflectivity of a graded interface [60], whereas the second part will have the shape of a peak function with a width that is a function of the inverse lateral coherence length  $1/\zeta$ . In general the diffuse scattering has to be calculated numerically, but for some cases, e.g. fractal surfaces, it may be calculated analytically [60, 67].

In fig. 1.16 is plotted a reflectivity map subject to the inclined and outgoing angles. A specular reflectivity scan corresponds to the diagonal line. The off-specular scattering is usually recorded by keeping the detector in a certain position  $2\theta_f$  and rocking the sample from zero to  $\theta_f$ . This results in a constant  $\theta_i + \theta_f$  and is called *rocking scan*.

In summary, the specular reflectivity does not give any information about the lateral structure of the surface and therefore off-specular measurements have to be performed. It must be emphasized that the theory derived here is limited to the kinematical range, i.e. the first-order Born approximation. For a more accurate description one has to calculate in the DWBA, where refraction is also taken into account. These effects are particularly important close to the total reflection, i.e. if  $\theta_i$  or  $\theta_f$  come close to  $\theta_c$ . However, this takes us beyond the scope of this work and I refer to [67, 62, 68] for more information.

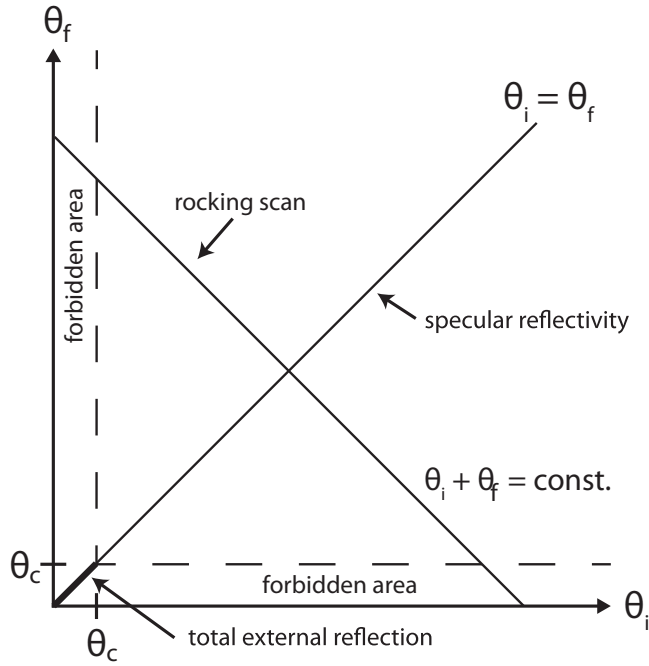


Figure 1.16.: Draft of a specular and a rocking scans, which are usually applied in reflectometry. The x-axis corresponds to the incoming angle and the y-axis to the outgoing one. The forbidden area corresponds to the off-specular region where no reflected intensity can be obtained due to total reflection.

### Grazing Incidence Small Angle Scattering and Grazing Incidence Diffraction

In order to investigate samples with correlations in all three dimensions, but at the same time being surface sensitive, *grazing incidence small angle scattering* (GISAS) or *grazing incidence diffraction* (GID) experiments are performed. These combine the reflection geometry of a reflectivity set-up with recording of the whole scattering pattern including specular, off-specular and diffracted intensities as can be seen in fig. 1.17. The surface sensitivity in that kind of experiments is given by the penetration depth of the impinging wave into the sample. The  $z$ -projection of the transmitted wave  $t(z)$  is given on the right hand side of eq. (1.78). Applying Snellius' law (1.65) and eq. (1.79) in order to translate into the original momentum transfer  $k$  and the incoming angle  $\theta_i$  one gets:

$$t(z) = a_j^- e^{-ikz\sqrt{\theta_i^2 - \theta_c^2 - i\frac{\lambda}{2\pi}\mu}}, \quad (1.100)$$

here  $n^2$  is again approximated by eq. (1.74). Calculating the absolute square of the transmitted wave one gets its intensity:

$$T(z) = |a_j^-|^2 e^{-ikz\frac{1}{\sqrt{2}}\sqrt{(\theta_i^2 - \theta_c^2)^2 + (\frac{\lambda}{2\pi}\mu)^2 - (\theta_i^2 - \theta_c^2)}}. \quad (1.101)$$

Comparing now the transmitted wave intensity with the absorption law (1.62) one can identify the penetration depth in  $z$ -direction  $z_{1/e}$ :

$$z_{1/e} = \frac{\sqrt{2}\lambda}{4\pi} \sqrt{\sqrt{(\theta_i^2 - \theta_c^2)^2 + \left(\frac{\lambda}{2\pi}\mu\right)^2} - (\theta_i^2 - \theta_c^2)}. \quad (1.102)$$

The penetration depth into a silicon substrate for different radiations is plotted in fig. 1.18. The sharp increase in penetration depth at the critical angle makes it possible to tune the surface sensitivity of GID experiments. Especially in the case of neutrons one can probe macroscopical and nanoscopical thin surface layers with the same set-up. The momentum transfers for a monochromatic incoming wavelength  $\lambda$  according to fig. 1.17 are given by:

$$q_x = \frac{2\pi}{\lambda} (\cos \theta_f \cos 2\theta_{in} - \cos \theta_i) \quad (1.103)$$

$$q_y = \frac{2\pi}{\lambda} (\cos \theta_f \sin 2\theta_{in}) \quad (1.104)$$

$$q_z = \frac{2\pi}{\lambda} (\sin \theta_i + \sin \theta_f). \quad (1.105)$$

GISAS measurements thus provide information about all three dimensions of thin films. The length scales probed in a GISAS experiment may be very different though. For typical incident and outgoing angles on the order of one degree and typical wavelengths of several Ångströms, the observable structures in the  $z$ -direction are between 1 - 1000 nm, as for reflectivity measurements. The  $y$ -direction usually offers the same length scale, however, for GID measurements large in-plane angles are used, allowing for atomic

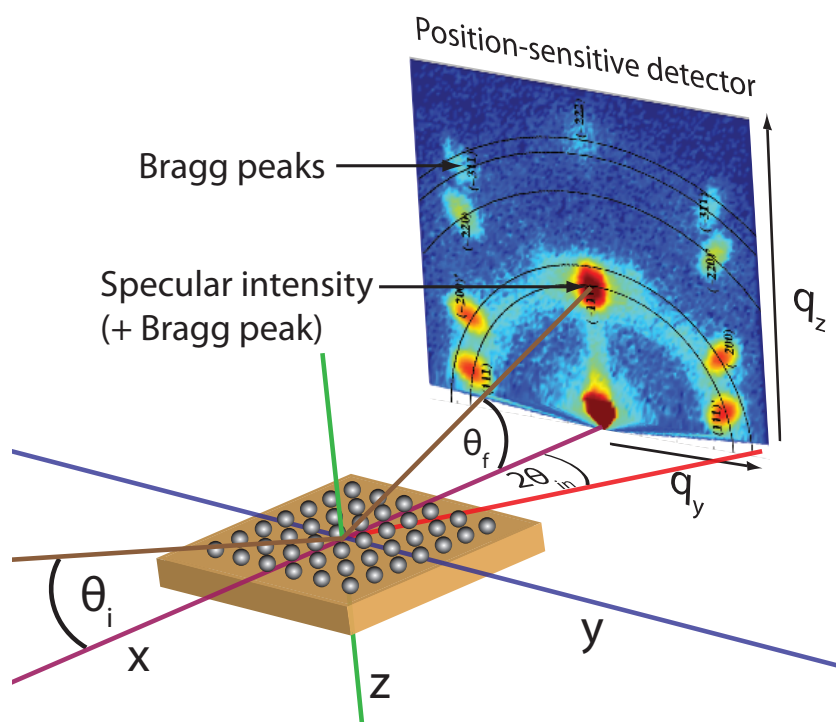


Figure 1.17.: Grazing incidence diffraction set-up.  $\theta_i$  denotes the grazing incident angle and  $\theta_f$  the outgoing one.  $2\theta_{in}$  corresponds to the in-plane diffracted angle. The neutron GISAS (GISANS) pattern was taken from a micellar solution in contact with a solid boundary as studied in appendix C

## 1. Introduction

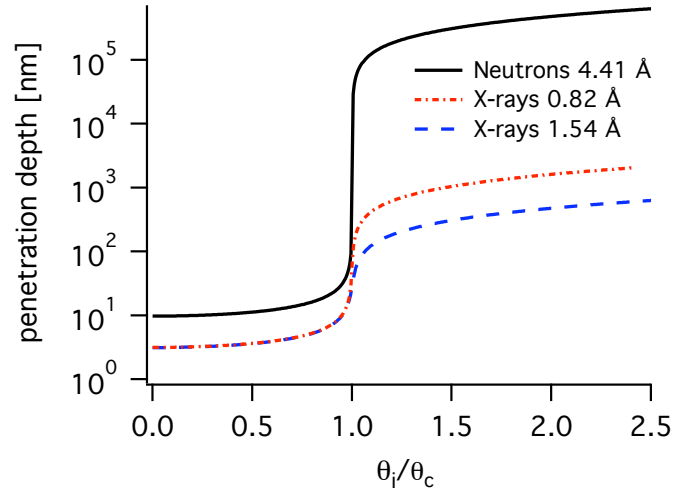


Figure 1.18.: Penetration depth into a silicon surface in log scale for different types of radiation. The x-axis shows the incident angle normalized to the critical angle.

resolution. On the other hand, insertion of typical GISAS angles into the equation (1.103) results in considerably smaller momentum transfers  $q_x$  and thus typical structures on the  $\mu\text{m}$  range can be resolved in x-direction. Therefore, besides the surface sensitivity, GISAS experiments give insight into two different length scales at the same time. This was used in study C, where the crystal lattice of polymer micelles on the nm scale was recorded together with its interface correlation on the  $\mu\text{m}$  scale. For more information about GISAS I refer to [69, 68].

## 2. Experimental

In this chapter an introduction into experimental considerations of reflectometry as well as a description of the neutron and x-ray reflectometers used in this study will be given. As it was mentioned in sec. 1.3.3 only elastic scattering is assumed. This allows two different experimental methods regarding the energy selection of the scattered wave. In the first case the incoming wave is monochromized by a single crystal, which is called *monochromatic* or *angle dispersive* mode. The second possibility is to use a 'white' spectrum of wavelengths impinging on the sample and to analyze the energy of the scattered wave, thus using several wavelengths at the same time. In the case of neutrons this is done by recording the time they need to pass through the experimental set-up. Consequently, this method is called *time-of-flight* (TOF) neutron scattering.

### 2.1. Experimental considerations

#### 2.1.1. Resolution

One of the most challenging aspects of a reflectivity experiment is the use of glancing angles that may be very small. To scan the total reflection edge for example, an instrumental resolution on the order of a tenth of a degree is needed for the wavelengths used in this study. Furthermore, sharp features in the reflectivity, as demonstrated in fig. 1.13(e), are smeared out if the reflection angle is loosely defined. The instrumental resolution is affected by three factors: the first one is the mechanical accuracy in positioning the sample and the detector. Nowadays, this is on the order of a thousandth of a degree and can be neglected. The second parameter is the optical divergence, which is the sum of the incoming beam divergence  $\Delta\theta_i$  and the angular acceptance of the detector  $\Delta\theta_f$  or the pixel size of a two-dimensional detector. The third parameter is the wavelength resolution  $\Delta\lambda$  of the incoming wave. According to eq. (1.105) the specular resolution in q-space  $\Delta q_z$  can be calculated for small angles considering error propagation:

$$\frac{\Delta q_z}{q_z} = \sqrt{\left(\frac{\Delta\theta_i + \Delta\theta_f}{2\theta}\right)^2 + \left(\frac{\Delta\lambda}{\lambda}\right)^2}. \quad (2.1)$$

The wavelength resolution is determined either by the monochromator on angle-dispersive reflectometers or by the length of the neutron pulse and potentially the time resolution of the detector on a time-of-flight reflectometer. If perfect crystals are used, as it is the case on synchrotron sources, the wavelength distribution is of order  $\frac{\Delta\lambda}{\lambda} = 10^{-4}$  and can be neglected in comparison with the angular divergence. At neutron sources,

## 2. Experimental

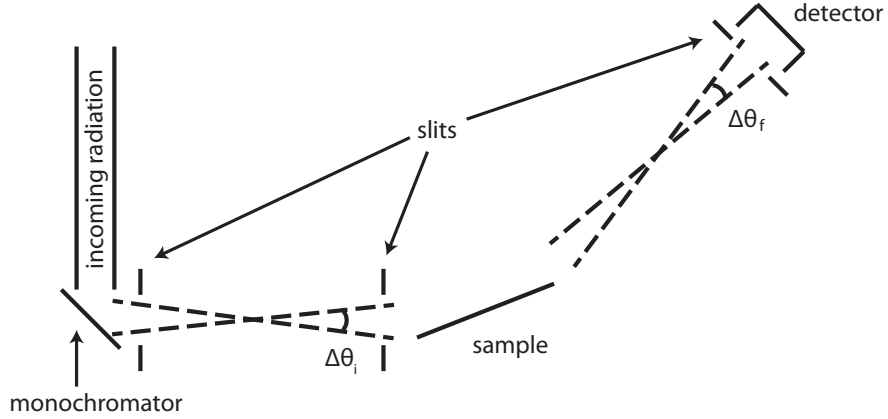


Figure 2.1.: Optics sketch in a reflectometry experiment. For a position-sensitive detector the resolution  $\Delta\theta_f$  is given by the pixel size and the sample-to-detector distance.

however, mosaic crystals are usually used as monochromators. Here the wavelength band is considerably broader and so comparable to the spatial divergence. A similar wavelength resolution is achieved on time-of-flight reflectometers, where the wavelength accuracy is often adjusted to  $10^{-2} < \frac{\Delta\lambda}{\lambda} < 10^{-1}$ .

The spatial divergence is defined by the initial angular spread of the incoming beam, optionally by the monochromator mosaicity and finally by the size of the beam before and after the sample constricted by an arrangement of slits. A sketch of a typical arrangement of slits in a reflectometry experiment is given in fig. 2.1.

In a synchrotron the initial angular spread of the x-ray beam normal to the electron orbit is limited by the opening of the relativistic cone shown in fig. 1.7(b). For an electron energy  $E$  this is given by [67]:

$$\Delta\theta_i = \frac{m_e c^2}{E}, \quad (2.2)$$

with the electron mass  $m_e$  and the speed of light  $c$ . For an energy of 1.5 GeV this corresponds to an angular divergence of  $\Delta\theta_i = 1.9 * 10^{-2}^\circ$  which is often smaller than the detector resolution. Hence, in a synchrotron experiment, the instrumental resolution is mainly defined by the detector resolution and the beam size.

In the simplest case of zero initial beam divergence and equal slits, the angular resolution function resembles a triangular profile. A convolution with a Gaussian distribution of wavelength leads to a wavelength dependent smearing out and eventually the resolution function  $\tilde{R}$  becomes a non-trivial peak function dependent on the momentum transfer  $q_z$ . In most cases, however, it can be approximated by a Gaussian distribution:

$$\tilde{R}(q_z) = \frac{2\pi}{\Delta q_z(q_z)} e^{-(q_z/2\Delta q_z(q_z))^2}. \quad (2.3)$$

This approximation is often used in fitting procedures as described in sec. 2.1.3. In order to further simplify the data analysis, the resolution function is often tuned to have a simple dependence on the momentum transfer  $q_z$ . In the simplest case the resolution is kept constant ( $\Delta q_z = \text{const.}$ ), which can be achieved, for example, on a synchrotron, where the wavelength spread can be neglected, and the slit configuration is kept constant. Another possibility is to ensure a constant resolution relative to the momentum transfer ( $\frac{\Delta q_z}{q_z} = \text{const.}$ ). This is usually done on a time-of-flight reflectometer by keeping the same pulse length ( $\frac{\Delta \lambda}{\lambda} = \text{const.}$ ) and opening of the slits for larger angles to keep  $\Delta \theta / \theta$  constant as well.

In the following the non-specular resolution will be calculated. As in a reflectivity experiment only the momentum transfer perpendicular to the surface is of interest, the beam is usually collimated in the surface plane, whereas the out-of-plane collimation is relaxed. Consequently, correlations in y-direction are not accessible. The resolution in x-direction  $\Delta q_x$  can be calculated from eq. (1.103) via error propagation. If  $\theta_{in} = 0$  and  $\theta_i = \theta_f$  one gets:

$$\Delta q_x = \sqrt{\left(\frac{\Delta \lambda}{\lambda} q_x\right)^2 + \left(\frac{q_z}{2}\right)^2 (\Delta \theta_i^2 + \Delta \theta_f^2)}. \quad (2.4)$$

For grazing incidence small angle scattering (GISAS), momentum transfers in y-direction are recorded as well and thus a reasonable resolution in both directions is needed. The y-resolution for  $\theta_i = \theta_f$  can be calculated similarly by using eq. (1.104):

$$\Delta q_y = \sqrt{\left(\frac{\Delta \lambda}{\lambda} q_y\right)^2 + q_z^2 \left( \left(\frac{\Delta \theta_f \sin 2\theta_{in}}{2}\right)^2 + \left(\frac{\Delta \theta_{in} \cos 2\theta_{in}}{\tan \theta_f}\right)^2 \right)}. \quad (2.5)$$

### 2.1.2. Data correction

Besides the experimental resolution, other corrections have to be taken into account. The first data correction comes from the use of glancing angles. Due to the finite size of the sample the beam height is larger than the sample projection perpendicular to the beam for very small angles. This leads to an overillumination of the sample as depicted in fig. 2.2 and thus not all of the initial beam intensity is reflected. In order to take this circumstance into account the measured intensity has to be corrected up to the angle  $\theta_t$ , where all of the incident beam is reflected. This leads to the correction factor  $\beta$  and is called *footprint correction*:

$$\beta = \begin{cases} \sin \theta_i / \sin \theta_t & \text{for } \theta_i < \theta_t \\ 1 & \text{for } \theta_i \geq \theta_t. \end{cases} \quad (2.6)$$

In fig. 2.3 a sample reflectivity curve before and after footprint correction is shown. As one can see, for small samples, the footprint correction may cover the whole q-range under investigation and thus a false data correction may result in a significant deviation from the real reflectivity. It is noted that the sinusoidal footprint correction is only valid for rectangular beam profiles and samples. For other situations one has to calculate the

## 2. Experimental

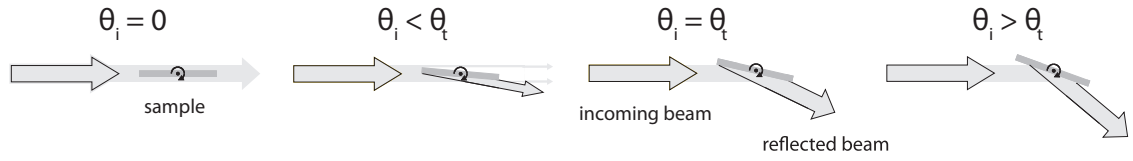


Figure 2.2.: Beam size and sample projection for small angles in a reflectometry experiment [55].

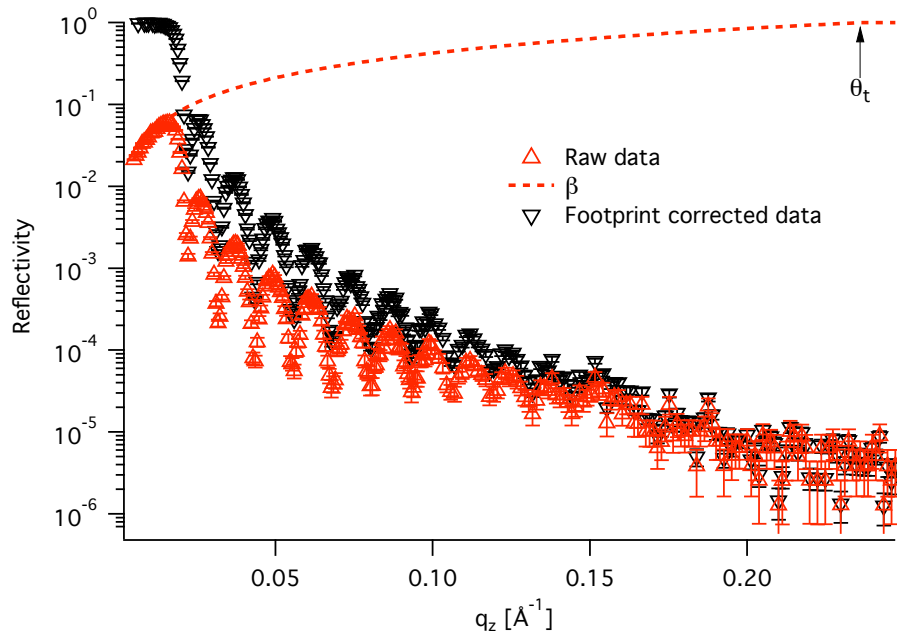


Figure 2.3.: Neutron reflectivity curve on log scale of a 1 cm long silicon block covered with a 50 nm thick deuterated polystyrene layer. The data was recorded on ADAM using a beam height of 0.7 mm.

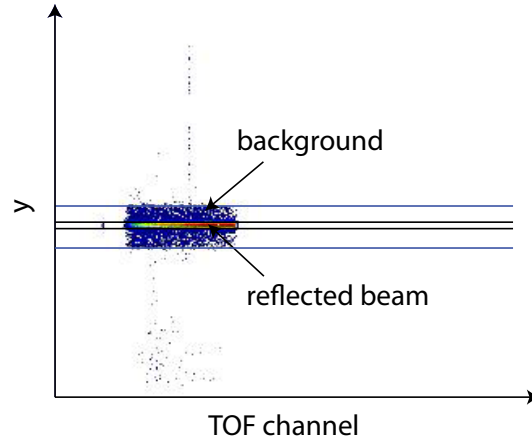


Figure 2.4.: Time-of-flight pattern recorded on the Liquids Reflectometer. The x-axis corresponds to the velocity of the neutrons and the y-axis to the y projection of the 2D-detector image. The black and blue lines mark the limit of the specular signal and the background, respectively.

corresponding footprint via geometrical considerations.

Another data correction that usually has to be applied in reflectometry is the background consideration. Given that the reflected intensity drops according to  $q^{-4}$ , the minimal count rate of the detectors is quickly reached. The latter is limited by noise of the detector electronics and by the radiation background from the sample and the environment. In order to consider this one can either measure the background separately and subtract it from the reflectivity or, if the background is assumed to be constant, it can be modeled in the fitting routine as an additional parameter. When a two-dimensional detector is used, as it is the case on TOF reflectometers for example, the background is always recorded and later subtracted from the signal. In fig. 2.4 a typical TOF pattern is plotted. The bright area denotes high counting rates and corresponds to the specular signal. Around the specular beam an area with lower intensity is visible, which is background scattering from the sample and its mean value is deducted from the reflected intensity during data reduction. Further away there are almost no counts visible, this region corresponds to the environmental background and electronic noise. Obviously, in this case, most of the background comes from the sample itself, hence, it could lead to a false reflectivity if only the constant environmental background is considered.

### 2.1.3. Data fitting

In the course of this work *Motofit* [64] was used throughout the data fitting. *Motofit* is a free available fitting program embedded into the IGOR [70] environment. It is based on the optical matrix method described in sec. 1.3.4 including the possibility of rough interfaces. These are modeled by the *Nevot-Croce* approach [66], which includes

## 2. Experimental

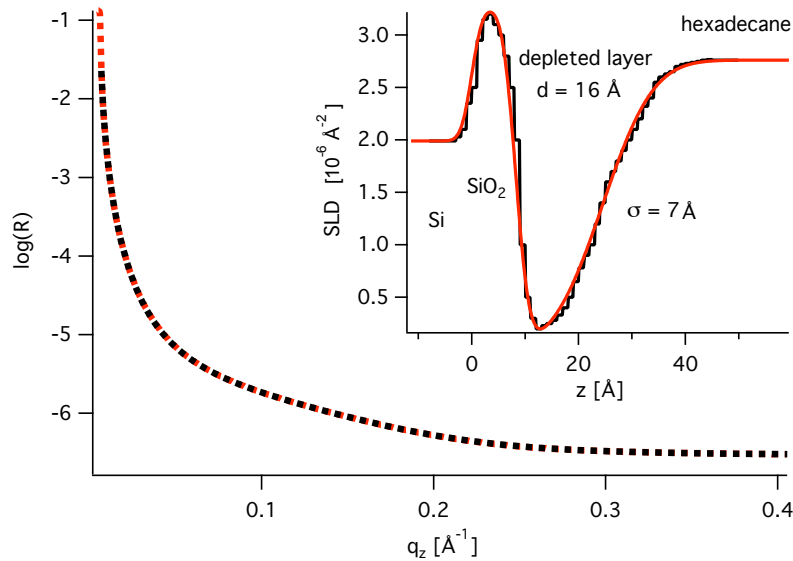


Figure 2.5.: Logarithmic reflectivity curves calculated with Motofit by using the corresponding SLD profiles from the inset. Inset: Typical SLD profiles for a deuterated hexadecane/silicon interface as used in sec. A. The red line shows the profile as calculated by Motofit with Gaussian roughness and the black line denotes a modeled SLD profile using thin slices and zero roughness.

the Nevot-Croce factor from eq. (1.93). Therefore, a Gaussian roughness is assumed between subsequent layers. The advantage of this procedure is that roughnesses are not restricted to values that are much smaller than the corresponding layer thickness. An example is given in fig. 2.5, where a typical scattering length density profile of an interface between deuterated hexadecane and silicon is simulated using rough interfaces as well as modeling the same interface with  $1 \text{\AA}$  thick smooth slices. The resulting reflectivity curves are identical, demonstrating the ability of fitting roughnesses that are comparable to the thickness of the corresponding layer.

The program calculates the reflectivity using four parameters for every layer, namely the thickness  $d$ , the scattering length density (SLD), the absorption (imaginary SLD) and the roughness  $\sigma$ . Thereupon it calculates the variance  $\chi^2$  between the calculated curve and the reflectivity data points and refines the parameters up to the point when it reaches a minimum in  $\chi^2$ . A strong advantage of Motofit is the possibility to fit several reflectivities with different SLD contrasts at the same time. This was used during the present work while simultaneously fitting the neutron and x-ray reflectivity curves of the same sample. It is noted that this is possible only if the reflectivity curves have the same statistical weight in terms of errors and data point density.

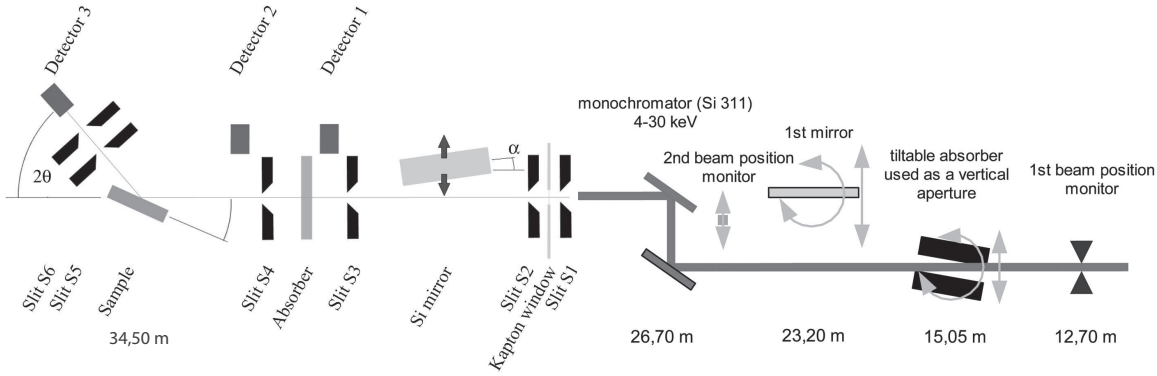


Figure 2.7.: Sketch of the beamline BL 9 at DELTA [71, 72].

## 2.2. Angle dispersive reflectometers

In angle dispersive reflectometers a crystal with a well-defined lattice parameter is used to select a certain wavelength out of the impinging beam. Therefore, one takes advantage of the Bragg law (1.52), which ensures that only one wavelength and its higher harmonics are constructively scattered under a certain angle. In order to maximize the flux, the monochromator crystal is used in reflection geometry, which allows an effective pick-up of the desired energy at a certain angle.

### 2.2.1. Beamline BL9

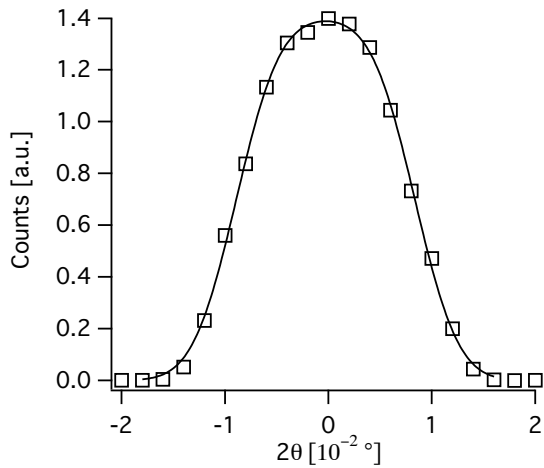


Figure 2.6.: Direct beam measured on the BL9 at DELTA. The errors are smaller than the symbols. The solid line represents a fit using a trapezoidal function with Gaussian borders.

Beamline 9 (BL9) [71, 72] is an x-ray diffractometer at the 1.5 GeV synchrotron Dortmund Elektronenspeicherring-Anlage (DELTA) in Dortmund, Germany. The radiation is extracted in a wiggler (see fig. 1.7(b)) with an energy between 4 - 30 keV. The energy is subsequently selected by two single crystalline silicon monochromators adjusted to the (311) Bragg reflection. This leads to a wavelength resolution of  $\frac{\Delta\lambda}{\lambda} = 10^{-4}$ . A sketch of the beamline is inserted in fig. 2.7. Consequently, the beam is shaped by several slits and passes a variable absorber to avoid overstraining of the detector. To monitor the incident flux two detectors are installed before and after the absorber. After being reflected

## 2. Experimental

from the sample, which is mounted horizontally, the x-rays pass two more slits which reduce the background and define the detector resolution, respectively. For the present study a NaI point-detector was used to record the scattered intensity.

As mentioned in sec. 2.1.1 the experimental resolution on a synchrotron reflectometer is mainly given by the detector resolution. In this study the slit size was adjusted to 0.3 mm which results in  $8.6 \cdot 10^{-3}^\circ$  (FWHM). This corresponds well to the  $\Delta\theta = 8 \cdot 10^{-3}^\circ$  (FWHM) extracted from the direct beam profile shown in fig. 2.6. The measurements for sec. B were performed with a constant slit setting and thus, the experimental resolution  $\Delta q$  was constant as well. The raw reflectivity was obtained by normalizing the detected intensity to the monitor count rate and by dividing by the normalized direct beam intensity. Subsequently, the footprint correction was applied by fitting a sinusoidal increase of the intensity to the totally reflected region and by correcting the data up to the point where the direct beam intensity is reached (see fig. 2.3).

### 2.2.2. ADAM

The Advanced Diffractometer for the Analysis of Materials (ADAM) was a neutron reflectometer with vertical sample geometry located at the Institut Laue-Langevin (ILL) in Grenoble, France [73]. It was dismantled in 2009 and replaced by a new instrument called Super-ADAM, which comprises all features from the old instrument and adds new ones. It was used for the polymer/solid interface structure study presented in sec. B. The neutrons produced in the 56 MW reactor were reflected out of the cold neutron guide from a highly oriented pyrolytic graphite (HOPG) monochromator (002) at a wavelength of 4.41 Å. Due to the low mosaicity of the graphite crystal, the wavelength resolution was  $\Delta\lambda/\lambda = 6 \cdot 10^{-3}$  and therefore ADAM was suitable for high resolution studies. Afterwards the beam passed a cooled beryllium crystal which absorbed wavelengths below 4 Å. This was done to suppress higher order reflected wavelengths of 2.2 Å and 1.1 Å which also fulfill Bragg's law (1.52). The spatial resolution of the incoming beam was given by two collimation slits at a distance of 2102 mm. A drawing of the instrument is included in fig. 2.8. In the configuration used for this study the reflected neutrons flew through another slit and were detected in a  $^3\text{He}$ -pencil-detector. An identical detector was mounted before the second collimation slit in order to monitor the incident flux. In the given experiments constant slit configurations were used. Due to the small wavelength spread the experimental resolution could be approximated to be constant as well. The reflectivity was calculated by the same way as for BL9.

### 2.2.3. V6 Horizontal Reflectometer

The V6 Horizontal Reflectometer is located at the Helmholtz-Zentrum Berlin (HZB) in Berlin, Germany, and uses neutrons from the 10 MW BERII reactor. It was used to investigate the near surface structure of micellar solutions in sec. C. The reflectometer has a similar layout as ADAM and its principle components are sketched in fig. 2.9. The difference in comparison with ADAM is a slightly longer wavelength of 4.66 Å and the horizontal sample geometry. Furthermore, in this work a two-dimensional  $^3\text{He}$ -

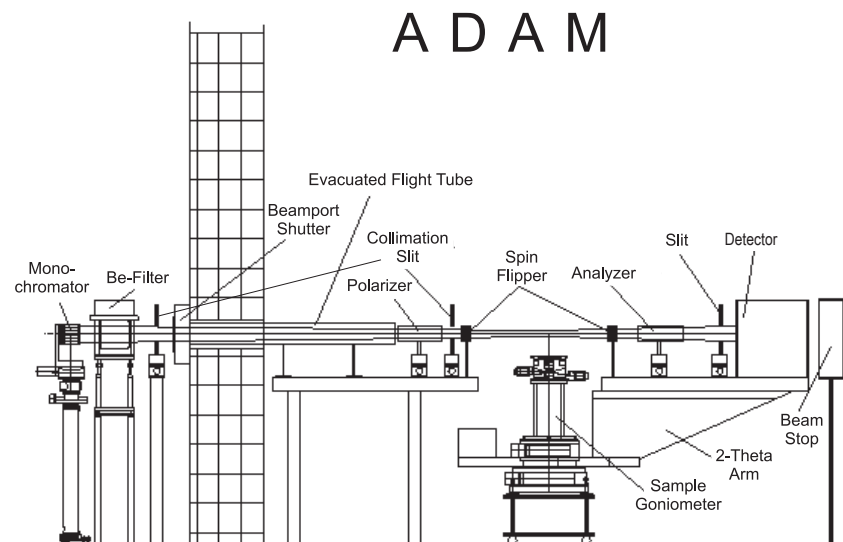


Figure 2.8.: Sketch of the ADAM reflectometer at ILL [74]. The polarizer and analyzer, as well as the spin flippers are optional components for the polarization analysis and were not used in this study.

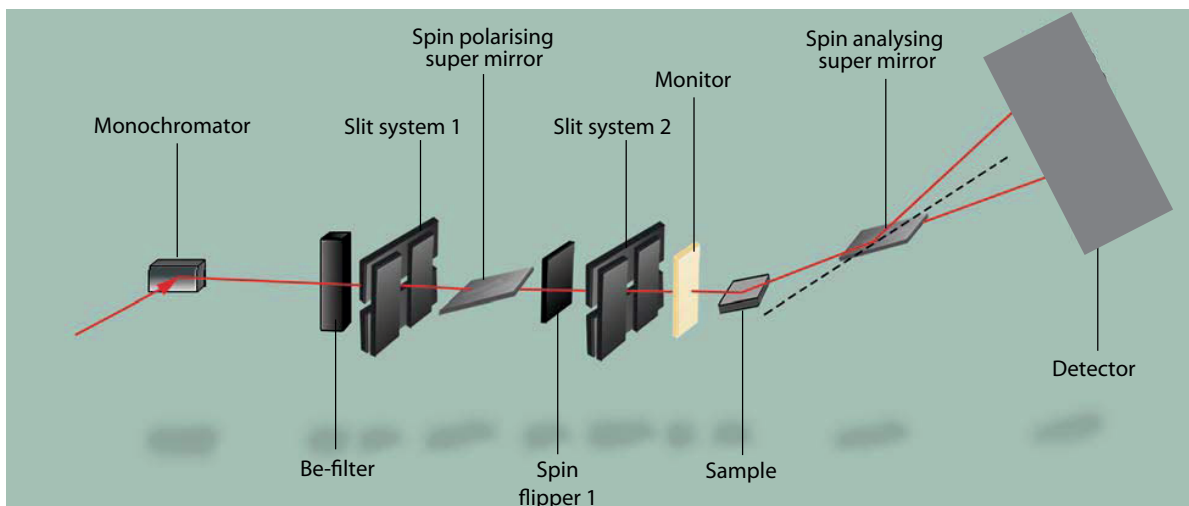


Figure 2.9.: Sketch of the V6 Horizontal Reflectometer at HZB [75]. The polarizer and analyzer, as well as the spin flippers are optional components for the polarization analysis and were not used in this study.

## 2. Experimental

detector was used in order to record Grazing Incidence Small Angle Scattering (GISANS) patterns. The active area of the detector covers  $18 \times 18 \text{ cm}^2$  with a resolution of  $\Delta\theta_f = 0.027^\circ$  for the sample-to-detector distance of 157 cm used in this study. The incoming beam divergence was adjusted by the collimation slits to  $\Delta\theta_z = 0.04^\circ$  normal to the sample surface and  $\Delta\theta_y = 0.22^\circ$  in-plane. With the wavelength spread of  $\Delta\lambda/\lambda = 0.02$  the resulting experimental resolution was  $\Delta q_z = 1.4 \times 10^{-3} \text{ \AA}^{-1}$ ,  $\Delta q_y = 1 \times 10^{-2} \text{ \AA}^{-1}$  and  $\Delta q_x = 7.8 \times 10^{-5} \text{ \AA}^{-1}$ , respectively, at the grazing incident angle  $\theta = 0.85^\circ$  that corresponds to the Bragg peak investigated in sec. C.

### 2.2.4. N-Rex<sup>+</sup>

The neutron reflectometer N-Rex<sup>+</sup> at the Forschungsreaktor München II (FRMII) in Garching, Germany, is similar to the V6 reflectometer. It was utilized for the Grazing Incidence Diffraction (GID) measurements of the hexadecane/solid interface in sec. A. The HOPG monochromator was set to reflect  $4.26 \text{ \AA}$  with a resolution of  $\Delta\lambda/\lambda = 0.02$ . The most important difference in comparison with other reflectometers is the possibility to move the detector arm in the sample surface plane to angles up to  $2\theta_y = 110^\circ$  as can be seen in fig 2.10.

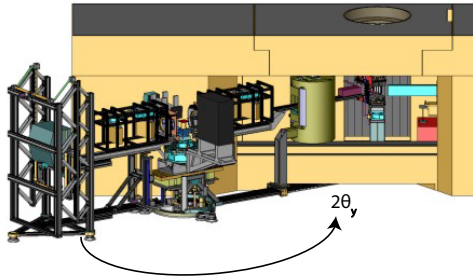


Figure 2.10.: Drawing of the N-Rex<sup>+</sup> reflectometer at the FRMII [76].  $2\theta$  corresponds to the in-plane scattering angle.

This allows GID experiments and thus the investigation of atomic length scales. The in-plane diffraction patterns were recorded with a two-dimensional detector of  $20 \times 20 \text{ cm}^2$  size for two grazing incident angles. The resulting diffraction patterns were obtained by integrating over the reflected beam intensity and by plotting the intensity versus the in-plane momentum transfer  $q_y$ . The neutron beam was  $0.3 \times 15 \text{ mm}^2$  large and the resolution in z-direction for the two incident angles was adjusted to  $\Delta q_z(q_z = 1.3 \times 10^{-2} \text{ \AA}^{-1}) = 2.7 \times 10^{-4} \text{ \AA}^{-1}$  and  $\Delta q_z(q_z = 2.6 \times 10^{-2} \text{ \AA}^{-1}) = 7.2 \times 10^{-4} \text{ \AA}^{-1}$  in order to ensure total reflection for the small incident angle ( $q_c = 1.8 \times 10^{-2} \text{ \AA}^{-1}$ ). The in-plane resolution was  $\Delta\theta_y = 0.15^\circ$ .

## 2.3. Time-of-flight reflectometers

An alternative way to measure the reflectivity of a sample with neutrons is to use a polychromatic beam and to analyze the wavelength of the scattered neutrons. In this way a distinct q-range of the reflectivity curve is measured at a time. In order to resolve the energy of the neutrons, the incoming beam is either pulsed, as it is the case at spallation sources, or a continuous beam is chopped into pulses as depicted in fig. 2.11. The neutrons are reflected by the sample and eventually detected by a time-resolving detector. The data acquisition system is synchronized with the chopper disks, and

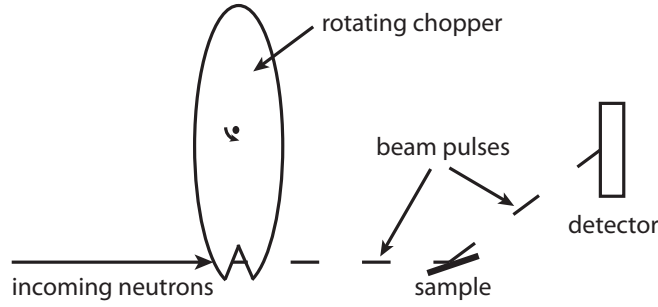


Figure 2.11.: Schematic drawing of a rotating chopper at a continuous source as used for time-of-flight neutron reflectometry.

with the proton-on-target signal at a spallation source, to register the time of flight of the neutrons through the instrument as depicted in fig. 2.12. From the flight time of the neutrons  $T$  one can calculate their wavelength according to eq. 1.24 and 1.25 and, knowing the incident angle onto the sample  $\theta$ , finally the momentum transfer via eq. 1.35:

$$q = \frac{4\pi}{\lambda} \sin \theta = \frac{4\pi m_n L}{hT} \sin \theta. \quad (2.7)$$

In order to inhibit an overlap of neighbor pulses, which can occur when fast neutrons from pulse  $n+1$  overrun slower neutrons from pulse  $n$ , and to allow an adjustable, but constant instrumental resolution on a continuous source, usually several synchronized choppers are used. Additionally, a frame-overlap mirror is often used which reflects neutrons with wavelengths longer than a certain threshold out of the beam.

### 2.3.1. FIGARO

FIGARO is located at the ILL and was used to probe the solid/hexadecane interface described in sec. A. It has a horizontal sample geometry and can use a broad wavelength band between 2 Å and 30 Å provided by the cold source of the ILL reactor. A drawing of the instrument is included in fig. 2.13. The time resolution and wavelength band is shaped by an arrangement of two out of four available choppers plus a frame-overlap mirror. In the configuration we used, the fastest neutrons, which pass through the chopper windows have a wavelength of 2 Å. Their wavelength uncertainty is defined only by the time resolution of the detector. The time resolution of slower neutrons is given by the start time uncertainty and by the detector resolution. In the present set-up the parameters were chosen to ensure a constant  $\Delta\lambda/\lambda=5.6\%$  resolution for all wavelengths. In order to suppress an overlap of adjacent pulses the frame-overlap mirror was adjusted to reflect neutrons slower than  $\lambda = 30$  Å out of the beam. The two-dimensional detector is 50\*25 cm<sup>2</sup> large and has a resolution of 2\*7 mm<sup>2</sup>. During the experiment the relative experimental resolution was constantly  $\Delta q/q = 0.06$ .

## 2. Experimental

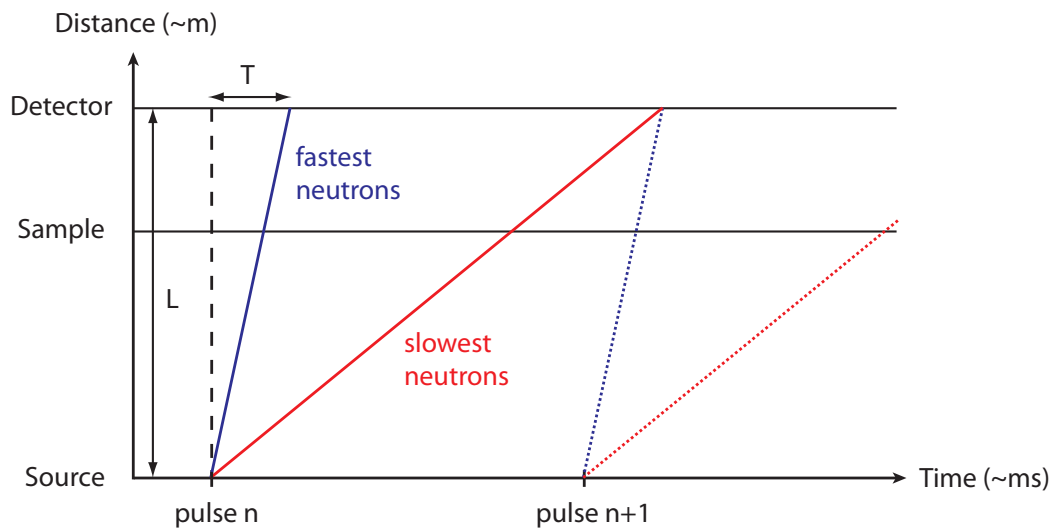


Figure 2.12.: Time-distance diagram for an elastic TOF measurement. The neutron pulses are produced at a distinct time in a spallation source, or by a chopper at a continuous source and are detected by a time-resolving detector after a certain time  $T$ . Neighbor pulses have to be scheduled as shown in order to prevent an overrun of the slowest neutrons of one pulse (red line) by the fastest neutrons of the next pulse (dashed blue line).

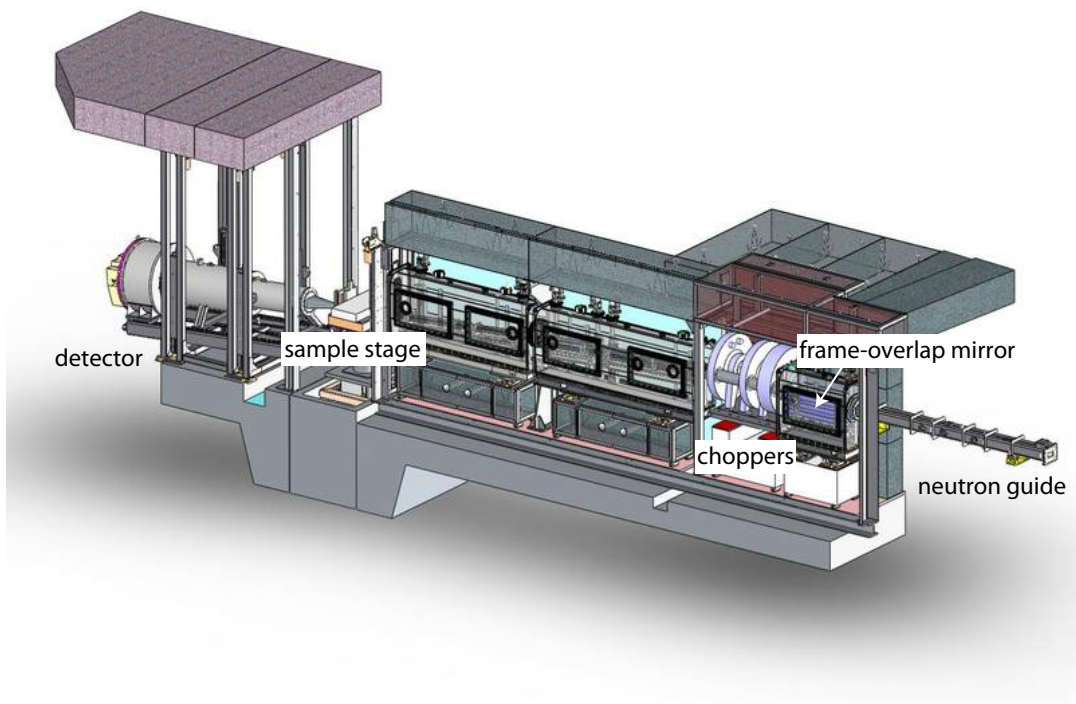


Figure 2.13.: Drawing of the FIGARO reflectometer at ILL [77].

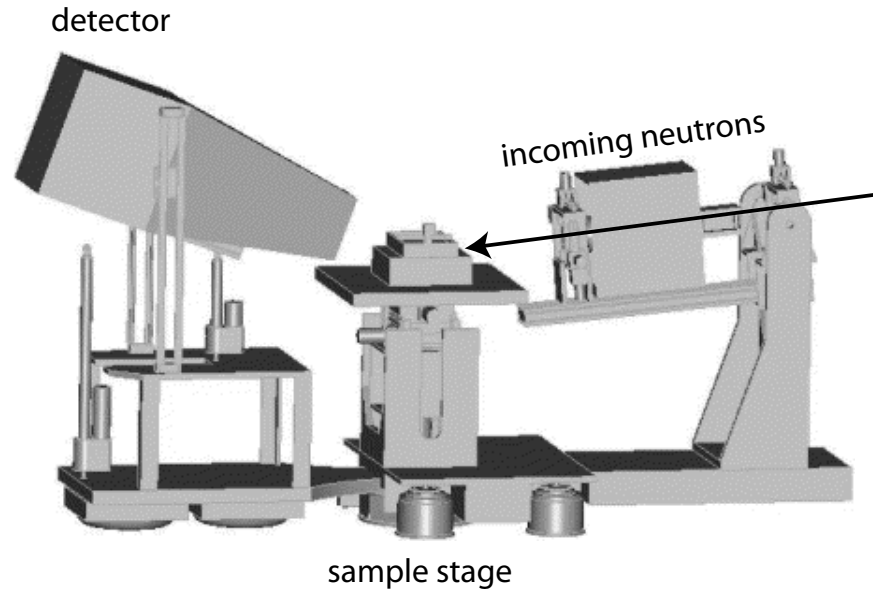


Figure 2.14.: Drawing of the Liquids Reflectometer at the SNS [78].

### 2.3.2. Liquids Reflectometer

The Liquids Reflectometer was used together with FIGARO for the investigation of the solid/hexadecane interface. It was fed with neutrons from the cold source of the Spallation Neutron Source (SNS) in Oak Ridge, Tennessee, USA, that was operating at 600 kW at that time. Similarly to FIGARO it has a horizontal sample geometry but due to the 60 Hz repetition rate of the spallation source, its optimal wavelength band is a narrower 2.5 - 5.5 Å. A frame-overlap mirror and three neutron choppers are synchronized with the pulsed source in order to suppress overlapping of adjacent pulses [78]. The wavelength resolution is given by the pulse rate and the distance between the source and the detector. The SNS operates at 60 Hz and the Liquids Reflectometer detector is situated 15.25 m away from the moderator, which results in a resolution of  $\Delta\lambda/\lambda = 0.5\%$  [78]. A drawing of the instrument is given in fig. 2.14. The 20\*20 cm<sup>2</sup> position-sensitive detector has a symmetric resolution of 1.3 mm and is 1.5 m away from the sample. The resulting resolution was set to a constant value of  $\Delta q/q = 0.044$ .

## 2.4. Comparison of the neutron reflectometers

In this section the advantages and disadvantages of the neutron reflectometers used in this work are briefly discussed. The first matter of choice is whether to use the time-of-flight technique or a monochromatic reflectometer. A strong advantage of the time-of-flight reflectometer FIGARO is the possibility to adjust the wavelength resolution in a wide range, which can give an enormous gain in flux, if the experiment does not

require high resolution. Due to the use of a relatively low momentum transfer resolution of 6% in the study presented in appendix A, the first half of the reflectivity curves, obtained by using two incident angles solely, was recorded within three hours. For the same  $q$ -range the reflectivity scans on the ADAM reflectometer took roughly 12 h. In this case the average resolution was 3.5%. It is mentioned that the wavelength resolution function of the FIGARO reflectometer is in general not a Gaussian distribution due to the asymmetry of the Maxwell distribution of wavelengths coming from the cold source. Thus the resultant reflectivity curves should be fitted accordingly. A conventional fitting procedure described in sec. 2.1.3 can be only applied if  $\frac{\Delta\lambda}{\lambda} \ll \frac{\Delta\theta}{\theta}$  holds valid or if the reflectivity curve does not incorporate sharp features as for example Bragg-peaks or frequent Kiessig-oscillations.

At the Liquids Reflectometer the situation is a little bit different. Due to the pulsed source the quite high wavelength resolution of  $\Delta\lambda/\lambda = 0.5\%$  cannot be changed. On the other hand, because of the coupling of the choppers with the pulsed source, a high fraction of the available neutrons are used, opposite to FIGARO, where the biggest part of neutrons is discarded while chopping the continuous beam from the reactor. Thus the complete reflectivity curves from appendix A were measured within 2 h on the Liquids Reflectometer, which was therefore the fastest reflectometer used in this work. Like on FIGARO the wavelength resolution function is not symmetric, but if the angular resolution is kept much larger, as it is usually the case on pulsed sources, the contribution of the wavelength spread is negligible.

A drawback of the measurements at the spallation source was the varying neutron flux due to beam instabilities. As can be seen in fig. 2.15 the power of the spallation source, proportional to the neutron flux, heavily fluctuated on the time scale of a measurement. This may lead to systematic errors when normalizing the reflectivity, and that is why measurements with an alternating neutron flux have to be discarded in the data analysis. Consequently, the neutron flux at the Liquids Reflectometer has to be constantly monitored and affected scans have to be repeated manually, or excluded in the data reduction process. This provokes an inconvenience, which is not present at a stable reactor source. Moreover, if a slow dynamical process has to be monitored, for example the micellar lattice reconstruction from study C, a spallation source is a bad choice, because a stable beam cannot be guaranteed during the dynamical process under investigation.

Concerning the monochromatic reflectometers, N-Rex<sup>+</sup> showed a very similar performance as ADAM regarding time and  $q$ -range. The neutron loss due to the better wavelength resolution on ADAM was counterbalanced by the higher power of the ILL reactor (56 MW) as compared to the 30 MW of the FRMII. The advantage of N-Rex<sup>+</sup> was the possibility to move the detector arm in the sample plane to large angles, which enabled the GID experiments presented in appendix D. The V6 reflectometer at HZB had the lowest neutron flux among the reflectometers we used. It was chosen because of its horizontal sample geometry and the possibility to mount a bulky rheometer onto the sample stage.

In summary, the appropriate reflectometer should be chosen according to the sample geometry, the needed momentum transfer range and resolution, and the need for a stable neutron beam. Presumably the Liquids Reflectometer showed the best performance

## 2. Experimental

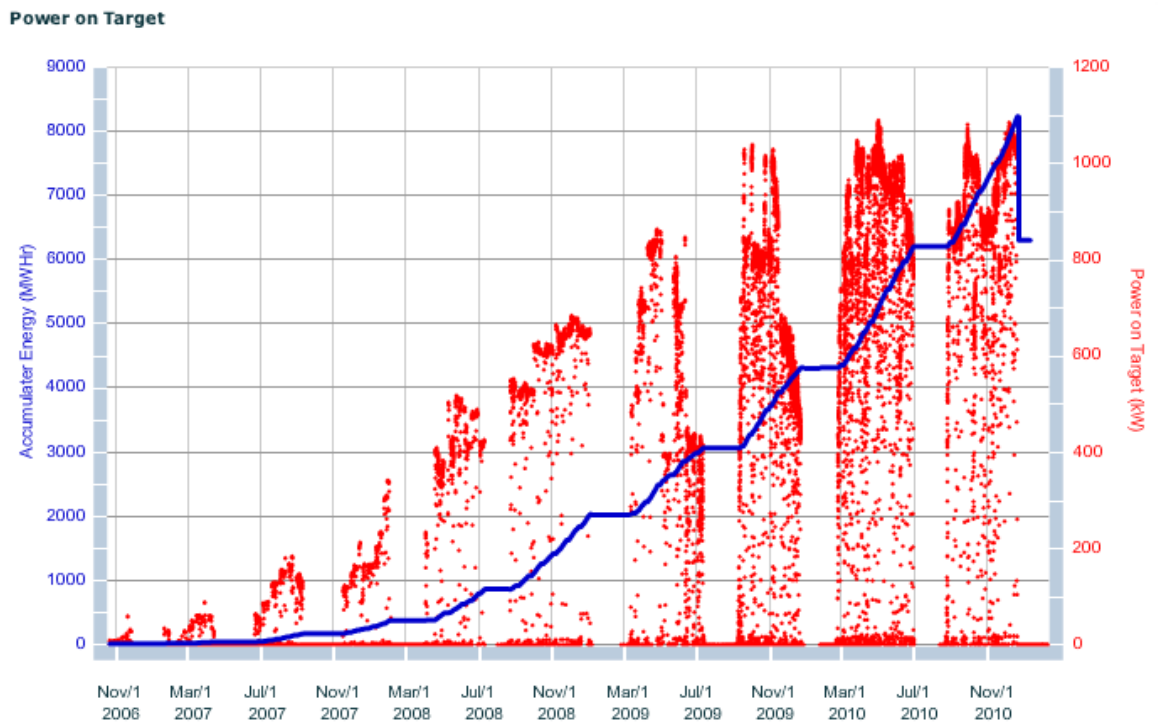


Figure 2.15.: History of the power focussed on the target (red points) and the accumulated energy (blue line) at the Spallation Neutron Source since its first operation [79].

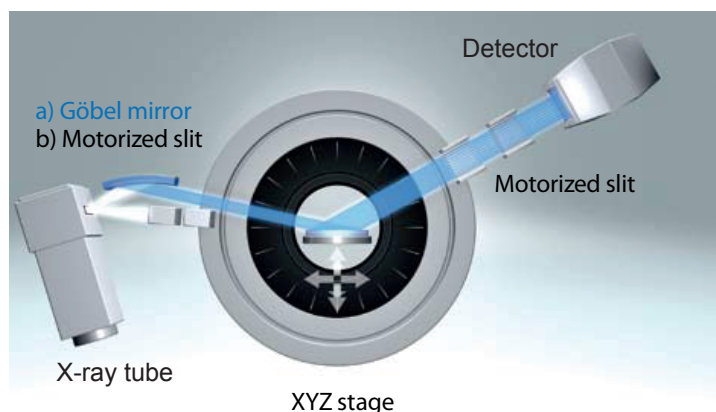


Figure 2.16.: Sketch of the laboratory reflectometers used in this work [80].

for specular reflectivity scans, but with the disadvantage of an unstable neutron beam, which may be crucial for some applications. Among monochromatic instruments, ADAM outperformed the others, especially if high resolution was needed.

## 2.5. Laboratory reflectometers

Two commercial x-ray reflectometers were used to pre-characterize the silanized substrates dedicated for neutron reflectometry. In sec. A the X'Pert Pro from Panalytical, Almelo, Netherlands, was used and in sec. B the D8 by Bruker, Madison, Wisconsin, USA. The configuration of both instruments is essentially the same and is sketched in fig. 2.16. The x-rays are produced by a copper x-ray tube and subsequently are parallelized by a Göbel-mirror. This results in a monochromatic beam with  $1.54 \text{ \AA}$  wavelength and a resolution of  $\Delta\lambda/\lambda = 8 * 10^{-4}$ . This is considerably smaller than the angular divergence of  $0.029^\circ$  and thus, the experimental resolution of  $\Delta q = 4.1 * 10^{-3} \text{ \AA}^{-1}$  can be considered to be constant.

## 2.6. Contact angle measurements

Generally speaking three different contact angles may be determined in order to characterize a solid/liquid interface. The first two are called *dynamic contact angles*. They correspond to the maximal and minimal droplet size which can be achieved by adding or removing liquid with a syringe without changing the interfacial area as depicted in fig. 2.17. The dynamic contact angles, measured in this way, are called *advancing* and *receding* contact angles, respectively, and the difference is referred to as the *contact angle hysteresis*. This hysteresis is an indicator for the chemical heterogeneity of the surface and a small value denotes a homogeneous surface [82].

The third contact angle often quoted is the *static contact angle* and corresponds to the

## 2. Experimental

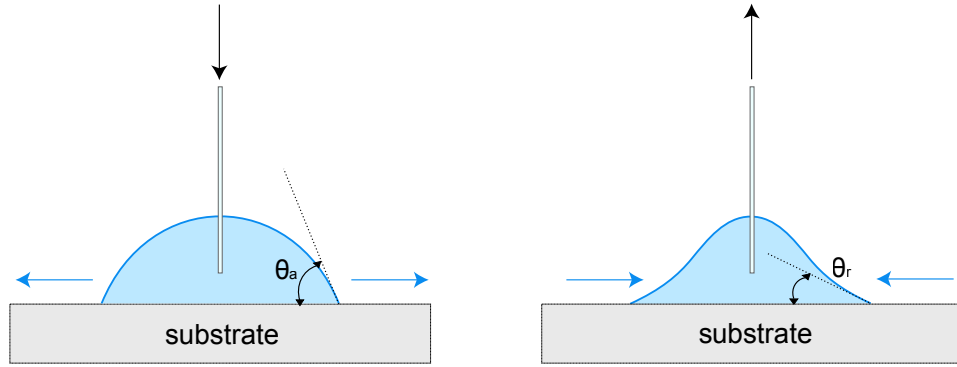


Figure 2.17.: Drawing of a dynamic contact angle measurement [81].  $\theta_a$  and  $\theta_r$  correspond to the advancing and receding contact angles, respectively.

average of the two dynamic contact angles. The static contact angle  $\theta$  of a liquid droplet on a solid surface is related to the interfacial energy  $\gamma_{sl}$  through the following equation [82]:

$$\gamma_{sl} = \gamma_{sg} - \gamma_{lg} \cos \theta, \quad (2.8)$$

where  $\gamma_{lg}$  is the surface tension of the liquid and  $\gamma_{sg}$  the free surface energy.

# 3. Results and Discussion

## 3.1. Hexadecane on functionalized surfaces

In appendix A a neutron and x-ray reflectivity study on the interface of hexadecane and different functionalized solid substrates is included. As in the previous work [45] a density depleted layer was found between the bulk liquid and the solid wall. For one system the temperature dependence was recorded, which revealed a slight increase of the depletion layer while heating. This dependence of the depletion layer on temperature was already observed before at the water/SAM interface and predicted by MD simulations [44]. This showed the intrinsic nature of the depletion layer and contradicts propositions in literature that the depletion layer is an artifact of contamination [83].

The comparison of the depleted layers for several alkane/solid interfaces displayed a systematic increase of the amount of density depletion with rising interfacial energy. This is opposite to the relation between density depletion and interfacial energy observed in a recent MD simulation [18] and XRR study [43] of water. Another difference between the depletion in water and in alkanes is their extension. A common parameter to compare the resulting depletion effects is the depletion distance  $d_2$  [84]:

$$d_2 = \int_{liquid\ phase} \left(1 - \frac{\rho(z)}{\rho_{bulk}}\right) dz, \quad (3.1)$$

where  $\rho(z)$  denotes the density of the depleted liquid at a distance  $z$  from the interface and  $\rho_{bulk}$  represents the bulk liquid density.  $d_2$  reduces the smeared-out density profile of the depletion to a step-like function that represents an equivalent layer of zero density. In the water MD study [18] the resulted depletion distances are below one molecular diameter and arise from a real density depletion without a significant alignment of the water molecules. The depletion distances are well in accord with recent XRR measurements [49, 85, 39, 40, 42, 43], however the molecular configuration could not be resolved. In contrast to water, the hexadecane molecule can undergo a conformational change additionally to the orientational degrees of freedom. Nevertheless, the hydrocarbon chain is usually coiled in the liquid state and the diameter of such a hexadecane coil is 5.37 Å [86]. This is comparable to the depletion distance measured at the substrate covered with octadecyl-trichlorosilane (OTS), which was the system with the lowest surface energy. For higher surface energies the depletion distances reached more than 20 Å and were thus considerably thicker than one coiled molecule's diameter. Hence, and because of the opposite dependence on interfacial energy, the origin of the depleted layer in hexadecane has to be fundamentally different from the one in water. The next point in this study was the discussion of a possible connection of the depletion layer and surface slip, as mentioned in sec. 1.2.3. Surface slip of hexadecane was

### 3. Results and Discussion

observed in contact with several surfaces [87, 29, 28], including OTS, but the reported slip lengths vary importantly as can be seen in fig. 1.4(a). However, in all cases the slip length increased for lower interfacial energy. Recalling the systematic decrease of the depletion layer established in the first part of this study, a stronger depletion thus suppresses slippage of hexadecane. This contradicts the explanation of surface slip due to a density reduced interface layer. In order to underline this conclusion, the expected slip lengths appearing from the viscosity change in the depletion layer were calculated as proposed in ref. [30]. As it was already observed before [45], the calculated slip lengths are much shorter than any of the numbers reported in literature. This favors another explanation of surface slip, which implies molecular ordering of the near surface molecules. If the depletion observed for hexadecane is connected with an alignment of the molecules, the difference in comparison to water could be explained. Indeed, in contrast to water, MD simulation studies predict a configurational change of oligomeric liquids near solid walls [13].

Another aim of this study was to inspect the influence of shear stress on the depletion layer. In case of OTS the depletion did not change with shear, as it was already observed before for similar systems [45]. For the largest depletion layer though, observed at chemically cleaned silicon, a slight influence on shear was found. But due to a possible contamination with water this finding has to be treated with care.

## 3.2. Polystyrene on silanized surfaces

The work included in appendix B comprises a neutron and x-ray reflectivity study on the interface of polystyrene and self-assembled monolayers. As in the above study a density depleted region was found at both SAMs under investigation. Certainly the depletion distances for PS were much shorter than for hexadecane, viz.  $1.44 \pm 0.01 \text{ \AA}$  for the PS/OTS interface and  $1.13 \pm 0.04 \text{ \AA}$  at the dodecyl-trichlorosilane (DTS). Due to the high resolution of the reflectivity experiments, distinct features of the depletion layer could be resolved. It was shown, that the adjacent polymer forms a smooth interface on a molecular level. The results indicated that the adjacent polystyrene chains built a well-ordered configuration with the phenyl rings pointing to the SAM. Additionally they followed the orientation of the SAM tails which were standing upright in case of the OTS and were tilted by  $30^\circ$  relatively to the surface in case of DTS. Thus we could show that the depletion layer at the PS/SAM interface is not due to a density depletion, but is a result of a configurational change of the adjacent polymer.

The structural study of this system was motivated by previous dewetting studies performed on the same system, which revealed slip lengths on the  $\mu\text{m}$ -scale [21, 22, 23, 24, 25]. Moreover, a huge difference in slip velocity was found between the PS/DTS and the PS/OTS interfaces, although both systems do not differ, apart from a slightly longer tail length of the OTS, which consists of 18 hydrocarbons, as compared to DTS with 12 hydrocarbons. Similar to hexadecane, the depleted layer in PS, found in the present study, is too thin to explain the large slip length. Besides, the tiny difference in depletion distance between the OTS and the DTS cannot lead to a

slip length difference of one order of magnitude as observed in the dewetting studies. The only difference between the two systems was the tilt angle of the SAM tails and the consequential in-plane correlation of the surface roughness. Rocking scans of the silanized surfaces showed a well-ordered OTS surface, whereas the DTS roughness was uncorrelated on a length scale of several tenths of  $\mu\text{m}$ . This testified that the surface correlation is the major parameter determining the slip length in this system.

The replication of the surface order in the contacting PS chain segments, which was indicated by the results, is corroborated by recent MD simulations [20], where the crystal structure of the solid boundary was repeated within the first liquid layer. Moreover, in these simulations the slip velocity of the adjacent liquid was reduced for stronger ordering, which is in compliance with our observation of a shorter PS slip length at the more well-ordered OTS surface compared to DTS.

### 3.3. Complex Liquid

The third study in appendix C deals with a grazing incidence neutron small angle scattering study of the interface between an aqueous triblock copolymer solution in contact with a hydrophobic and a hydrophilic solid wall. Triblock copolymer solutions are known to show a rich phase behavior dependent on temperature and the concentration of the ingredients [88]. In the composition used in this study the molecules aggregated to micelles and the micelles arranged in a lattice structure. This lattice structure gave rise to Bragg-peaks in the GISANS pattern, which was recorded while shearing the solution *in situ*. It was observed that the lattice structure broke when shear stress was applied, but rearranged within several hours when the shear stress was turned off again. In order to quantify the in-plane correlation of the reconstructed lattice, rocking scans were performed around the brightest Bragg-peak in the GISANS pattern during the rearrangement process. It could be shown that for the hydrophobic surface the crystalline arrangement of polymer micelles was entirely reconstructed in about two hours, but for the hydrophilic substrate only partial reconstruction was achieved after 5 hours. This demonstrates accelerated dynamics at the hydrophobic surface, which fits well to the observation of surface slip in other lyophobic systems.

### 3.4. First GID experiments on crystalline hexadecane

The last study in appendix D summarizes, among others, the results from the works A and C. Additionally, it includes a grazing incidence neutron diffraction study for the hexadecane/solid interface, which could be the key to a direct observation of a conformational change of the near surface liquid. In order to check the ability of this kind of experiments, crystalline hexadecane was investigated, which gave a pronounced Bragg-peak in the in-plane diffraction pattern. For a large grazing incident angle, corresponding to a penetration depth of some  $\mu\text{m}$  (see sec. 1.3.4), this crystalline peak was clearly visible. But as soon as the incident angle was below the angle of total external reflection,

### *3. Results and Discussion*

which corresponds to a penetration of only several nm, the crystalline peak vanished. It was demonstrated that the signal-to-background ratio for that kind of experiment is on the order of  $10^{-3}$  and thus not resolvable on current neutron sources.

# 4. Conclusion and Summary

## 4.1. Conclusion

The investigations of the density depleted layer at hexadecane/solid interfaces reveal a systematic increase of the amount of density depletion with interfacial energy. This is opposite to the relation between density depletion and interfacial energy observed in water [18, 43]. Moreover, the thickness of the depleted layers differs considerably between water and hexadecane. Hence, the origin of the depleted layer in hexadecane has to be fundamentally different from the one in water. A deeper insight into the depletion layer is found for polystyrene at SAMs, studied in appendix B. In this case distinct features of the depletion were resolved, that can be achieved only by a well-ordered orientation of the adjacent PS chain segments. This ultimately proves, that the depletion layer cannot be generally attributed to a mere density reduction, but may have its origin in molecular arrangements close to the solid wall.

These structural data are subsequently compared to surface slip measurements on the same samples. As it was already observed before [45], the depletion layer at hexadecane/solid interfaces is too thin to explain the slip lengths reported in literature, if the depletion layer is assumed as a mere density reduction. This is even more obvious for the depletion distances at the interfaces of PS and SAMs. Especially, the huge difference in slip length between the PS/DTS and the PS/OTS interfaces [25] cannot be explained by the tiny difference in depletion. All the other parameters listed in sec. 1.2.3, that could possibly influence slippage, are the same. The only difference between the two SAMs is the in-plane correlation of the surface roughness. This testifies that the surface order is the major parameter determining the slip length in this system and is in line with recent MD simulations of oligomers [20]. Hence, in addition to the presently discussed influences on slip, like roughness or interfacial energy [3, 4], one has to take into account the surface correlation as a crucial parameter and revisit slip length measurements concerning this property.

A direct example of the surface influence on the interfacial structure and dynamics is given in appendix C. It is shown that for low interfacial energy the crystalline arrangement of polymer micelles at the interface is entirely reconstructed in about two hours after being disturbed by shear stress. For a high interfacial energy substrate only partial reconstruction is achieved after 5 hours. This is in line with the general observation of stronger slippage on low interfacial energy substrates.

In conclusion, the results expose various cases, where a conformational change of the near surface liquid tends to be the crucial parameter for large slip lengths determined experimentally. This interpretation is consistent with a larger slip length observed for

#### 4. Conclusion and Summary

hexadecane, whose molecules can be elongated, in comparison with squalane, a more symmetric molecule [28]. Locally, surface-induced molecular layering of flowing liquids has been observed in confined propanol [36] using a SFA, and in eicosane [35] using an AFM after quenching the flowing alkane. However, these techniques require direct contact with the interfacial liquid and thus perturb the system. A possibility to resolve the interfacial structure without disturbing the sample is grazing incidence neutron diffraction (GIND). An attempt of a GIND experiment on the hexadecane/solid interface is introduced in appendix D. Unfortunately, the flux of present neutron sources is insufficient to perform such types of experiment.

### 4.2. Summary

In order to establish a connection between the interfacial structure at liquid/solid interfaces and surface slip, the present work includes surface sensitive neutron and x-ray scattering studies on several systems, where surface slip was observed by other techniques. Additionally, a grazing incidence neutron small angle scattering (GISANS) study was performed, where the dynamics of a complex liquid near solid boundaries were resolved. The results, regarding the interface between hexadecane and functionalized solid surfaces, disproved the proposed explanation of surface slip by a density reduced layer at the solid surface. A systematic connection between the extent of the density reduction and the interfacial energy was found, which contradicts the amount of surface slip in this system.

In a second study the depletion layer between polystyrene (PS) and self-assembled monolayers (SAM) could be explained by a conformational change in the adjacent polymer chain segments. A replication of the surface order in the contacting polymer layer was indicated by the results, which demonstrated the strong influence of the solid boundary on the interfacial structure. Moreover, the large difference in slippage of PS on various SAMs, reported in literature, could be linked to a difference of the in-plane order at the interface.

The influence of the substrate on the interfacial structure of the adjacent liquid and eventually on the near-surface dynamics could be demonstrated in a third study, revealing the arrangement of polymer micelles at the interface.

In summary, the presented results showed that surface order plays a significant role in slippage and that this parameter should be considered when searching for the molecular origin of surface slip. This corroborates on-going theoretical and experimental work claiming molecular alignment as the main origin of large surface slip.

# 5. Outlook

## 5.1. Depletion layer

The combination of neutron and x-ray reflectometry exercised in the studies A and B holds the ability to determine the chemical composition of the depleted layers at solid/liquid interfaces. This could be established as a standard routine when investigating depletion layers and could give a clear answer to the present discussion, whether parts of the solid surface are incorporated in the depletion layer of water or not [39, 40, 42, 43].

## 5.2. Thin polymer films

The study from appendix B investigating the interface structure of thin polystyrene films opens a wide range of possible extensions. First of all, dynamic measurements of the PS/SAM systems revealed a strong dependence of the slip length on temperature [25]. It can be easily checked whether this dynamical change is accompanied by a structural change of the interface, by performing reflectivity measurements on a series of PS/OTS interfaces, annealed at different temperatures.

Simultaneously, the PS/teflon interface could be investigated by the same method. This system shows temperature independent slip lengths in the range of the ones for OTS at high temperatures [89]. The teflon surface is amorphous and thus cannot induce a long-range correlation in the adjacent PS. The density-reduced layer should consequently disappear according to our explanation.

Another continuation would be the use of long PS chains in contact with teflon. It could be recently shown that the entanglement density of PS with a high molecular weight is reduced close to a solid teflon surface [26]. It is of fundamental interest to verify, whether this entanglement reduction is connected with a real density reduction. This is clearly a job for reflectometry and the accomplishment of this study is already under progress in collaboration with the group of Prof. K. Jacobs.

Finally other polymers apart from PS could be investigated in the same way. Polymethylmethacrylate (PMMA) for example has a different molecular structure than PS and shows slippage on top of solid surfaces too [89]. The changed form of the PMMA molecules should have an impact on the interfacial structure and could consequently be compared to the amount of surface slip.

### 5.3. In situ rheometry

The possibility of combining rheology with neutron reflectometry is demonstrated in study C. This technique offers new research areas for neutron reflectometry like e.g. the investigation of polymer/polymer interfaces under shear stress. An interesting phenomenon in these systems is the so-called stick-slip transition, which involves a rapid change of the slip length in these systems when a threshold shear rate is reached [90]. The origin of the stick-slip transition is supposed to lie in a configurational change at the polymer/polymer interface and could be well investigated by the proposed method. Another fundamental effect that could be investigated in this way is shear-thinning of polymer melts. By examining the interface between polymer chains chemically grafted to a solid substrate, and an identical polymer melt, a possible structural change could be observed when bringing the system into the shear-thinning region.

In appendix D some preparative measurements concerning the mechanical stability of end-grafted polymer brushes are shown. It comes out that the polymer brushes can be damaged by the shear stress if the torque is too high. Thus caution has to be exercised when electing the molecular weight, temperature and shear rate. A recently proposed high torque rheometer dedicated for *in situ* reflectometry experiments [91] can therefore not be used for chemically bonded polymers.

A possibility to bypass this sample damaging is the use of oscillating shear rates. The frequency and amplitude could be tuned in order to determine the critical value for the ripping off of the grafted polymer. A further application of oscillating shear stress includes viscoelastic samples. The transition from elastic to viscous behavior could be linked to the interface structure in a controlled manner. Moreover, the time resolution in oscillatory measurements could be significantly improved in comparison with steady shear, which could be useful for the observation of dynamic processes as the one included in appendix C.

## 6. Zusammenfassung

Um eine Verbindung zwischen der Struktur von flüssig/fest-Grenzflächen und dem Phänomen des Wandgleitens von Flüssigkeiten herzustellen, wurden im Rahmen der vorliegenden Arbeit grenzflächensensitive Neutronen- und Röntgenstreustudien an Systemen durchgeführt, bei denen mit anderen Methoden Wandgleiten beobachtet wurde. Zusätzlich wurden Neutronen-Kleinwinkelmessungen unter streifendem Einfall (GISANS) durchgeführt, bei denen die Grenzflächendynamik einer komplexen Flüssigkeit aufgelöst wurde.

Die Resultate an der Grenzfläche zwischen Hexadekan und funktionalisierten Oberflächen zeigten, dass die Dichtereduzierung an der Grenze zwischen Flüssigkeit und einer festen Wand nicht ausreicht, um die beobachteten Wandgleiteffekte zu erklären. Eine systematische Verbingung zwischen dem Grad der Dichteverarmung und der Grenzflächenenergie konnte aufgedeckt werden, die dem Auftreten von Wandgleiten durch eine Verarmungszone widerspricht.

In einer zweiten Studie gelang es die Dichteverarmung zwischen Polystyrol (PS) und selbstgeordneten Monolagen (SAM) durch eine Konformationsänderung der anliegenden Polymersegmente zu erklären. Es wurden Indizien einer Reproduzierung der Oberflächenordnung in der ersten Schicht der Polymerschmelze gefunden, die den großen Einfluss der Oberfläche auf die anliegende Flüssigkeit zeigten. Des Weiteren konnte der Unterschied in der Oberflächenkorrelation zweier silanisierter Substrate mit einem großen Unterschied in der Gleitlänge von Polystyrol in Verbindung gebracht werden.

Der starke Einfluss der Grenzfläche auf die Struktur und auch die Dynamik der angrenzenden Flüssigkeit wurde in einer dritten Studie demonstriert, bei der die Anordnung von Polymermizellen an festen Grenzflächen aufgelöst wurde.

Zusammenfassend zeigten die Resultate, dass die Oberflächenordnung einen wesentlichen Einfluss auf das Wandgleiten von Flüssigkeiten haben kann und deshalb sollte diese auf der Suche nach dem molekularem Ursprung des Wandgleitens miteinbezogen werden. Das bestätigt aktuelle theoretische und experimentelle Arbeiten, die molekulare Ordnung als Hauptursache des Wandgleitens sehen.



# Bibliography

- [1] T. M. Squires and S. R. Quake, “Microfluidics: Fluid physics at the nanoliter scale,” *Reviews of Modern Physics*, vol. 77, no. 3, p. 977, 2005.
- [2] T. Thorsen, S. Maerkl, and S. Quake, “Microfluidic large-scale integration,” *Science*, vol. 298, no. 5593, pp. 580–584, 2002.
- [3] C. Neto, D. Evans, E. Bonaccorso, H. Butt, and V. Craig, “Boundary slip in newtonian liquids: A review of experimental studies,” *Reports on Progress in Physics*, vol. 68, no. 12, pp. 2859–2897, 2005.
- [4] E. Lauga, M. P. Brenner, and H. A. Stone in *Springer Handbook of Experimental Fluid Mechanics* (C. Tropea, A. L. Yarin, and J. F. Foss, eds.), Springer, 2007.
- [5] L. D. Landau and E. M. Lifshitz, *Hydrodynamics*, vol. 4 of *Theoretical Physics*. first ed., 1953.
- [6] C. Gerthsen and H. Vogel, *Physik*. Springer, 17 ed., 1993.
- [7] D. Bernoulli, *Hydrodynamica*. 1738.
- [8] C. A. Coulomb, *Mémoires relatifs à la physique*. Société Française de Physique, Paris, 1784.
- [9] C. L. M. H. Navier *Mémoires de l’Académie royale des sciences de l’institut de France*, vol. 6, pp. 389–440, 1823.
- [10] P. G. de Gennes, “Viscometric flows of tangled polymers,” *Comptes rendus hebdomadaires de séances de l’Académie des sciences Série B*, vol. 288, no. 14, pp. 219–220, 1979.
- [11] S. Wang, “Molecular transitions and dynamics at polymer/wall interfaces: Origins of flow instabilities and wall slip,” in *Polymers in confined environments*, vol. 138 of *Adv. Polymer Sci.*, pp. 227–275, Springer, 1999.
- [12] O. Bäumchen and K. Jacobs, “Slip effects in polymer thin films,” *Journal of Physics - Condensed Matter*, vol. 22, no. 3, 2010.
- [13] M. J. Stevens, M. Mondello, G. S. Grest, S. T. Cui, H. D. Cochran, and P. T. Cummings, “Comparison of shear flow of hexadecane in a confined geometry and in bulk,” *The Journal of Chemical Physics*, vol. 106, no. 17, pp. 7303–7314, 1997.

## Bibliography

- [14] J.-L. Barrat and L. Bocquet, “Large slip effect at a non-wetting fluid-solid interface,” *Physical Review Letters*, vol. 82, no. 23, pp. 4671–4674, 1999.
- [15] S. Gupta, H. Cochran, and P. Cummings, “Shear behavior of squalane and tetracosane under extreme confinement .1. model, simulation method, and interfacial slip,” *The Journal of Chemical Physics*, vol. 107, no. 23, pp. 10316–10326, 1997.
- [16] S. Gupta, H. Cochran, and P. Cummings, “Shear behavior of squalane and tetracosane under extreme confinement .2. confined film structure,” *The Journal of Chemical Physics*, vol. 107, no. 23, pp. 10327–10334, 1997.
- [17] N. Priezjev, A. Darhuber, and S. Troian, “Slip behavior in liquid films on surfaces of patterned wettability: Comparison between continuum and molecular dynamics simulations,” *Physical Review E*, vol. 71, no. 4, Part 1, p. 041608, 2005.
- [18] D. M. Huang, C. Sendner, D. Horinek, R. R. Netz, and L. Bocquet, “Water slippage versus contact angle: A quasiversal relationship,” *Physical Review Letters*, vol. 101, no. 22, p. 226101, 2008.
- [19] C. Sendner, D. Horinek, L. Bocquet, and R. R. Netz, “Interfacial water at hydrophobic and hydrophilic surfaces: Slip, viscosity, and diffusion,” *Langmuir*, vol. 25, no. 18, pp. 10768–10781, 2009.
- [20] N. V. Priezjev, “Relationship between induced fluid structure and boundary slip in nanoscale polymer films,” *Physical Review E*, vol. 82, no. 5, p. 051603, 2010.
- [21] R. Fetzer, K. Jacobs, A. Münch, B. Wagner, and T. Witelski, “New slip regimes and the shape of dewetting thin liquid films,” *Physical Review Letters*, vol. 95, no. 12, p. 127801, 2005.
- [22] R. Fetzer, M. Rauscher, A. Münch, B. A. Wagner, and K. Jacobs, “Slip-controlled thin-film dynamics,” *Europhysics Letters*, vol. 75, no. 4, pp. 638–644, 2006.
- [23] R. Fetzer, A. Münch, B. Wagner, M. Rauscher, and K. Jacobs, “Quantifying hydrodynamic slip: A comprehensive analysis of dewetting profiles,” *Langmuir*, vol. 23, no. 21, pp. 10559–10566, 2007.
- [24] R. Fetzer and K. Jacobs, “Slippage of newtonian liquids: Influence on the dynamics of dewetting thin films,” *Langmuir*, vol. 23, no. 23, pp. 11617–11622, 2007.
- [25] O. Bäumchen, R. Fetzer, A. Münch, B. Wagner, and K. Jacobs, “Comprehensive analysis of dewetting profiles to quantify hydrodynamic slip,” in *Proceeding of the IUTAM Symposium on Advances in Micro- and Nanofluidics* (M. Ellero, X. Hu, J. Fröhlich, and N. Adams, eds.), Springer, 2009.
- [26] O. Bäumchen, R. Fetzer, and K. Jacobs, “Reduced interfacial entanglement density affects the boundary conditions of polymer flow,” *Physical Review Letters*, vol. 103, no. 24, p. 247801, 2009.

- [27] T. Schmatko, H. Hervet, and L. Léger, “Effect of nanometric-scale roughness on slip at the wall of simple fluids,” *Langmuir*, vol. 22, no. 16, pp. 6843–6850, 2006.
- [28] T. Schmatko, H. Hervet, and L. Léger, “Friction and slip at simple fluid-solid interfaces: The roles of the molecular shape and the solid-liquid interaction,” *Physical Review Letters*, vol. 94, no. 24, p. 244501, 2005.
- [29] J. Cho, B. Law, and F. Rieutord, “Dipole-dependent slip of newtonian liquids at smooth solid hydrophobic surfaces,” *Physical Review Letters*, vol. 92, no. 16, p. 166102, 2004.
- [30] O. I. Vinogradova, “Drainage of a thin liquid film confined between hydrophobic surfaces,” *Langmuir*, vol. 11, p. 2213, 1995.
- [31] S. Granick, Y. Zhu, and H. Lee, “Slippery questions about complex fluids flowing past solids,” *Nature Materials*, vol. 2, no. 4, pp. 221–227, 2003.
- [32] S. Heidenreich, P. Ilg, and S. Hess, “Boundary conditions for fluids with internal orientational degrees of freedom: Apparent velocity slip associated with the molecular alignment,” *Physical Review E*, vol. 75, no. 6, Part 2, p. 066302, 2007.
- [33] J.-L. Barrat and L. Bocquet, “Influence of wetting properties on hydrodynamic boundary conditions at a fluid/solid interface,” *Faraday Discussions*, vol. 112, pp. 119–127, 1999.
- [34] A. Berker, S. Chynoweth, U. Klomp, and Y. Michopoulos, “Nonequilibrium molecular-dynamics (NEMD) simulations and the rheological properties of liquid normal-hexadecane,” *Journal of the Chemical Society - Faraday Transactions*, vol. 88, no. 13, pp. 1719–1725, 1992.
- [35] C. Drummond, N. Alcantar, and J. Israelachvili, “Shear alignment of confined hydrocarbon liquid films,” *Physical Review E*, vol. 66, no. 1, Part 1, pp. 1–6, 2002.
- [36] G. Sun, E. Bonaccorso, V. Franz, and H. Butt, “Confined liquid: Simultaneous observation of a molecularly layered structure and hydrodynamic slip,” *The Journal of Chemical Physics*, vol. 117, no. 22, pp. 10311–10314, 2002.
- [37] W. A. Hamilton, L. Porcar, and L. J. Magid, “Using neutron reflectometry and reflection geometry ‘near-surface’ SANS to investigate surfactant micelle organization at a solid-solution interface,” *Physica B: Condensed Matter*, vol. 357, no. 1-2, pp. 88–93, 2005.
- [38] M. Maccarini, “Water at solid surfaces: A review of selected theoretical aspects and experiments on the subject,” *Biointerphases*, vol. 2, no. 3, pp. MR1–MR15, 2007.
- [39] B. M. Ocko, A. Dhinojwala, and J. Daillant, “Comment on ‘How water meets a hydrophobic surface’,” *Physical Review Letters*, vol. 101, no. 3, p. 039601, 2008.

## Bibliography

- [40] A. Poynor, L. Hong, I. K. Robinson, S. Granick, P. A. Fenter, and Z. Zhang, “Poynor et al. reply,” *Physical Review Letters*, vol. 101, no. 3, p. 039602, 2008.
- [41] M. Mezger, S. Schöder, H. Reichert, H. Schröder, J. Okasinski, V. Honkimäki, J. Ralston, J. Bilgram, R. Roth, and H. Dosch, “Water and ice in contact with octadecyl-trichlorosilane functionalized surfaces: A high resolution x-ray reflectivity study,” *The Journal of Chemical Physics*, vol. 128, no. 24, p. 244705, 2008.
- [42] M. Mezger, F. Sedlmeier, D. Horinek, H. Reichert, D. Pontoni, and H. Dosch, “On the origin of the hydrophobic water gap: An x-ray reflectivity and md simulation study,” *Journal of the American Chemical Society*, vol. 132, no. 19, pp. 6735–6741, 2010.
- [43] S. Chattopadhyay, A. Uysal, B. Stripe, Y.-g. Ha, T. J. Marks, E. A. Karapetrova, and P. Dutta, “How water meets a very hydrophobic surface,” *Physical Review Letters*, vol. 105, no. 3, p. 037803, 2010.
- [44] M. Maccarini, R. Steitz, M. Himmelhaus, J. Fick, S. Tatur, M. Wolff, M. Grunze, J. Janecek, and R. R. Netz, “Density depletion at solid-liquid interfaces: A neutron reflectivity study,” *Langmuir*, vol. 23, no. 2, pp. 598–608, 2007.
- [45] M. Wolff, B. Akgun, M. Walz, A. Magerl, and H. Zabel, “Slip and depletion in a newtonian liquid,” *Europhysics Letters*, vol. 82, no. 3, pp. 1–5, 2008.
- [46] J. W. G. Tyrrell and P. Attard, “Images of nanobubbles on hydrophobic surfaces and their interactions,” *Physical Review Letters*, vol. 87, no. 17, p. 176104, 2001.
- [47] R. Steitz, T. Gutberlet, T. Hauss, B. Klösgen, R. Krastev, S. Schemmel, A. C. Simonsen, and G. H. Findenegg, “Nanobubbles and their precursor layer at the interface of water against a hydrophobic substrate,” *Langmuir*, vol. 19, no. 6, pp. 2409–2418, 2003.
- [48] D. A. Doshi, E. B. Watkins, J. N. Israelachvili, and J. Majewski, “Reduced water density at hydrophobic surfaces: Effect of dissolved gases,” *Proceedings of the National Academy of Sciences of the United States of America*, vol. 102, no. 27, pp. 9458–9462, 2005.
- [49] M. Mezger, H. Reichert, S. Schöder, J. Okasinski, H. Schröder, H. Dosch, D. Palms, J. Ralston, and V. Honkimäki, “High-resolution in situ x-ray study of the hydrophobic gap at the water-octadecyl-trichlorosilane interface,” *Proceedings of the National Academy of Sciences of the United States of America*, vol. 103, no. 49, pp. 18401–18404, 2006.
- [50] W. C. Röntgen, “Ueber eine neue Art von Strahlen,” *Aus den Sitzungsberichten der Würzburger Physik.-medic. Gesellschaft*, pp. 137–147, 1895.
- [51] J. Chadwick *Nature*, vol. 129, p. 312, 1932.

- [52] S. Gerth, “Strukturen Polymer-dekorierter Grenzflächen,” Master’s thesis, Friedrich-Alexander-Universität Erlangen-Nürnberg, 2008.
- [53] E. M. McMillan, “The synchrotron—a proposed high energy particle accelerator,” *Physical Review*, vol. 68, no. 5-6, pp. 143–144, 1945.
- [54] A. C. Thompson, ed., *X-ray data booklet*. Lawrence Berkeley National Laboratory, University of California, Berkeley, California, USA, 2009.
- [55] D. Meier, “Neutronenstreuung an dynamischen Flüssigkeiten,” Master’s thesis, Ruhr-Universität Bochum, 2007.
- [56] A. J. Dianoux and G. Lander, eds., *Neutron data booklet*. 2003.
- [57] L. D. Landau and E. M. Lifshitz, *Non-Relativistic Quantum Mechanics*, vol. 3 of *Theoretical Physics*. fourth ed., 1989.
- [58] V. F. Sears, “Neutron scattering lengths and cross sections,” *Neutron News*, vol. 3, no. 3, pp. 26–37, 1992.
- [59] G. L. Squires, *Introduction to the Theory of Thermal Neutron Scattering*. Cambridge University Press, 1978.
- [60] J. Als-Nielsen and D. McMorrow, *Elements of Modern X-ray Physics*. 2001.
- [61] M. Born and E. Wolf, *Principles of Optics*. Cambridge University Press, 7 ed., 2003.
- [62] J. Daillant and A. Gibaud, eds., *X-ray and Neutron Reflectivity - Principles and Applications*, vol. 770 of *Lect. Notes Phys*. Springer, 2009.
- [63] L. Parratt, “Surface studies of solids by total reflection of x-rays,” *Physical Review*, vol. 95, no. 2, pp. 359–369, 1954.
- [64] A. Nelson, “Co-refinement of multiple-contrast neutron/x-ray reflectivity data using motofit,” *Journal of Applied Crystallography*, vol. 39, no. Part 2, pp. 273–276, 2006.
- [65] M. Wolff, *Struktur und Dynamik komplexer Flüssigkeiten*. PhD thesis, Friedrich-Alexander-Universität Erlangen-Nürnberg, 2003.
- [66] L. Nevot and P. Croce, “Characterization of surfaces by grazing x-ray reflection - application to study of polishing of some silicate-glasses,” *Revue de Physique Appliquée*, vol. 15, no. 3, pp. 761–779, 1980.
- [67] M. Tolan, *X-Ray Scattering from Soft-Matter Thin Films, -Materials Science & Basic Research -, STMP*. Springer, 1998.

## Bibliography

- [68] H. Zabel, K. Theis-Bröhl, and B. P. Toperverg, *Novel Techniques for Characterizing and Preparing Samples*, vol. 3 of *Handbook of Magnetism and Advanced Magnetic Materials*, ch. Polarized Neutron Reflectivity and Scattering from Magnetic Nanostructures and Spintronic Materials, p. 1237. John Wiley & Sons, 2007.
- [69] M. Wolff, A. Magerl, and H. Zabel, “Structure of polymer micelles close to the solid interface - a grazing incidence small angle neutron scattering study,” *The European Physical Journal E*, vol. 16, no. 2, pp. 141–145, 2005.
- [70] “<http://www.wavemetrics.com>.”
- [71] M. Paulus, R. Fendt, C. Sternemann, C. Gutt, H. Hövel, M. Volmer, M. Tolan, and K. Wille, “An internet-based synchrotron experiment for students measuring the x-ray magnetic circular dichroism of a PtFe alloy,” *Journal of Synchrotron Radiation*, vol. 12, no. 2, pp. 246–250, 2005.
- [72] C. Krywka, M. Paulus, C. Sternemann, M. Volmer, A. Remhof, G. Nowak, A. Nefedov, B. Poter, M. Spiegel, and M. Tolan, “The new diffractometer for surface x-ray diffraction at beamline BL9 of DELTA,” *Journal of Synchrotron Radiation*, vol. 13, no. Part 1, pp. 8–13, 2006.
- [73] M. Wolff, K. Zhernenkov, and H. Zabel, “Neutron reflectometry with ADAM at the ILL: Present status and future perspectives,” *Thin Solid Films*, vol. 515, no. 14, pp. 5712–5715, 2007.
- [74] H. Zabel and K. Theis-Bröhl, “Polarized neutron reflectivity and scattering studies of magnetic heterostructures,” *Journal of Physics: Condensed Matter*, vol. 15, no. 5, p. S505, 2003.
- [75] M. Gierlings, M. J. Prandolini, H. Fritzsche, M. Gruyters, and D. Riegel, “Change and asymmetry of magnetization reversal for a Co/CoO exchange-bias system,” *Physical Review B*, vol. 65, no. 9, p. 092407, 2002.
- [76] “<http://www.mf.mpg.de/en/abteilungen/dosch/frmii/index.shtml>.”
- [77] “<http://www.ill.eu>.”
- [78] J. F. Ankner and C. Rehm, “Time-dependent measurements at the SNS liquids reflectometer,” *Physica B: Condensed Matter*, vol. 336, no. 1-2, pp. 68 – 74, 2003.
- [79] “<http://neutrons.ornl.gov>.”
- [80] “<http://www.bruker-axs.de>.”
- [81] “<http://en.wikipedia.org>.”
- [82] J. F. Joanny and P. G. de Gennes, “A model for contact angle hysteresis,” *Simple views on condensed matter*, p. 457, 1984.

- [83] Y.-S. Seo and S. Satija, “No intrinsic depletion layer on a polystyrene thin film at a water interface,” *Langmuir*, vol. 22, no. 17, pp. 7113–7116, 2006.
- [84] S. Mamatkulov, P. Khabibullaev, and R. Netz, “Water at hydrophobic substrates: Curvature, pressure, and temperature effects,” *Langmuir*, vol. 20, no. 11, pp. 4756–4763, 2004.
- [85] A. Poynor, L. Hong, I. K. Robinson, S. Granick, Z. Zhang, and P. A. Fenter, “How water meets a hydrophobic surface,” *Physical Review Letters*, vol. 97, no. 26, p. 266101, 2006.
- [86] X. Wu, E. Sirota, S. Sinha, B. Ocko, and M. Deutsch, “Surface crystallization of liquid normal-alkanes,” *Physical Review Letters*, vol. 70, no. 7, pp. 958–961, 1993.
- [87] D. Chan and R. Horn, “The drainage of thin liquid-films between solid-surfaces,” *The Journal of Chemical Physics*, vol. 83, no. 10, pp. 5311–5324, 1985.
- [88] G. Wanka, H. Hoffmann, and W. Ulbricht, “Phase-diagrams and aggregation behavior of poly(oxyethylene)-poly(oxypropylene)-poly(oxyethylene) triblock copolymers in aqueous-solutions,” *Macromolecules*, vol. 27, no. 15, pp. 4145–4159, 1994.
- [89] O. Bäumchen, *Fluidics of Thin Polymer Films - Boundary Conditions and Interfacial Phenomena*. PhD thesis, Universität des Saarlandes, 2010.
- [90] L. Léger, “Friction mechanisms and interfacial slip at fluid-solid interfaces,” *Journal of Physics - Condensed Matter*, vol. 15, no. 1, Sp. Iss. SI, pp. S19–S29, 2003.
- [91] L. A. Sasa, E. J. Yearley, C. F. Welch, M. A. Taylor, R. D. Gilbertson, C. Hammeter, J. Majewski, and R. P. Hjelm, “The Los Alamos Neutron Science Center neutron rheometer in the cone and plate geometry to examine tethered polymers/polymer melt interfaces via neutron reflectivity,” *Review of Scientific Instruments*, vol. 81, no. 5, p. 055102, 2010.



# A. Depletion at Solid-Liquid Interfaces: Flowing Hexadecane on Functionalized Surfaces

*Journal of Chemical Physics* **134**, 64711 (2011)

Authors: P. GUTFREUND<sup>1,2</sup>, M. WOLFF<sup>3</sup>, M. MACCARINI<sup>2</sup>, S. GERTH<sup>4</sup>, J. F. ANKNER<sup>5</sup>, J. BROWNING<sup>5</sup>, C. E. HALBERT<sup>5</sup>, H. WACKLIN<sup>2</sup>, H. ZABEL<sup>1</sup>

<sup>1</sup>Ruhr-Universität Bochum, 44780 Bochum, Germany

<sup>2</sup>Institut Laue-Langevin, BP 156, 38042 Grenoble, France

<sup>3</sup>Material Science, Department of Physics, Uppsala University, 75121 Uppsala, Sweden

<sup>4</sup>Lehrstuhl für Kristallographie und Strukturphysik, Universität Erlangen-Nürnberg, 91058 Erlangen, Germany

<sup>5</sup>Spallation Neutron Source, Oak Ridge National Laboratory, Oak Ridge, Tennessee, USA

*Author contributions: M. Wolff designed research. The samples were prepared by P. Gutfreund, S. Gerth and M. Maccarini. The experiments were performed by P. Gutfreund under the supervision of M. Wolff, J. F. Ankner, J. Browning, C. E. Halbert and H. Wacklin. Data analysis was performed by P. Gutfreund. The article was written by P. Gutfreund under the supervision of M. Wolff, M. Maccarini and H. Zabel.*

## Depletion at solid/liquid interfaces: Flowing hexadecane on functionalized surfaces

Philipp Gutfreund,<sup>1,2,a)</sup> Max Wolff,<sup>3,b)</sup> Marco Maccarini,<sup>2</sup> Stefan Gerth,<sup>4</sup> John F. Ankner,<sup>5</sup> Jim Browning,<sup>5</sup> Candice E. Halbert,<sup>5</sup> Hanna Wacklin,<sup>2</sup> and Hartmut Zabel<sup>1</sup>

<sup>1</sup>*Institut für Festkörperphysik, Ruhr-Universität Bochum, 44780 Bochum, Germany*

<sup>2</sup>*Institut Laue-Langevin, 38042 Grenoble, France*

<sup>3</sup>*Materials Science, Department of Physics and Astronomy, Uppsala University, 75121 Uppsala, Sweden*

<sup>4</sup>*Lehrstuhl für Kristallographie und Strukturphysik, Universität Erlangen-Nürnberg, 91058 Erlangen, Germany*

<sup>5</sup>*Spallation Neutron Source, Oak Ridge National Laboratory, Oak Ridge, Tennessee 37831, USA*

(Received 19 September 2010; accepted 10 January 2011; published online 14 February 2011)

We present a neutron reflectivity study on interfaces in contact with flowing hexadecane, which is known to exhibit surface slip on functionalized solid surfaces. The single crystalline silicon substrates were either chemically cleaned Si(100) or Si(100) coated by octadecyl-trichlorosilane (OTS), which resulted in different interfacial energies. The liquid was sheared *in situ* and changes in reflectivity profiles were compared to the static case. For the OTS surface, the temperature dependence was also recorded. For both types of interfaces, density depletion of the liquid at the interface was observed. In the case of the bare Si substrate, shear load altered the structure of the depletion layer, whereas for the OTS covered surface no effect of shear was observed. Possible links between the depletion layer and surface slip are discussed. The results show that, in contrast to water, for hexadecane the enhancement of the depletion layer with temperature and interfacial energy reduces the amount of slip. Thus a density depletion cannot be the origin of surface slip in this system. © 2011 American Institute of Physics. [doi:10.1063/1.3549895]

### I. INTRODUCTION

In fluid mechanics, the classical assumption of a flowing liquid featuring a stationary molecular layer adjacent to a solid boundary [no-slip boundary condition (BC)], has been disproved by various experiments with microscopic resolution.<sup>1,2</sup> In order to have a quantitative measure of this effect, the slip length  $b$  is defined as the distance from the solid interface at which the flow profile of the liquid extrapolates to zero,

$$b = \nu(0) \left( \frac{\partial v(z)}{\partial z} \right)^{-1}, \quad (1)$$

where  $\nu$  denotes the velocity of the liquid and  $z$  is the distance from the interface. However, a microscopic picture of surface slip is still missing. Two theoretical scenarios have been proposed. In the case of real slip, the liquid slides over the solid interface on an atomic length scale. This implies either very high shear rates<sup>2</sup> or a roughness of the solid boundary which considerably differs from the size of the liquid molecules.<sup>3</sup> The second, more realistic, scenario for moderate shear over molecularly smooth surfaces is termed “apparent slip.” In this case, a microscopic boundary layer is assumed to exist, which is different structurally and/or dynamically from the bulk liquid. One example of a dynamical near-surface change is the so-called shark-skin effect where, at a critical shear rate, microscopic corrugation of the interface leads to turbulent flow

in the adjacent liquid.<sup>4</sup> This dynamical change appears as a thin layer of different viscosity. Likewise, a structural change of the boundary layer may produce a different viscosity that is observed as surface slip on a larger length scale, although the no-slip BC is still valid microscopically. Nevertheless, to the best of our knowledge, none of these models have been confirmed as the origin of slip in Newtonian liquids on molecularly smooth surfaces.

At present, two models explaining apparent surface slip are under discussion. In the first model, a microscopic layer with depleted liquid density near the solid interface has been proposed.<sup>5</sup> Depletion layers at liquid/solid interfaces have been observed in various cases<sup>6</sup> using x-ray and neutron reflectometry (NR), but only recently they have been recorded under shear load<sup>7</sup> with NR. In the latter study, however, no influence of shear stress on the structure of the depletion layer was observed. The other model proposes an alignment of the near surface molecules with shear stress as the cause of apparent slip.<sup>8</sup> This interpretation is consistent with a greater observed slip length for hexadecane, in which the molecules can be elongated, in comparison with squalane, which is a more symmetric molecule.<sup>9</sup> Surface-induced molecular layering of flowing liquids has been observed in confined propanol<sup>10</sup> using a surface force apparatus (SFA), and in eicosane<sup>11</sup> using an atomic force microscope (AFM) after quenching the flowing alkane. However, these techniques are either indirect or require direct contact with the interfacial liquid and thus may perturb the system.

The present study comprises an extension of an earlier work<sup>7</sup> where we used NR combined with a cone/plate shear

<sup>a)</sup>Electronic mail: gutfreund@ill.eu.

<sup>b)</sup>Electronic mail: max.wolff@fysik.uu.se.

cell to record the liquid density profile perpendicular to the interface while shearing the liquid *in situ*. As a model system, we use hexadecane on differently treated silicon substrates. In the current study, newly commissioned instruments were used, namely the Liquids Reflectometer at the Spallation Neutron Source (SNS) in Oak Ridge, Tennessee, as well as the FIGARO reflectometer at the Institut Laue-Langevin (ILL) in Grenoble, France, enabling us to access a wider  $q$ -range and thus to considerably increase the experimental resolution. Moreover, the use of octadecyl-trichlorosilane (OTS)-covered substrate allows a direct comparison of our structural results with dynamical studies on the same system,<sup>9</sup> building a bridge from depletion to slip.

Slippage of hexadecane has been examined by several techniques yielding slip lengths of 0–110 nm for a wetted interface and slip lengths of 20–350 nm for low interfacial energy substrates (hexadecane contact angle of about 40°).<sup>2,9,12</sup> In spite of the wide variation of reported slip lengths, the qualitative result showing that higher interfacial energy impairs or suppresses slippage of hexadecane is consistent and intuitive. In the present study, we try to establish a connection between the presence of a density depleted liquid layer at the interface and slip. Surprisingly, in our study, the interfacial energy has the opposite influence on the extension of the depletion layer as compared to the slip length. The reduction of the depletion layer with increasing interfacial energy is confirmed by the other studies of static alkanes on solid surfaces.<sup>6</sup> The main result is that the density depletion of liquids at solid boundaries cannot be generally attributed to surface slip.

## II. EXPERIMENTAL DETAILS

In order to measure the reflectivity of the silicon/hexadecane interface while shearing the liquid *in situ*, a shear device with a cone/plate geometry was mounted onto the sample stage of a neutron reflectometer. We used a scattering geometry in which the neutron beam passes through the silicon substrate and is reflected downward from the horizontal solid/liquid interface. The sample geometry is described in more detail elsewhere.<sup>7</sup> Two functionalized single crystalline silicon (100) substrates (70 mm × 70 mm × 10 mm, optically polished, obtained from CrysTec, Germany) were used throughout the experiments. To provide high surface energy, one wafer was chemically cleaned in freshly prepared Piranha solution [50/50 v/v H<sub>2</sub>SO<sub>4</sub>(concentrated) and H<sub>2</sub>O<sub>2</sub>(30% aqueous)] (Oxidizing! Do not mix with organic solvents/materials. Acid-resistant gloves, protective goggles, and lab coats must be worn handling the Piranha solution.) for 30 min and rinsed with Millipore water. Then the substrate was kept in Millipore water (as long as 12 h) up to the drying of the sample with a clean nitrogen stream just before the measurement. As a result, we obtained a surface which was completely wetted by hexadecane, corresponding to an interfacial energy of  $\gamma_{sl} = 34 \text{ mJ/m}^2$  at room temperature.<sup>6,13</sup> For the lower interfacial energy substrate another identically cleaned silicon wafer was subsequently chemically coated with an OTS monolayer by immersing it in a solution of 50 g bicyclohexane, 2.8 g carbon tetrachloride, and 0.8 g OTS for 15 min and flushing

afterward with chloroform to remove any cross-linked OTS chains. This procedure was repeated three times to ensure a fully covered substrate, and the resulting advancing contact angle of hexadecane was  $40^\circ \pm 2^\circ$  at 22°C,  $39^\circ \pm 2^\circ$  at 40°C, and  $37.3^\circ \pm 2^\circ$  at 60°C. This corresponds to an interfacial energy of  $\gamma_{sl} = 7.2 \text{ mJ/m}^2$  at room temperature. The contact angle error corresponds to variations on different spots on the surface. The contact angle hysteresis was always smaller than 2.8°. The OTS substrate was prepared 2 weeks prior to the experiment and was kept in air until the final ultrasonic cleaning in ethanol, acetone, and toluene and drying of the surface with a clean nitrogen gas stream just before the measurement. All relevant surface parameters of this study and our previous article are summarized in Table I.

The NR measurements with the OTS substrate in contact with fully deuterated hexadecane (deuteration > 98.4%, purity 98.9% from Polymer Source, Montreal, Canada) were performed on the Liquids Reflectometer at the SNS. A wavelength band of 2.5–5.5 Å was chosen with a resolution of  $\Delta\lambda/\lambda = 0.5\%$ . Seven incident beam angles ( $\theta = 0.15^\circ, 0.25^\circ, 0.4^\circ, 0.7^\circ, 1.2^\circ, 2.2^\circ$ , and  $3.0^\circ$  for liquid/solid measurements and  $\theta = 0.15^\circ, 0.25^\circ, 0.45^\circ, 0.85^\circ, 1.6^\circ, 3.0^\circ$ , and  $5.5^\circ$  for air/solid measurements) were used to cover a  $q$ -range up to  $0.25 \text{ \AA}^{-1}$  for the liquid/solid interface and  $0.48 \text{ \AA}^{-1}$  in the case of air/solid measurements with a constant angular resolution of 4.4%. A complete reflectivity curve was obtained in 2 h. After background subtraction, the raw data were normalized to a direct beam pattern recorded on the same day and divided by a constant factor for the corresponding slit size. Measurements with fluctuating neutron flux due to spallation source instabilities were discarded.

The NR curves of the cleaned Si wafer in contact with 44% deuterated hexadecane (diluted with protonated hexadecane from BDH Prolabo) were recorded on the FIGARO reflectometer at the ILL. Wavelengths from 2 to 22 Å were used with  $\Delta\lambda/\lambda = 5.6\%$  resolution, while the angular resolution varied for the three incident angles ( $\theta = 0.6^\circ, 2.0^\circ$ , and  $3.8^\circ$ ) between 1% and 2%. The background corrected raw data were normalized to the direct beam pattern measured for each slit setting.

Characterization of the OTS substrate by means of x-ray reflectometry was done on a Panalytical X'Pert Pro laboratory reflectometer. The substrate structure was determined by simultaneously fitting the x-ray and neutron reflectivities of the bare substrate in air, as well as the neutron

TABLE I. Interface properties at room temperature of the surfaces used in this study and in Ref. 7. The interfacial energy  $\gamma_{sl}$  was calculated by using  $\gamma_{sl} = \gamma_{sg} - \gamma_g \cos \theta$ , where  $\gamma_g$  is the surface tension of hexadecane ( $27.1 \text{ mJ/m}^2$ ),  $\gamma_{sg}$  the free surface energy (Ref. 13) and  $\theta$  the contact angle of hexadecane.

Sample	$\gamma_{sg}$ (mJ/m <sup>2</sup> )	$\theta$	$\gamma_{sl}$ (mJ/m <sup>2</sup> )
OTS	28	40°	7.2
HMDS	44	30°	20
Native Si	61	10°	34
UV/ozone treated Si	61	0°	34
Piranha treated Si	61	0°	34

data of the static OTS/*d*-hexadecane interface at 22 °C. The resulting substrate parameters were subsequently fixed and only a change of the liquid density due to temperature was allowed. Fitting of the reflectivity data was accomplished using corefinement of a slab model with Motofit.<sup>14</sup> The depletion layer at the substrate/*d*-hexadecane interface was modeled using an additional layer with reduced liquid density. Due to poor statistics in the reflectivity tail, negative numbers may appear after the background deduction. In order to take into account omitted negative numbers when fitting on a logarithmic scale, a constant background was included in the fits, even though the physical background has already been subtracted in the data reduction process. The given errors correspond to an impairment of the standard deviation ( $\chi^2$ ) by 5%, unless otherwise stated. For the determination of the contact angles, a DataPhysics OCA15EC was used.

### III. RESULTS

#### A. Low interfacial energy surface

The OTS substrate was measured with x-ray and neutron reflectometry before and after the shear experiments, and no change was observed, apart from a slightly increased roughness of the OTS up to 5 Å; however, this roughness increase was not observed in contact with hexadecane. The resulting fitting parameters of the bare substrates are summarized in Table II. Note that the fitted roughnesses are on the same length scale as the thicknesses, especially in case of the silicon oxide layers, which makes it impossible to consider adjacent layers as independent from each other. Thus the corresponding densities and layer thicknesses have to be considered as effective parameters. The reflectivity curves themselves as well as the reflectivity curve for the static *d*-hexadecane/OTS interface at room temperature are shown in Fig. 1. A three slab model for the OTS substrate, consisting of a low and a high density hydrocarbon part and the silicon oxide layer was sufficient to obtain a consistent fit for the x-ray and neutron data simultaneously. This approach has already been

TABLE II. Fitting parameters of the bare substrates before the shear experiment measured with X-ray and neutron reflectometry. SiO<sub>2</sub> denotes the natural silicon oxide layer.  $d$ ,  $\rho$ , and  $\sigma$  correspond to the thickness, scattering length density (SLD) for neutrons, and roughness (error function) of the respective layers. Note that the lower SLD for the low density OTS part comes from the hydrogen termination of the OTS tail. The given errors correspond to one standard deviation.

Parameter	Piranha	OTS
$\sigma_{\text{Si/SiO}_2}$ [Å]	$1.6 \pm 0.4$	$3.8 \pm 0.18$
$d_{\text{SiO}_2}$ [Å]	$8.24 \pm 0.08$	$13.1 \pm 0.18$
$\rho_{\text{SiO}_2}$ [ $10^{-6} \text{Å}^{-2}$ ]	$3.26 \pm 0.01$	$3.42 \pm 0.01$
$\sigma_{\text{SiO}_2/\text{air}}$ [Å]	$2 \pm 0.3$	
$\sigma_{\text{SiO}_2/\text{crystOTS}}$ [Å]		$4.78 \pm 0.03$
$d_{\text{crystOTS}}$ [Å]		$19.9 \pm 0.2$
$\rho_{\text{crystOTS}}$ [ $10^{-6} \text{Å}^{-2}$ ]		$-0.32 \pm 0.001$
$\sigma_{\text{crystOTS}/\text{amorphOTS}}$ [Å]		$0.43 \pm 0.43$
$d_{\text{amorphOTS}}$ [Å]		$5.3 \pm 0.2$
$\rho_{\text{amorphOTS}}$ [ $10^{-6} \text{Å}^{-2}$ ]		$-0.626 \pm 0.002$
$\sigma_{\text{amorphOTS}/\text{air}}$ [Å]		$2.88 \pm 0.02$

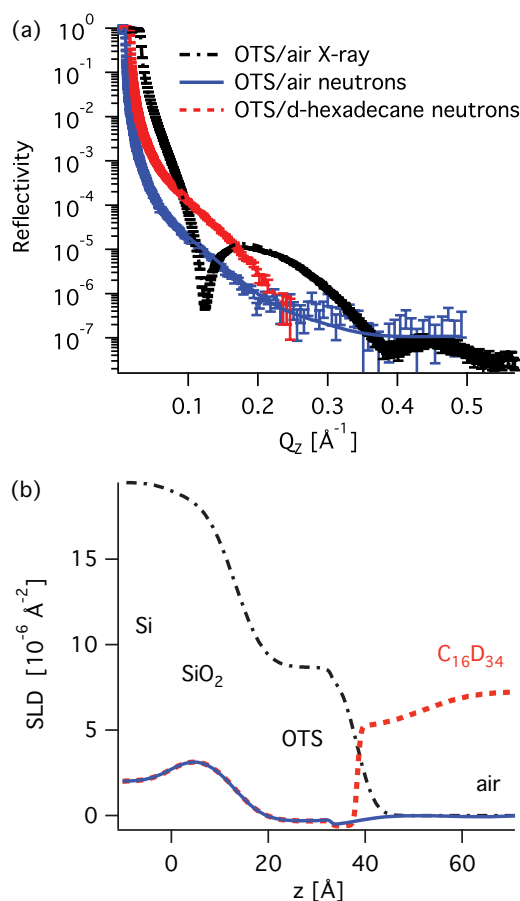


FIG. 1. (a) Neutron (blue bars) and x-ray (black bars) reflectivity curves on a logarithmic scale of the bare silicon wafer covered with OTS; NR for the same substrate in contact with static *d*-hexadecane at 22 °C (red bars). The solid, dotted and dashed lines represent the best fits, respectively. (b) The corresponding SLD profiles obtained with the fits. The color code corresponds to the one used in (a).

successfully used in Ref. 15. In our case, the high density OTS part was  $19.9 \pm 0.2$  Å thick, which corresponds to 14 fully stretched hydrocarbon monomers,<sup>16</sup> with a density of  $0.895 \pm 0.002$  g/cm<sup>3</sup>, close to the density of crystalline octadecane ( $0.93$  g/cm<sup>3</sup>).<sup>17</sup> The low density layer had a thickness of  $5.3 \pm 0.2$  Å corresponding to four hydrocarbon monomers and a density of  $0.888 \pm 0.003$  g/cm<sup>3</sup>. The minor density difference between the two OTS parts was clearly visible by using neutrons due to the hydrogen termination of the OTS tail, which can be easily resolved in deuterated hexadecane due to the negative coherent scattering length density (SLD) of the protons in natural hydrogen. This model resulted in a  $\chi^2$  of 4.175 when fitting the three contrasts simultaneously. The assumption of an OTS head group between the OTS tail and the silicon oxide, as proposed in Ref. 16 and later used in Refs. 18 and 19, leads to a considerably worse fit with a  $\chi^2$  of 4.659. However, the overall OTS thickness of 25.2 Å in our model is comparable to the values reported in the latter studies.

A possible swelling or increased density of the OTS in contact with hexadecane was modeled as well, but this did not improve the fit quality, even though the number of free

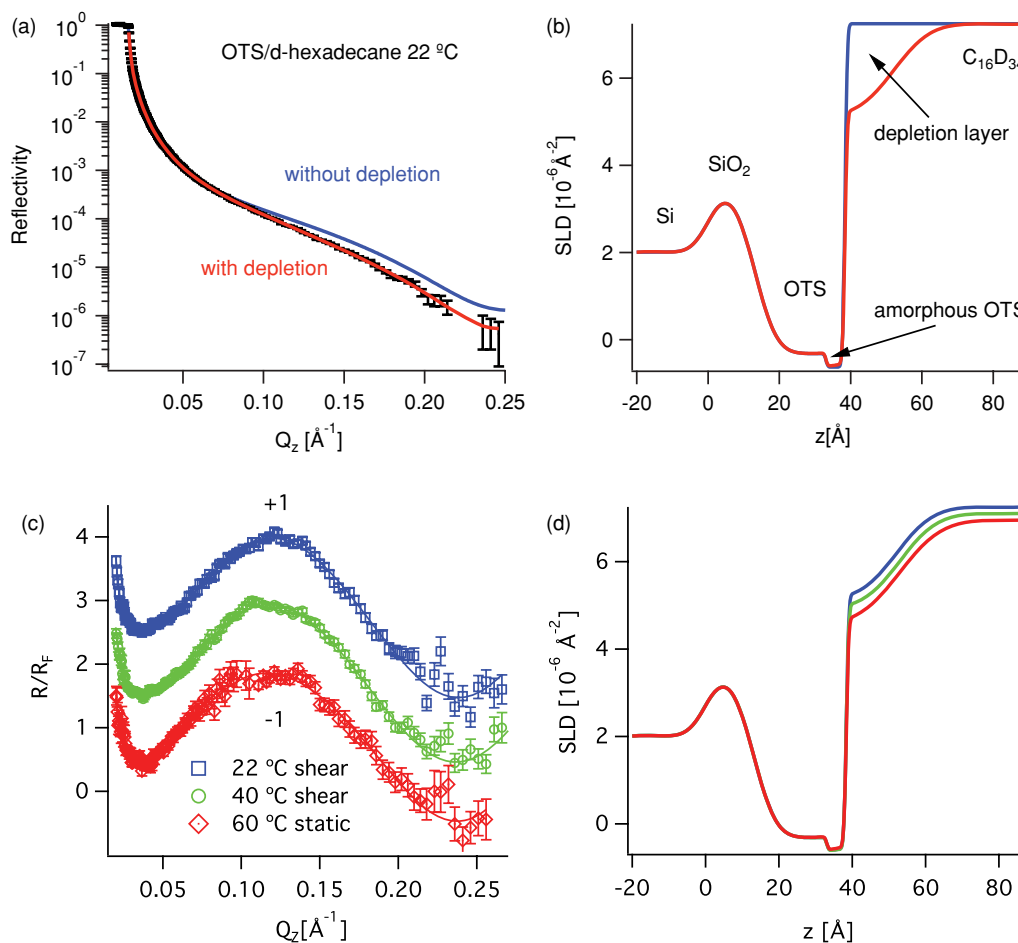


FIG. 2. (a) Logarithmic neutron reflectivity curves from the OTS wafer in *d*-hexadecane (black bars) with the conformable fit (red line). The blue line is a simulation of the reflectivity without depletion. (b) Corresponding SLD profiles. (c) Fresnel normalized neutron reflectivity curves for the OTS/*d*-hexadecane interface at different temperatures. The 22 °C (blue squares) and 60 °C (red diamonds) curves are shifted by one for clarity. (d) The corresponding SLD profiles.

parameters increased. The only change of the substrate structure in contact with the liquid was the OTS roughness which decreased from 2.88 to 0.5 Å. According to the fit, swelling of the OTS layer with increasing temperature did not occur either. Thus, in the following, the bare substrate parameters were kept constant during the fitting.

As one can derive from Fig. 2(b), a 14 Å thick hexadecane layer with a density depletion of 30% must be introduced to fit the data with a standard deviation of 1.4. If no depletion layer is assumed, the best alternative fit has to assume swelling of the OTS layer and leads to a  $\chi^2$  of 4.1 [see Fig. 2(a)]. This impairment of the fit quality is much larger than 5% and obviously does not fit the measured reflectivity. Thus, this possibility was excluded. All other parameters determined from the bare substrate fit were kept constant in fitting the hexadecane data. In order to compare the resulting depletion effects, the depletion distance  $d_2$  (Ref. 20) is introduced,

$$d_2 = \int_{\text{liquid phase}} \left(1 - \frac{\rho(z)}{\rho_{\text{bulk}}}\right) dz, \quad (2)$$

where  $\rho(z)$  denotes the density of the depleted liquid at a distance  $z$  from the interface and  $\rho_{\text{bulk}}$  represents the bulk liquid density.  $d_2$  reduces the smeared-out density profile of the

depletion to a steplike function that represents an equivalent layer of zero density.

The depletion distance calculated in the case of the OTS/hexadecane interface at 22 °C is  $3.8 \pm 0.24$  Å. The subsequent application of shear at  $500 \text{ s}^{-1}$  does not change the depletion distance within the error bars. Increasing the temperature enlarges the depletion distance slightly to  $d_2 = 4.6 \pm 0.45$  Å at 60 °C, as shown in Fig. 3, but no effect of shear is visible.<sup>21</sup>

## B. High interfacial energy surface

Next we discuss the interfacial structure at the wetted surface. In this case, only a model with a considerably stronger SLD depletion of up to 100% and of 16–25 Å thickness fits the data, as seen in Fig. 4. The derived depletion distance is  $20.5 \pm 2.5$  Å. Contrary to the OTS surface, the application of shear at  $500 \text{ s}^{-1}$  changes the reflectivity curve as can be seen in Fig. 4(a). The resulting depletion shrinks slightly to  $16.5 \pm_{0.5}^{0.9}$  Å.

Due to the highly hydrophilic surface, the presence of a thin layer of protonated water cannot be excluded, even though the substrate was dried with a clean nitrogen stream

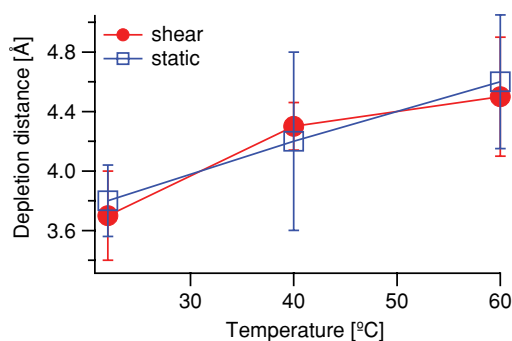


FIG. 3. Depletion distances calculated from the fitted SLD profiles of the OTS/*d*-hexadecane interface.

until no water was optically visible. From SFA studies, it is known that even the low solubility of water in oils can affect the hydrodynamic forces between hydrophilic surfaces on a length scale of several nm when working under a humid atmosphere.<sup>22</sup> The assumption of a 13 Å thick protonated water layer instead of the depletion layer leads to the same fit quality, due to the small SLD difference between protonated water and air. Thus the depletion distances for the chemically cleaned SiO<sub>2</sub> interface have to be understood as an upper limit, as in the previous study.<sup>7</sup>

## IV. DISCUSSION

### A. Low interfacial energy surface

The calculated depletion distances, ranging from 3.4 to 5 Å in the case of the OTS coated surface, are consistent with previously measured values at the interface between octane and self-assembled monolayers (SAM).<sup>6</sup> Note that in the present study the depletion layer can be modeled separately from the SAM due to the high resolution of the instrument, and, therefore, no reference system is needed anymore, which could introduce a systematic error. A further indication of the intrinsic nature of the observed depletion at the OTS/*d*-hexadecane interface is the enhancement of the depletion distance with temperature. The growth of the depletion layer with increasing temperature has already been observed for water in contact with a SAM and predicted by molecular dynamics (MD) simulations.<sup>6</sup> A possible contamination of the OTS layer due to contact with air<sup>23</sup> is unlikely, as dust layers do not show any change with temperature, but increase with time,<sup>6</sup> which was not the case for the depletion at OTS, even after 2 days. Furthermore, the contamination layer observed in Ref. 23 was only 2 Å thick, much thinner than the depletion layer at OTS, which spans about 14 Å.

Several properties of the OTS layer are crucial for the amount of slip, namely, the surface roughness<sup>24</sup> and the homogeneous surface coverage of the film.<sup>25</sup> Regarding our own experience and findings in the literature,<sup>26</sup> a nonhomogeneously grown or cross-linked OTS film, e.g., due to the presence of too much water during the growth process, shows up as a 12–15 Å thin film with a roughness of more than 5 Å. In our case, the overall OTS thickness was 25.2 Å with a roughness of 2.88 Å. Hence, we infer that

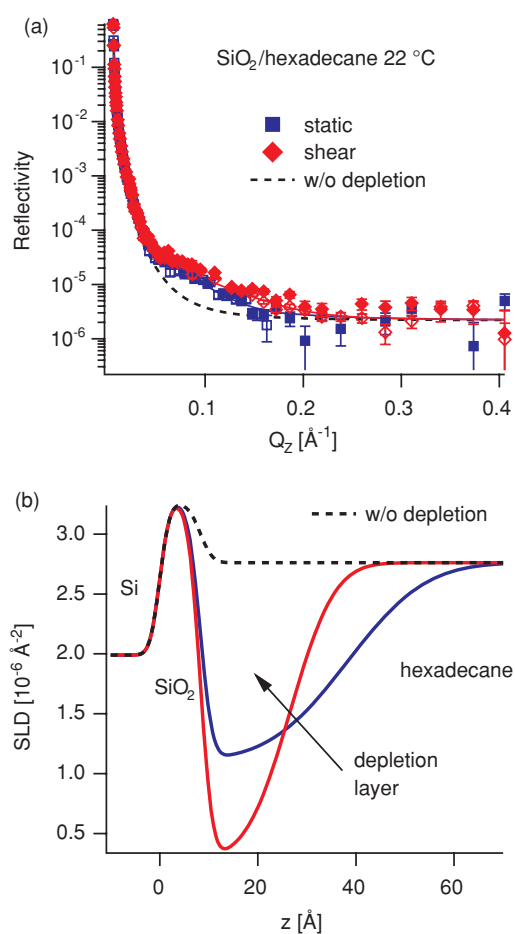


FIG. 4. (a) Logarithmic neutron reflectivity curves from the cleaned Si wafer in contact with 44% deuterated hexadecane at 22 °C. The blue squares correspond to the static case, the red ones to the sheared liquid. Open and closed symbols indicate reproduction measurements. The solid lines are fits, respectively. Additionally, the theoretical reflectivity without any depletion is shown by the dashed line. (b) The SLD profiles corresponding to the fits.

our OTS film is complete and comparable to the ones used in the cited literature. To the best of our knowledge, two research groups have investigated surface slip of hexadecane on silanated surfaces up to now. Fluorescence recovery after photobleaching (FRAP) has been used to measure a slip length of 3500 Å for hexadecane in contact with an OTS layer, which was 24.5 Å thick and 3.5 Å rough and thus directly comparable to ours.<sup>9</sup> In a surface force study of hexadecane on hexadecyltrichlorosilane (HTS), a slip length of 200 Å was observed.<sup>12</sup> In this case the roughness was 3 Å.

As mentioned in the Introduction, viscosity change due to the depleted liquid at the interface may be a possible explanation of surface slip. If one considers this interfacial layer as a density depleted region solely (no change of the liquid structure), it can be related to the slip length  $b$  introduced in Eq. (1).<sup>27</sup> A straightforward calculation yields

$$b = \int_{\text{liquid phase}} \left( \frac{\rho_{\text{bulk}}}{\rho(z)} - 1 \right) dz. \quad (3)$$

The calculated slip length of flowing hexadecane over OTS at 22 °C is  $5.18 \pm 0.15$  Å in our case. This is far too small to explain the reported hexadecane slip lengths mentioned

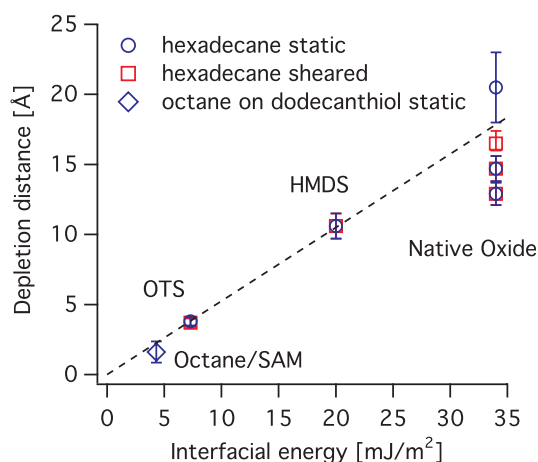


FIG. 5. Depletion distances for hexadecane calculated from the fitted SLD profiles of the liquid/solid interfaces using Eq. (3). The numbers for the HMDS surface, the untreated silicon, and the UV/ozone treated substrate are from Ref. 7. As comparison the depletion distance measured for *d*-octane in contact with a *d*-dodecanthiol SAM from Ref. 6 is included. The dotted line is a guide to the eye.

above. Accordingly, this result argues against the appearance of surface slip by a pure density depletion of the interfacial liquid.

## B. High interfacial energy surface

Concerning the bare silicon substrate, considerably larger depletion distances of about 16–23 Å are indicated by the results. Moreover, this is the first system where we have been able to observe a change in the interfacial structure while applying shear. This shows that even a moderate shear rate of  $500 \text{ s}^{-1}$  can affect the structure of the interfacial liquid featuring a bulk structural relaxation time on the order of ps. This dependence might imply discontinuous dynamics near the interface, e.g., surface slip. Unfortunately, the presence of a thin water layer cannot be excluded, thus these numbers have to be considered as upper limits on the depletion. Nevertheless, the calculated slip length via Eq. (3) lies between 41 and 133 Å. If part or all of the depleted SLD would be due to water the calculated slip length would be even smaller because the viscosity of water is greater than 0 and Eq. (3) assumes slip due to a viscosity reduction at the interface. In any case, this value is too small to explain the 1100 Å slip length measured with FRAP for hexadecane on a mica surface,<sup>9</sup> in spite of the comparable surface roughnesses and surface energies in both studies. On the other hand, SFA based studies report no slip of hexadecane on mica surfaces.<sup>22</sup> Here the liquids were degassed and the measurement was performed under a dry atmosphere. Perhaps this could be the origin of the discrepancy between the reported slip lengths.

## V. CONCLUSION

All our results show the same trend with increasing interfacial energy, namely, an enhancement of the depletion layer. The same effect was observed, when the interfacial structures of different liquids in contact with the same solid were

compared.<sup>6</sup> In Fig. 5 all depletion distances measured in this work as well as in our previous study<sup>7</sup> and in Ref. 6 are plotted versus the interfacial energy  $\gamma_{sl}$ . The obvious connection between the interfacial energy and the extension of the depletion layer is in contrast with the trend of surface slippage of alkanes, which is more pronounced for lower interfacial energy surfaces.<sup>9,12</sup> The enhancement of the depletion layer with temperature is also contrary to the temperature dependent reduction of slip length observed in polystyrene on OTS.<sup>28</sup> Accordingly, the enhancement of the depleted layer contradicts the amount of surface slip. Thus, in addition to slip lengths calculated via formula (3), which are orders of magnitude smaller than the reported literature values, the opposite trend of the depletion effect with interfacial energy we observe shows that the presence of a depletion layer alone cannot explain surface slippage of hexadecane. This result is in sharp contrast to the findings in a recent MD simulation study<sup>29</sup> of water on a diamond surface, where the calculated slip length increased for thicker depletion layers. This result shows that interfacial liquid structure has different effects on the boundary conditions of flowing liquids, dependent on the type of liquid used, and that the depletion layer cannot be generally attributed to surface slip. Therefore, structural investigations via surface sensitive diffraction techniques are necessary.

## VI. SUMMARY

In summary, we have studied the interface of flowing hexadecane at functionalized solid boundaries by neutron reflectivity. For both high- and low-energy interfaces a layer with depleted liquid density at the hexadecane/solid interface is indicated by the results. But these depletion effects cannot explain reported slip lengths in similar systems if only a density depleted layer is assumed. The opposing influences of interfacial energy and temperature on depletion, as compared to surface slip, point out that the appearance of a depletion layer even contradicts slippage of hexadecane. Thus, different structural rearrangements, e.g., molecular alignments, are more likely to mediate surface slip as proposed in Refs. 8 and 9. Such surface-induced order under shear stress has already been observed in the case of micelles<sup>30,31</sup> using neutron scattering and indirectly in confined propanol<sup>10</sup> and eicosane<sup>11</sup> using SFA and AFM based techniques, as well as in MD simulations<sup>32</sup> and theoretical calculations<sup>33</sup> of confined liquids.

## ACKNOWLEDGMENTS

We thank R. Campbell for the help with the experiment on FIGARO and we gratefully acknowledge financial support by the BMBF (05K10PC1) and the DFG Grant No. ZA161/18 within the priority program (SPP) 1164. The measurements at SNS were carried out by the U.S. DOE under Contract No. DE-AC05-00OR22725.

<sup>1</sup>C. Neto, D. Evans, E. Bonaccorso, H. Butt, and V. Craig, *Rep. Prog. Phys.* **68**, 2859 (2005).

<sup>2</sup>E. Lauga, M. P. Brenner, and H. A. Stone, *Microfluidics: The No-Slip Boundary Condition*, edited by J. Foss, C. Tropea, and A. Yarin (Springer, New York, 2007).

- <sup>3</sup>T. Galea and P. Attard, *Langmuir* **20**, 3477 (2004).
- <sup>4</sup>D. Bushnell and K. Moore, *Annu. Rev. Fluid Mech.* **23**, 65 (1991).
- <sup>5</sup>D. C. Tretheway and C. D. Meinhart, *Phys. Fluids* **16**, 1509 (2004).
- <sup>6</sup>M. Maccarini, R. Steitz, M. Himmelhaus, J. Fick, S. Tatur, M. Wolff, M. Grunze, J. Janecek, and R. R. Netz, *Langmuir* **23**, 598 (2007).
- <sup>7</sup>M. Wolff, B. Akgun, M. Walz, A. Magerl, and H. Zabel, *Europhys. Lett.* **82**, 1 (2008).
- <sup>8</sup>J. Barrat and L. Bocquet, *Faraday Discuss.* **112**, 119 (1999).
- <sup>9</sup>T. Schmatko, H. Hervet, and L. Leger, *Phys. Rev. Lett.* **94**, 980 (2005).
- <sup>10</sup>G. Sun, E. Bonaccorso, V. Franz, and H. Butt, *J. Chem. Phys.* **117**, 10311 (2002).
- <sup>11</sup>C. Drummond, N. Alcantar, and J. Israelachvili, *Phys. Rev. E* **66**, 1 (2002).
- <sup>12</sup>J. Cho, B. Law, and F. Rieutord, *Phys. Rev. Lett.* **92**, 166102 (2004).
- <sup>13</sup>S. Lim, S. Kim, J. Lee, M. Kim, D. Kim, and T. Zyung, *Synth. Met.* **148**, 75 (2005).
- <sup>14</sup>A. Nelson, *J. Appl. Crystallogr.* **39**, 273 (2006).
- <sup>15</sup>G. Fragneto, R. Thomas, A. Rennie, and J. Penfold, *Science* **267**, 657 (1995).
- <sup>16</sup>I. M. Tidswell, B. M. Ocko, P. S. Pershan, S. R. Wasserman, G. M. Whitesides, and J. D. Axe, *Phys. Rev. B* **41**, 1111 (1990).
- <sup>17</sup>X. Wu, E. Sirota, S. Sinha, B. Ocko, and M. Deutsch, *Phys. Rev. Lett.* **70**, 958 (1993).
- <sup>18</sup>M. Mezger, H. Reichert, S. Schoeder, J. Okasinski, H. Schroeder, H. Dosch, D. Palms, J. Ralston, and V. Honkimaki, *Proc. Natl. Acad. Sci. U.S.A.* **103**, 18401 (2006).
- <sup>19</sup>M. Mezger, S. Schoeder, H. Reichert, H. Schroeder, J. Okasinski, V. Honkimaki, J. Ralston, J. Bilgram, R. Roth, and H. Dosch, *J. Chem. Phys.* **128**, 244705 (2008).
- <sup>20</sup>S. Mamatkulov, P. Khabibullaev, and R. Netz, *Langmuir* **20**, 4756 (2004).
- <sup>21</sup>See supplementary material at <http://dx.doi.org/10.1063/1.3549895> for additional reflectivity curves, remaining fitting parameters, and the resulting depletion distances.
- <sup>22</sup>D. Chan and R. Horn, *J. Chem. Phys.* **83**, 5311 (1985).
- <sup>23</sup>Y.-S. Seo and S. Satija, *Langmuir* **22**, 7113 (2006).
- <sup>24</sup>T. Schmatko, H. Hervet, and L. Leger, *Langmuir* **22**, 6843 (2006).
- <sup>25</sup>R. Pit, H. Hervet, and L. Leger, *Phys. Rev. Lett.* **85**, 980 (2000).
- <sup>26</sup>Y. Wang and M. Lieberman, *Langmuir* **19**, 1159 (2003).
- <sup>27</sup>O. I. Vinogradova, *Langmuir* **11**, 2213 (1995).
- <sup>28</sup>R. Fetzer, M. Rauscher, A. Muench, B. A. Wagner, and K. Jacobs, *Europhys. Lett.* **75**, 638 (2006).
- <sup>29</sup>D. M. Huang, C. Sendner, D. Horinek, R. R. Netz, and L. Bocquet, *Phys. Rev. Lett.* **101**, 226101 (2008).
- <sup>30</sup>W. Hamilton, L. Porcar, and L. Magid, *Physica B* **357**, 88 (2005).
- <sup>31</sup>M. Wolff, R. Steitz, P. Gutfreund, N. Voss, S. Gerth, M. Walz, A. Magerl, and H. Zabel, *Langmuir* **24**, 11331 (2008).
- <sup>32</sup>N. Priezjev, A. Darhuber, and S. Troian, *Phys. Rev. E* **71**, 041608 (2005).
- <sup>33</sup>S. Heidenreich, P. Ilg, and S. Hess, *Phys. Rev. E* **75**, 066302 (2007).

## Supplementary to Depletion at sheared Liquid-Solid Interfaces

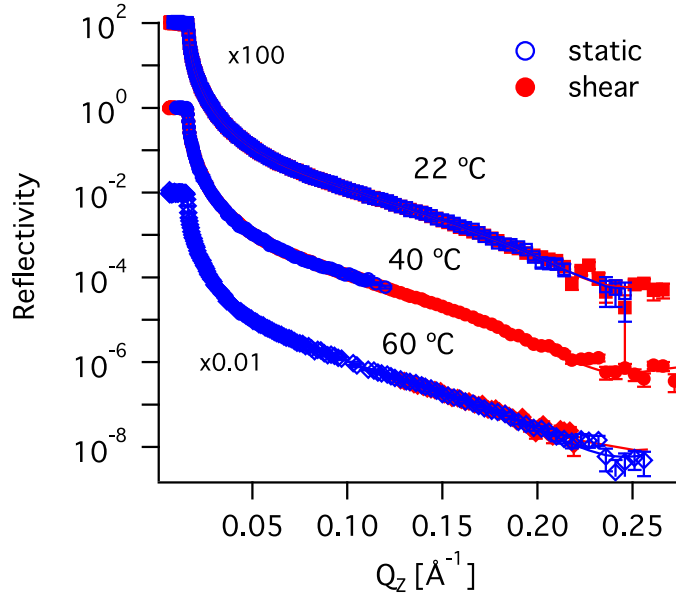


Figure 6. Reflectivity curves on a logarithmic scale for all temperatures and shear rates of the d-hexadecane/OTS interface. Open symbols correspond to the static and filled symbols to the sheared liquid. Reflectivities for different temperatures are shifted for clarity.

OTS	22 C		40 C		60 C		SiO <sub>2</sub>	22 C
	static	sheared	static	sheared	static	sheared		
$\rho_{hd}$ [ $10^{-6} \text{Å}^{-2}$ ]	$7.25 \pm 0.1$	$7.25 \pm 0.1$	$7.1 \pm 0.1$	$7.1 \pm 0.1$	$6.95 \pm 0.1$	$6.95 \pm 0.1$	$2.76 \pm 0.1$	$2.76 \pm 0.1$
$\sigma_{hd/depl}$ [ $\text{Å}$ ]	$6.3 \pm 2.7$	$8 \pm 1.1$	$7.5 \pm 6.9$	$9.8 \pm 0.2$	$9 \pm 1.2$	$6 \pm 10$	$13 \pm 1.8$	$7.4 \pm 0.5$
$d_{depl}$ [ $\text{Å}$ ]	$16 \pm 2.3$	$13.7 \pm 1.6$	$17.5 \pm 6.4$	$11 \pm 0.7$	$14.6 \pm 1.8$	$14 \pm 9.8$	$19 \pm 1.2$	$16.5 \pm 1.3$
$\rho_{depl}$ [ $10^{-6} \text{Å}^{-2}$ ]	$5.5 \pm 0.4$	$5.1 \pm 0.3$	$5.4 \pm 0.95$	$4.3 \pm 0.1$	$4.6 \pm 0.3$	$5.1 \pm 1.9$	$0 \pm 0.2$	$0 \pm 0.2$
$d_2$ [ $\text{Å}$ ]	$3.8 \pm 0.24$	$3.7 \pm 0.3$	$4.2 \pm 0.6$	$4.3 \pm 0.16$	$4.6 \pm 0.45$	$4.5 \pm 0.4$	$20.5 \pm 2.5$	$16.5 \pm_{0.3}^{0.9}$

Table III. Fitting parameters and calculated depletion distances  $d_2$  via equation 2.  $\rho_{hd}$  corresponds to the SLD of the bulk hexadecane,  $\sigma_{hd/depl}$  to the interface roughness between the bulk and the depleted liquid and  $d_{depl}$  is the thickness of the depleted layer with the SLD  $\rho_{depl}$ . Note that the fitting parameters are correlated and only the resulting depletion distance can be assumed as an independent parameter.



# B. Surface Correlation Affects Liquid Order and Slip in a Newtonian Liquid

*submitted to Physical Review Letters*

Authors: P. GUTFREUND<sup>1,2</sup>, O. BÄUMCHEN<sup>3</sup>, D. VAN DER GRINTEN<sup>1</sup>, R. FETZER<sup>3</sup>, M. MACCARINI<sup>2</sup>, K. JACOBS<sup>3</sup>, H. ZABEL<sup>1</sup>, M. WOLFF<sup>4</sup>

<sup>1</sup>Ruhr-Universität Bochum, 44780 Bochum, Germany

<sup>2</sup>Institut Laue-Langevin, BP 156, 38042 Grenoble, France

<sup>3</sup>Department of Experimental Physics, Saarland University, 66041 Saarbrücken, Germany

<sup>4</sup>Material Science, Department of Physics, Uppsala University, 75121 Uppsala, Sweden

*Author contributions: M. Wolff and K. Jacobs designed research. The samples were prepared by O. Bäumchen and R. Fetzer. The experiments were performed by M. Wolff, D. van der Grinten and P. Gutfreund. Data analysis was performed by P. Gutfreund. The article was written by P. Gutfreund under the supervision of M. Wolff, M. Maccarini, O. Bäumchen, R. Fetzer, K. Jacobs and H. Zabel.*

# Surface Correlation Affects Liquid Order and Slip in a Newtonian Liquid

Philipp Gutfreund<sup>1,2,\*</sup>, Oliver Bäumchen<sup>3,†</sup>, Dorothee van der Grinten<sup>1</sup>, Renate Fetzner<sup>3,‡</sup>, Marco Maccarini<sup>2</sup>, Karin Jacobs<sup>3</sup>, Hartmut Zabel<sup>1</sup>, and Max Wolff<sup>4</sup>

<sup>1</sup>*Condensed Matter Physics, Ruhr-University Bochum, 44780 Bochum, Germany*

<sup>2</sup>*Institut Laue-Langevin, 38042 Grenoble, France*

<sup>3</sup>*Department of Experimental Physics, Saarland University, 66041 Saarbrücken, Germany*

<sup>4</sup>*Materials Science, Department of Physics and Astronomy, Uppsala University, 75121 Uppsala, Sweden*

(Dated: April 5, 2011)

Interfacial slip can enhance fluid flow substantially. Polystyrene (PS) melts show a large difference in slip velocity on top of dodecyl- (DTS) and octadecyl-trichlorosilane (OTS). To study the microscopic origin of this macroscopic effect, we performed x-ray and neutron reflectivity studies characterizing the PS/silane interfaces. The results reveal the molecular conformation of PS at the two silane layers. Differences in the surface order of OTS and DTS are replicated by the adjacent PS. Our findings open a link between the microscopic interfacial structure and liquid slip.

When downsizing devices, confinement and interface effects grow enormously in importance. Especially, in the context of microfluidic devices [1], the controlled motion of small amounts of liquid is indispensable. These systems open completely new perspectives for research as well as for applications, like e.g. lab-on-chip devices in pharmaceuticals, chemistry or the food industry. Likewise, polymer flow in confined geometries plays an important role in nanodevice fabrication [2]. As the solid/liquid friction dramatically impacts hydrodynamics in these systems, the boundary condition (BC) of flowing liquids, commonly quantified by the slip length [3], has been extensively revised on a microscopic length scale in recent years [4]. Although interfacial slip developed to a well-recognized phenomenon, its microscopic origin is still unclear. It is the aim of this Letter to shed light on the matter.

From a theoretical point of view, two different types of slippage are distinguished [5]: *Real slip* occurs when the liquid slides over the solid surface on an atomic scale. Alternatively, *apparent slip* arises where a microscopic boundary layer is assumed to exist that is structurally and/or dynamically different from the bulk liquid. This boundary layer may lead to a different viscosity and is observed as interfacial slip on a larger length scale, although the no-slip BC may microscopically still hold. The nature of such a boundary layer may be depleted density of the liquid [6] or an alignment of the near-surface molecules [7].

Depletion effects of simple liquids have been observed in various cases [8–11] using x-ray and neutron reflectometry (XRR and NR). Their origin and the consequential link to macroscopic properties of liquids on solid surfaces such as hydrophobicity and also slippage is currently under debate [10–12]. Density profile fluctuations and depletion layers of polymer melts close to solid substrates were also reported and attributed to altered molecular conformations and locally modified segmental distributions [13]. In cases of entangled polymer melts, dedicated chain conformations at the solid/liquid interface

are responsible for a decrease in the entanglement density compared to the bulk and, thus, substantially influence slippage [14].

In this Letter, we present a combined XRR and NR study on polystyrene (PS) films on top of two different silanes, octadecyl-trichlorosilane (OTS) and dodecyl-trichlorosilane (DTS). As known from previous studies, PS melts show large slippage when flowing over hydrophobized surfaces, depending on molecular weight [14], temperature and substrate [15]. In contact with OTS the slip length is about one order of magnitude smaller than for DTS covered silicon (Si). This strong effect on slip length is surprising, as both are chemically identical self-assembled monolayers (SAM) that differ only by six backbone hydrocarbons in tail length. We show that the difference between the two surfaces is a less pronounced in-plane order of the DTS. We provide evidence that the SAMs induce a conformational change within the interfacial polymer, which influences slippage.

The Si wafers (Wacker/Siltronic, Burghausen, Germany) were hydrophobized with OTS and DTS monolayers [16], which resulted in a static contact angle of  $67 \pm 3^\circ$  for PS on the silanized wafers in both cases. The atactic PS with a molecular weight of 13.7 kg/mol ( $M_w/M_n=1.03$ ) and the deuterated PS (*d*PS) with a molecular weight of 12.3 kg/mol ( $M_w/M_n=1.05$ ) were purchased from PSS, Mainz, Germany. PS films between 50 nm and 60 nm were prepared by spin-casting a toluene solution (Merck, Darmstadt, Germany) onto mica, floating on Millipore water, from where they were picked up by the hydrophobized wafers. Then, the samples were annealed above the glass transition temperature ( $T_g$ ) at 120 °C for 30 s. Further details and slip length determination can be found elsewhere [15].

The x-ray measurements were conducted at beamline BL9 [17] of the Dortmund Electron Accelerator (DELTA), Germany, with photon energies of 11 keV and 15.2 keV and beam sizes of  $0.2 \times 2.5$  mm<sup>2</sup> and  $0.1 \times 1$  mm<sup>2</sup>, respectively, with an angular resolution of  $0.008^\circ$  (FWHM). During the x-ray measurements, we ob-

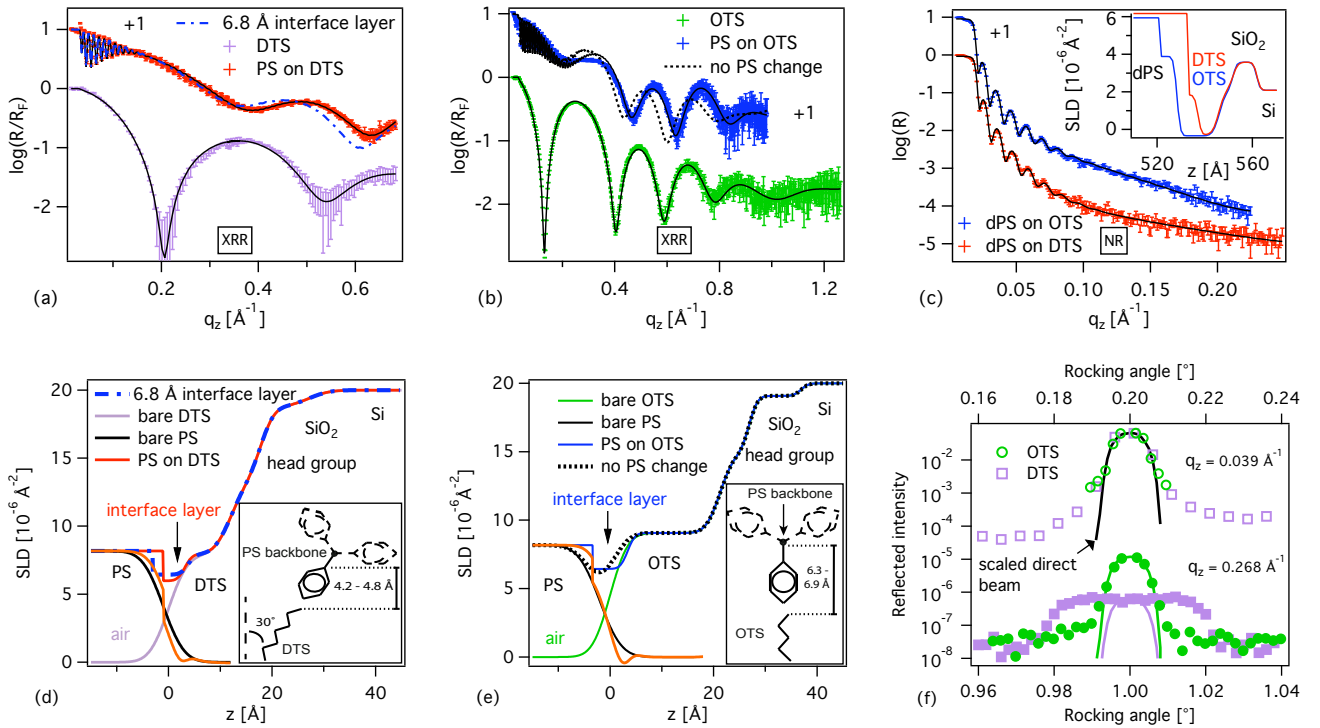


Figure 1. X-ray reflectivity curves divided by the Fresnel-reflectivity on a logarithmic scale of the bare silicon wafers covered with DTS (purple bars) (a) and OTS (green bars) (b) as well as the reflectivities for the samples covered with PS (shifted by one, red and blue bars, respectively). The solid lines represent fits. Fig. (d) and (e) display the corresponding scattering length density (SLD) profiles in the same color code. The dotted lines are explained in the text. Fig. (c) shows neutron reflectivities in log scale of the OTS (blue bars, shifted by one) and DTS (red bars) substrates covered with deuterated PS films. The solid lines are fits corresponding to the SLD profile from the inset in the same color code. In Fig. (f), rocking scans of the bare DTS (squares) and OTS (circles) covered substrates are plotted for two values of  $q_z$  on a logarithmic scale. The solid lines show the direct beam scaled with the specular reflectivity for the given  $q_z$ .

served no beam damage. The NR measurements were performed on the ADAM Reflectometer [18] at the Institut Laue-Langevin (ILL) in Grenoble, France, using a  $0.5 \times 10 \text{ mm}^2$  beam with a constant angular resolution of  $0.08^\circ$  (FWHM). Pre-characterization of the samples dedicated for neutron scattering by means of XRR was done on the laboratory reflectometer XPert Pro PW3020, Panalytical, Netherlands. Fitting of the reflectivity data was obtained by using co-refinement of a slab model with *Motofit* [19, 20].

The x-ray reflectivities normalized to the Fresnel curve, i.e. the reflectivity for an ideally flat silicon surface, are shown in Fig. 1(a) and (b). To get a quantitative description of the measured results, we first analyze the silanized Si wafers and assume a three-slab model, consisting of silicon oxide ( $\text{SiO}_2$ ), a silane headgroup and a hydrocarbon tail [21]. This reproduces the measured data, as can be seen by the solid lines in Fig. 1. The SAM parameters reflect the characteristics of homogeneously grown silane layers [21]. On top of the 9 - 10 Å thick  $\text{SiO}_2$ , with densities of  $2.24 - 2.25 \text{ g/cm}^3$ , there is a silane headgroup, which is 5.6 - 5.95 Å thick, followed by

the silane tail. The roughness between subsequent layers is between 1 - 4 Å. Note that the roughness of the bare DTS tail of  $2.9 \pm 0.08 \text{ Å}$  is comparable to the  $2.73 \pm 0.01 \text{ Å}$  measured for OTS. This rules out the influence of surface roughness on the slippage difference. The only significant difference between the DTS and the OTS layer, apart from the tail length, is a slightly higher grafting density of the OTS, which appears as a higher electron density of the silane head and tail. The headgroup of the DTS has an electron density of  $0.476 \pm 0.007 \text{ Å}^{-3}$ , compared to  $0.532 \pm 0.004 \text{ Å}^{-3}$  in case of the OTS. Likewise, the density of the DTS tail ( $0.82 \pm 0.01 \text{ g/cm}^3$ ) corresponds to 88% of an alkane crystal's density [22], whereas the OTS reaches 100% ( $0.936 \pm 0.004 \text{ g/cm}^3$ ). This difference is also observed when comparing the thicknesses of the layers with the calculated length of an all-trans hydrocarbon chain [21]. The  $21.31 \pm 0.05 \text{ Å}$  OTS tail length matches 99% of the calculated fully stretched molecule (21.5 Å). The  $12.0 \pm 0.1 \text{ Å}$  DTS tail length, however, corresponds to only 86% of the calculated 13.9 Å, which is commonly explained as a tilted SAM [21] and yields a tilt angle of  $30^\circ$  for DTS.

To check the lateral surface correlation of the two layers, we performed rocking scans on the bare silanized substrates. The rocking peaks at two positions on the reflectivity curves are displayed in Fig. 1(f). For the small  $q_z$  value, which is close to the total reflection edge ( $q_c = 0.03 \text{ \AA}^{-1}$ ), the peaks of DTS and OTS do not differ and reflect the experimental resolution. At the higher  $q_z$  value, however, the DTS peak is considerably broadened as compared to the resolution, which is not observed at the OTS for the same in-plane momentum transfers. This indicates a better height-height correlation of the OTS surface compared to the DTS, which corroborates the assumption of upright-standing OTS as compared to tilted DTS tails exhibiting a less pronounced long-range order.

When the silanized substrates are brought into contact with PS and annealed above  $T_g$ , the data analysis reveals an interface layer with lower density between the SAM tail and the PS. To check whether this density-reduced layer is just an artifact of the roughness of the adjacent layers, we simulated the electron density profile of the interface between the OTS and PS layers, assuming no change in the layers themselves. The simulated scattering length density (SLD) profile and the resulting reflectivity are denoted by black dotted lines in Fig. 1(b) and (e). This assumption does not reproduce the measured curve, obviously the PS has changed in contact with the SAM. The resultant electron density profile of the PS (orange curve) can be obtained by subtracting the bare silanized substrate profile (green and purple line) from the fitted SLD of the PS/SAM interface (red and blue line). It shows pronounced features and deviates from the smooth density profile of the bare PS (black curve). The sharp density change of the interface layer towards the residual PS film points out that a smooth interface has emerged on a molecular level. The major difference between the DTS and OTS interfaces is the thickness of the density-reduced interface layer. The  $4.2 \pm 0.14 \text{ \AA}$  thick layer at the PS/DTS interface is considerably thinner than the  $6.79 \pm 0.04 \text{ \AA}$  at the PS/OTS.

In order to get information about the chemical composition of this layer, we have performed NR experiments on the same system. In contrast to x-rays, which are sensitive to the electron density of the sample, neutrons are scattered by nuclei and the scattering length difference between a proton ( $-3.7 \text{ fm}$ ) and a deuteron ( $6.7 \text{ fm}$ ) is noticeable. This makes NR particularly sensitive to protonated/deuterated interfaces. Replacing the PS by *d*PS, we obtained the NRs shown in Fig. 1(c). By combining the neutron and x-ray SLDs, the chemical composition of the density-reduced layer can be calculated. For the OTS interface, this results in  $66 \pm 4 \%$  PS and  $11 \pm 3 \%$  silane as compared to the bulk density, and, in case of the DTS,  $32 \pm 12 \%$  PS and  $43 \pm 12 \%$  silane are present. This means that the observed low-density layer comprises parts of the SAM and the PS as assumed in recent x-ray

reflectometry studies of water at hydrophobic surfaces [9, 10].

To produce the sharp density step of PS in contact with the SAMs (orange curves in Fig. 1(d),(e)), the adjacent PS chains cannot be randomly oriented. Instead, a rather well-ordered arrangement of contacting chain segments is formed. Considering the molecular composition of PS, only an orientation with the phenyl groups pointing to the SAM can comply all parameters extracted from the scattering experiments. The distance between the hydrocarbon backbone of the PS and the end of the phenyl group, including the covalent radius of the hydrogen, is  $5.6 \text{ \AA}$ . The projected bonding length of the OTS hydrogen termination including its covalent radius is  $0.65 - 1.25 \text{ \AA}$ , depending on whether the covalent radius of the linked carbon is subtracted or not. In total this adds up to  $6.25 - 6.85 \text{ \AA}$ , in accordance with the  $6.8 \text{ \AA}$  thick interface layer observed at the PS/OTS interface (see Fig. 1(e) inset). Due to three possible orientations of the phenyl group around a flat PS backbone, in average only every third one would be incorporated in the interface layer. In the bulk, one and a half out of three phenyl rings are projected on one side of the PS backbone. This explains the density of deuterated material, reduced by one third, in the interface layer revealed by NR. If we additionally assume that the phenyl rings follow the orientation of the SAM, they would be tilted by  $30^\circ$  as depicted in the inset of Fig. 1(d) in contact with DTS. This would lead to a reduced interface layer of  $4.18 - 4.78 \text{ \AA}$ , which matches very well the  $4.2 \text{ \AA}$  thick interface layer observed at DTS. In contrast to one methyl-hydrogen pointing into the interface layer at OTS, two methyl-hydrogens are present in the interface layer of the tilted DTS. Additionally, the interface layer at DTS is thinner than the OTS one and hence, the proportional amount of protonated silane should be considerably higher at the DTS, at the expense of the relative amount of deuterated PS. This is well in accord with the  $43 \%$  silane and  $32 \%$  *d*PS as revealed by NR for the DTS interface.

The interfacial liquid structure which we deduce from our scattering experiments is in line with recent MD simulations, where a crystalline surface induced order in polymeric liquids [23]: The first liquid layer showed an almost perfect reproduction of the preset periodic crystal structure. Recent experiments confirm that in thin polymer films chain segments may order [24] and, in particular, that certain orientations of the PS phenyl rings can be induced by the presence of interfaces, even in absence of specific interactions: As demonstrated by non-linear optical techniques such as sum-frequency generation (SFG) spectroscopy, the interplay of intra- and intermolecular interactions causes the phenyl rings to point away from the bulk polymer film perpendicular to the polymer/air interface [25] and also towards a hydrophobic substrate [26].

However, the slip lengths observed in MD studies are on

the order of several monomer lengths [23] and are not comparable to the large experimental slip lengths (up to several  $\mu\text{m}$  close to  $T_g$ ) for unentangled polymer melts on silanized surfaces [15]. Experimental slip lengths, therefore, may incorporate apparent slip in addition to real slip. Apparent slip of polymeric liquids may be explained by a higher segmental mobility in the vicinity of the interface, either (i) due to an interfacial depletion effect [6] or (ii) due to a layering [27] and/or alignment [7] of the liquid near the interface or (iii) due to a reduced segmental friction coefficient between the adjacent (and probably immobile) polymer chains and the residual polymer film caused by particular polymer conformations near interfaces.

The structural data of our study imply a flat arrangement of the adjacent PS chain segments and a sharp step in the density profile between the interfacial layer and the residual polymer film. The density was shown to be reduced down to 75 - 77% in a depletion zone of 4 - 7 Å thickness. Mechanism (i) does not apply to our system since the small extent of the depletion zone cannot account for the large experimental slip lengths measured. Regarding mechanism (ii), apparent slip due to layering implies more than one layer of polymer to be aligned. However, density oscillations indicating such molecular layering were not detected, but might become observable in *in situ* experiments while applying shear flow [28]. Our experiments clearly demonstrate a distinct orientation of the phenyl rings of the PS melt due to the structural properties of the adjacent substrate (OTS and DTS). Hence, compared to the non-oriented bulk liquid, it seems reasonable to expect locally deviating dynamical properties such as friction and viscosity in the interfacial region.

In literature, experimentally observed differences in slip length of Newtonian liquids on different substrates have been widely attributed to surface properties such as roughness and the strength of interaction between liquid molecules and the substrate [29]. We stress the fact that these parameters are found to be identical for PS on DTS and on OTS. For these systems we provide evidence of a molecular interplay of the liquid's interfacial structure and the surface order, affecting a macroscopically detectable parameter: slippage of an unentangled polymer film on silanized surfaces. MD simulations investigating slippage of polymer melts, therefore, should intend to account for the entire monomeric structure of the polymers to achieve comparability to experimental situations.

In summary, we have revealed that surface order of a SAM affects the conformation of polymer chain segments adjacent to the solid boundary. The results of combined x-ray and neutron scattering studies point out that chain segments lie completely flat and, moreover, that the SAM structure is replicated within the first polymer layer. This seems to be the crucial parameter determin-

ing a) substantially different polymer slippage on SAMs exhibiting apparently identical properties and b) large effective (comprising real and apparent) slip, both observed experimentally. Our findings corroborate on-going research claiming conformational changes at the interface in case of polymeric liquids [14] and the interfacial liquid structure in case of Newtonian liquids as the main origin of slip [11, 30, 31]. Additionally, our results might also shed light on further interfacial phenomena such as depletion layers or glass-transition temperatures of thin polymer films.

We gratefully acknowledge financial support by the BMBF (05K10PC1), the DFG grants ZA161/18 and JA905/3 within the priority program (SPP) 1164 and the graduate school GRK1276.

---

\* gutfreund@ill.eu

† o.baemchen@physik.uni-saarland.de

‡ Present address: Karlsruhe Institute of Technology, Institute for Pulsed Power and Microwave Technology, 76344 Eggenstein-Leopoldshafen, Germany

- [1] T. M. Squires and S. R. Quake, *Rev. Mod. Phys.* **77**, 977 (2005).
- [2] H. D. Rowland, W. P. King, J. B. Pethica, and G. L. W. Cross, *Science* **322**, 720 (2008).
- [3] C. L. M. H. Navier, *Mem. Acad. Sci. Inst. Fr.* **6**, 389 (1823).
- [4] C. Neto *et al.*, *Rep. Prog. Phys.* **68**, 2859 (2005); E. Lauga, M. P. Brenner, and H. A. Stone, in *Springer Handbook of Experimental Fluid Mechanics*, edited by C. Tropea, A. L. Yarin, and J. F. Foss (Springer, 2007); L. Bocquet and J.-L. Barrat, *Soft Matter* **3**, 685 (2007).
- [5] S. Granick, Y. Zhu, and H. Lee, *Nature Mater.* **2**, 221 (2003).
- [6] E. Ruckenstein and P. Rajora, *J. Colloid Interface Sci.* **96**, 488 (1983).
- [7] S. Heidenreich, P. Ilg, and S. Hess, *Phys. Rev. E* **75**, 066302 (2007).
- [8] M. Maccarini, *Biointerphases* **2**, MR1 (2007) and references therein.
- [9] B. M. Ocko, A. Dhinojwala, and J. Daillant, *Phys. Rev. Lett.* **101**, 039601 (2008); A. Poynor *et al.*, *ibid.* **101**, 039602 (2008); M. Mezger *et al.*, *J. Am. Chem. Soc.* **132**, 6735 (2010).
- [10] S. Chattopadhyay *et al.*, *Phys. Rev. Lett.* **105**, 037803 (2010).
- [11] P. Gutfreund *et al.*, *J. Chem. Phys.* **134**, 064711 (2011).
- [12] D. M. Huang *et al.*, *Phys. Rev. Lett.* **101**, 226101 (2008).
- [13] C. Bollinne *et al.*, *Macromolecules* **32**, 4719 (1999).
- [14] O. Bäumchen, R. Fetzer, and K. Jacobs, *Phys. Rev. Lett.* **103**, 247801 (2009).
- [15] R. Fetzer *et al.*, *Phys. Rev. Lett.* **95**, 127801 (2005); *Langmuir* **23**, 10559 (2007); O. Bäumchen *et al.*, in *Proceeding of the IUTAM Symposium on Advances in Micro- and Nanofluidics*, edited by M. Ellero *et al.* (Springer, 2009).
- [16] J. B. Brzoska, I. B. Azouz, and F. Rondelez, *Langmuir* **10**, 4367 (1994).

- [17] C. Krywka *et al.*, J. Synchrot. Radiat. **13**, 8 (2006).
- [18] M. Wolff, K. Zhernenkov, and H. Zabel, Thin Solid Films **515**, 5712 (2007).
- [19] A. Nelson, J. Appl. Crystallogr. **39**, 273 (2006).
- [20] The error bars given by the fit correspond to one standard deviation, whereas the parameter ranges indicated in this work correspond to the variation among two measurements of equal samples from different batches.
- [21] I. M. Tidswell *et al.*, Phys. Rev. B **41**, 1111 (1990).
- [22] J. M. Crissman *et al.*, J. Appl. Crystallogr. **3**, 194 (1970).
- [23] N. V. Priezjev, Phys. Rev. E **82**, 051603 (2010).
- [24] S. Rivillon, P. Auroy, and B. Deloche, Phys. Rev. Lett. **84**, 499 (2000).
- [25] K. S. Gautam *et al.*, Phys. Rev. Lett. **85**, 3854 (2000).
- [26] P. T. Wilson *et al.*, Chem. Phys. Lett. **363**, 161 (2002).
- [27] P. A. Thompson and M. O. Robbins, Phys. Rev. A **41**, 6830 (1990); N. V. Priezjev and S. M. Troian, Phys. Rev. Lett. **92**, 018302 (2004); Y. Zhu and S. Granick, *ibid.* **93**, 096101 (2004).
- [28] M. Wolff, A. Magerl, and H. Zabel, Physica B **350**, 196 (2004).
- [29] R. Pit, H. Hervet, and L. Léger, Phys. Rev. Lett. **85**, 980 (2000); Y. Zhu and S. Granick, *ibid.* **88**, 106102 (2002); L. Léger, J. Phys.: Condens. Matter **15**, S19 (2003); T. Schmatko, H. Hervet, and L. Léger, Langmuir **22**, 6843 (2006).
- [30] J.-L. Barrat and L. Bocquet, Faraday Discuss. **112**, 119 (1999).
- [31] T. Schmatko, H. Hervet, and L. Léger, Phys. Rev. Lett. **94**, 244501 (2005).

# C. Shear Induced Relaxation of Polymer Micelles at the Solid-Liquid Interface

*Langmuir* **24**, 11331-11333 (2008)

Authors: M. WOLFF<sup>1,2</sup>, R. STEITZ<sup>3</sup>, P. GUTFREUND<sup>1,2</sup>, N. VOSS<sup>4</sup>, S. GERTH<sup>4</sup>, M. WALZ<sup>4</sup>, A. MAGERL<sup>4</sup>, H. ZABEL<sup>1</sup>

<sup>1</sup>Ruhr-Universität Bochum, 44780 Bochum, Germany

<sup>2</sup>Institut Laue-Langevin, BP 156, 38042 Grenoble, France

<sup>3</sup>Helmholtz Centre Berlin for Materials and Energy, Hahn-Meitner-Platz 1, 14109 Berlin, Germany

<sup>4</sup>Lehrstuhl für Kristallographie und Strukturphysik, Universität Erlangen-Nürnberg, 91058 Erlangen, Germany

*Author contributions: M. Wolff, M. Walz and A. Magerl designed research. The samples were prepared by N. Voss, M. Wolff, P. Gutfreund and S. Gerth. The experiments were performed by P. Gutfreund and S. Gerth under the supervision of M. Wolff and R. Steitz. Data analysis was performed by M. Wolff and P. Gutfreund. The article was written by M. Wolff.*

## Shear Induced Relaxation of Polymer Micelles at the Solid–Liquid Interface

Max Wolff,<sup>\*,†</sup> Roland Steitz,<sup>‡</sup> Philipp Gutfreund,<sup>†</sup> Nicole Voss,<sup>§</sup> Stefan Gerth,<sup>§</sup>  
Marco Walz,<sup>§</sup> Andreas Magerl,<sup>§</sup> and Hartmut Zabel<sup>†</sup>

*Institute for Experimental Physics/Solid-State Physics/EP IV, Ruhr-University Bochum,  
D-44780 Bochum, Germany, Helmholtz Centre Berlin for Materials and Energy, Glienickerstr. 100,  
D-14109 Berlin, Germany, and Crystallography and Structural Physics, University of Erlangen-Nürnberg,  
Staudtstr. 3, D-91058 Erlangen, Germany*

Received June 20, 2008. Revised Manuscript Received September 10, 2008

A 20% aqueous solution of (ethylene oxide)<sub>99</sub>–(propylene oxide)<sub>65</sub>–(ethylene oxide)<sub>99</sub>, F127, was investigated by combining rheology in a cone/plate-geometry and surface-sensitive grazing incident neutron scattering. The crystalline structure formed by the polymer micelles becomes less pronounced for low shear rates, but correlations increase for higher shear rates. After stopping shear a slow relaxation of the micelles is found in the vicinity (50 μm thick layer) of a hydrophilic silicon wall (strong micelle–wall interaction), while a fast relaxation is observed in the boundary layer against the hydrophobic silicon wall (weak micelle–wall interaction). The results show that in the vicinity of the interface wall–particle interactions compete heavily with the shear force acting on the liquid.

Mixtures of amphiphilic block copolymers with a selective solvent are known to form various structures.<sup>1</sup> At moderate and high concentrations, micelles develop and may crystallize in face centered cubic (fcc) or hexagonal (hex) structures with unit cells in the range of several up to hundreds of nanometers. Applying external fields such as shear can dramatically change the overall structure of the sample. In most cases, crystallites become aligned. Also, secondary Bragg peaks are detected that were explained by a finite coherence of the crystalline structure.<sup>2</sup> A second possibility to introduce anisotropy is by bringing a solution in contact with a solid wall.<sup>3</sup> Well-suited methods for monitoring the near surface region over many orders of magnitude in length scales (from nanometers up to micrometers) are small angle scattering and reflectometry.<sup>4,5</sup> Except for some recent grazing incident small angle neutron scattering (GISANS)<sup>6,7</sup> and small-angle X-ray scattering (GISAXS)<sup>8,9</sup> measurements under shear, only transmission experiments on bulk systems were conducted on an in situ combination of rheology and small angle scattering measurements.<sup>10–15</sup> An issue of practical interest is

that the self-ordering of polymeric systems at the interface and under shear is widely used to template nanomaterials.<sup>16–20</sup> In this letter, we combine GISANS with neutron reflectometry (in particular, diffuse scattering) and rheology. It turns out that the crystallinity of a micellar solution depends on the interface properties as well as on shear. Furthermore, different relaxation processes for recovering the crystalline structure after shear are found depending on the coating of the solid surface.

As a sample, a 20% (in weight) aqueous solution of the Pluronic F127 ((ethylene oxide)<sub>99</sub>–(propylene oxide)<sub>65</sub>–(ethylene oxide)<sub>99</sub>) was used. The bulk properties of this material are known in great detail.<sup>21</sup> The polymer was purchased from Sigma-Aldrich and used without further purification. For the neutron scattering experiment, the molecules were solved in deuterated water, for better contrast, at low temperatures of 6 °C under constant stirring until a homogeneous solution was formed. The sample was then filled into the sample cell in its liquid state ( $T < 20$  °C) to prevent preshearing of the crystalline phase. The solid walls were activated with SiO<sub>2</sub>-terminated (hydrophilic) and hexamethyldisilazan (HMDS)-coated silicon wafers (hydrophobic), respectively. The SiO<sub>2</sub>-terminated wafer was cleaned with Carroic acid and showed a contact angle of water of less than 10°. The HMDS-coated silicon wafer was prepared by cleaning in Carroic acid and subsequent placement in HMDS vapor for 24 h and showed a contact angle of water of around 90°.

The scattering experiments were done with the V6 reflectometer at BENSC (Helmholtz Centre Berlin for Materials and Energy,

\* Corresponding author. E-mail: v-wolff@ill.eu. Present address: Institute Laue-Langevin, BP 156, F-38042 Grenoble Cedex 9, France. Tel.: +33-476207981. Fax: +33-476207120.

† Ruhr-University Bochum.

‡ Helmholtz Centre Berlin for Materials and Energy.

§ University of Erlangen-Nürnberg.

(1) Alexandritsis, P.; Lindman, B. *Amphiphilic Block Copolymers*, 1st ed.; Elsevier Science: Amsterdam, 2000; p 1.

(2) Förster, S.; Timmann, A.; Schellbach, C.; Förmsdorf, A.; Kornowski, A.; Weller, H.; Roth, S. V.; Lindner, P. *Nat. Mater.* **2007**, *6*, 888.

(3) Wolff, M.; Magerl, A.; Zabel, H. *Thin Solid Films* **2007**, *515*, 5724.

(4) Wolff, M.; Scholz, U.; Hock, R.; Magerl, A.; Leiner, V.; Zabel, H. *Phys. Rev. Lett.* **2004**, *92*, 255501.

(5) Wolff, M.; Magerl, A.; Zabel, H. *Euro. Phys. J. E* **2005**, *16*(2), 141.

(6) Wolff, M.; Magerl, A.; Zabel, H. *Physica B* **2005**, *357*, 84.

(7) Hamilton, W. A.; Butler, P. D.; Magid, L. J.; Han, Z.; Slawecski, T. M. *Phys. Ref. E* **1999**, *60*, R1146.

(8) Timmann, A.; Roth, S. V.; Fischer, S.; Förster, S. *Appl. Phys. Lett.* **2007**, *91*, 213102.

(9) Moulin, J. F.; Roth, S. V.; Müller-Buschbaum, P. *Rev. Sci. Instrum.* **2001**, *72*, 4305.

(10) Hamley, I. W. *Phil. Trans. R. Soc. London, Ser. A* **2001**, *359*, 1017.

(11) Panine, P.; Gradzielski, M.; Narayanan, T. *Rev. Sci. Instrum.* **2003**, *74*, 2451.

(12) Habas, J.-P.; Pavie, E.; Perreux, C.; Lapp, A.; Peyrelasse, J. *Phys. Rev. E* **2004**, *70*, 061802.

(13) Mortensen, K. *J. Polym. Sci., Part B: Polym. Phys.* **2004**, *42*, 3092.

(14) Förster, S.; Konrad, M.; Lindner, P. *Phys. Rev. Lett.* **2005**, *94*, 017803.

(15) Polushkin, E.; Bondzic, S.; De Wit, J.; Ekenstein, G. A.; Dolbnya, I.; Bras, W.; Ikkala, O.; ten Brinke, G. *Macromolecules* **2005**, *38*, 1804.

(16) Ludwigs, S.; Boker, A.; Voronov, A.; Rehse, N.; Magerle, R.; Krausch, G. *Nat. Mater.* **2003**, *2*, 744.

(17) Register, R. A. *Nature (London)* **2003**, *424*, 378.

(18) Kim, S. O.; Solak, H. H.; Stoykovich, M. P.; Ferrier, N. J.; de Pablo, J. J.; Nealey, P. F. *Nature (London)* **2003**, *424*, 411.

(19) Rosa, C.; Park, C.; Thomas, E. L.; Lotz, B. *Nature (London)* **2000**, *405*, 433.

(20) Cheng, J. Y.; Ross, C. A.; Thomas, E. L.; Smith, H. I.; Vancso, G. J. *Appl. Phys. Lett.* **2002**, *81*, 3657.

(21) Mortensen, K. *Polym. Adv. Technol.* **2001**, *12*, 2.

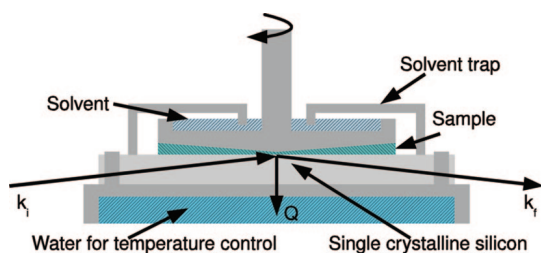


**Figure 1.** Sketch of the experimental setup with the rheometer mounted on the sample stage of V6. Neutrons enter a single crystalline block of silicon on the narrow side and get scattered from the bottom of the solid–liquid interface.

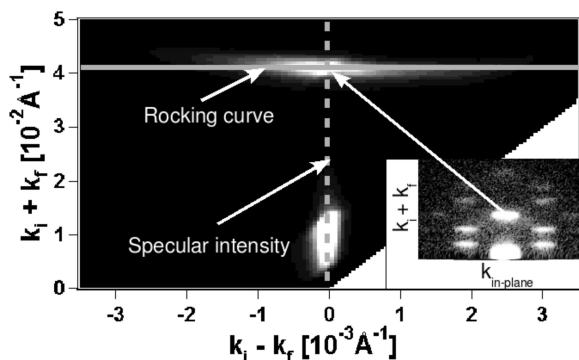


**Figure 2.** Reflectivity and diffuse scattering as collected for a sample forming a fcc structure (cubic close packing) close to a solid interface. The dashed and solid lines mark the specular reflectivity and the Rocking curve, respectively. The panel on the bottom right depicts a GISANS pattern reflecting the symmetry of the unit cell.

Berlin, Germany) using a neutron wavelength of 4.66 Å. This instrument offers the possibility of horizontal sample geometry and allows to scatter from the bottom of the liquid in contact with a silicon wafer underneath. Accordingly, no sealing is needed that may contaminate the sample. The scattering geometry is shown in Figure 1. For checking the symmetry of the unit cell first, always a grazing incident small angle scattering pattern was taken. For all experimental conditions, we found a more or less pronounced cubic close packing at the silicon interface which is well in line with previous studies.<sup>4</sup> Subsequently, rocking scans, with a resolution of  $\Delta(k_i - k_f) = 6.5 \times 10^{-4} \text{ \AA}^{-1}$ , on the first-order specular reflection were taken before, during,<sup>22</sup> and after shearing the sample. Neutron reflectometry and grazing incident SANS are surface-sensitive techniques. By varying the incident beam angle in the given setup, a depth of up to 50  $\mu\text{m}$  in the liquid close to the interface is probed.

To allow the shear experiment in a controlled manner, a commercially available rheometer (Bohlin CSR-10) was modified to fit the requirements of a neutron reflectometry study and mounted on the sample stage of V6. Neutrons collimated to a rectangular cross section of  $6 \times 1 \text{ mm}^2$  enter a single crystalline silicon block,  $70 \times 70 \times 10 \text{ mm}^3$ , on the narrow side ( $70 \times 10$ ) and get then reflected at the bottom of the liquid sample. To avoid evaporation of solvent, a trap is implemented confining the sample in a closed volume (Figure 1). The temperature was controlled by water circulating from a water bath kept at 20 °C for all measurements.

Figure 2 shows the intensity (the white and black color symbolize high and low intensity, respectively) plotted over  $k_i - k_f$  and  $k_i + k_f$ , where  $k_i$  and  $k_f$  denote the momentum of the

incident and scattered neutrons, respectively. The specular reflectivity is found along the vertical dashed gray line. The area of total reflection, reflected by high intensity, is visible on the bottom in the middle close to  $k_i - k_f = 0$ . The pronounced reflection visible at  $k_i + k_f \approx 0.04 \text{ \AA}^{-1}$  is the first-order Bragg reflection on the specular line corresponding to the (111) reflection in the fcc structure (cubic close packing).<sup>4</sup> The symmetry of the unit cell was determined by taking a complementary GISANS pattern (panel inserted on the bottom right of Figure 2).<sup>23</sup> On the  $x$ -axis,  $k_{\text{in-plane}}$  denotes the momentum transfer in the plane of the interface and out of the scattering plane for the reflectivity measurement. To explain all reflections, a cubic close packing with random orientation of the crystallites in the plane of the sample surface has to be assumed.<sup>4</sup>

The left panel (a) in Figure 3 shows the Rocking curve (intensity normalized to the incident beam intensity) of the first-order specular reflection taken in-plane with the Pluronic F127 dissolved in D<sub>2</sub>O, against the hydrophilic silicon wafer. The micelles of this sample are already known to form a cubic dense packing close to a solid interface.<sup>4</sup> From Figure 3a, it is clearly visible that shear has a strong influence on the line shape of the (111) reflection. An initially (without shear) narrow line representing a lateral correlation length of some micrometers becomes clearly broadened under shear as seen from the reduced peak intensity. This is explained by a reduction in the correlation length and seems to be in contradiction to the known shear alignment of micellar crystals.<sup>24</sup> This fact can be explained by assuming a global alignment of crystallites under shear, but at the same time, a less well-defined lattice constant as the sample is not in equilibrium and relates well to the explanation of secondary Bragg reflections given recently.<sup>2</sup> For increasing shear rates, we find a slightly increasing diffuse scattering. With the sample at the hydrophobic interface, qualitatively a similar behavior is found.

The right panel (b) in Figure 3 depicts the intensity (normalized to the incident beam intensity) distribution of the same reflection after stopping shear. Clearly, two components have to be separated. The narrow one is related to scattering from the mean potential along the interface normal and represents the specular reflected intensity on a large length scale. The broad, background-like one reflects the correlations in the fluctuations parallel to the interface on a much shorter length scale. It turns out that the narrow component increases with time, while the broad one remains more or less unchanged. This is explained by the fact that the micelles form a more and more layered structure close to the interface without changing the lateral correlations or crystallite size. This manifests in the sharp and narrow peak visible at  $k_i - k_f = 0$ , while the diffuse background remains constant. A closer look reveals that the intensity of the narrow peak increases continuously with time. This result is in contrast to the study of Hamilton et al. on a CTAB solution where a decay of the crystalline structure was found after stopping Poiseuille shear flow.<sup>7</sup>

To extract information on the relaxation of the long-range orientational correlations (or layering) after stopping shear at the different interfaces, the integrated intensity of the (111) reflection can be defined as order parameter. One single Gaussian line with fixed position, width (resolution limited), and background was fitted to the narrow component visible in panel (b) of Figure 3. The result is depicted in Figure 4 where the order parameter

(22) Data during shear were taken for 15 min after preshearing of the sample for 60 s to reach the steady state.

(23) The GISANS scattering pattern shown was corrected for refractive distortion. Further information on data correction in GISANS measurements can be found in, e.g.: Hamilton, W. A.; Butler, P. D.; Hayter, J. B.; Magid, L. J.; Kreke, P. J. *Physica B* **1996**, *221*, 309.

(24) Eiser, E.; Molino, F.; Porte, G.; Diat, O. *Phys. Rev. E* **2000**, *61*, 6759.

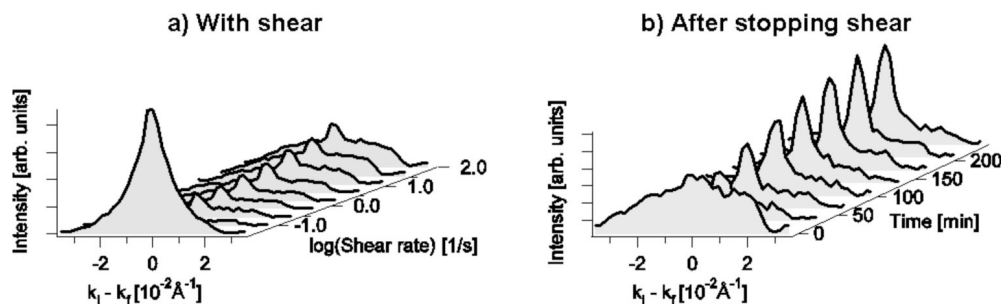


**Figure 3.** Panel on the left side (a) depicts Rocking curves for the (111) reflection measured for different shear rates, and the panel on the right side (b) shows the change in the Rocking curve with time after stopping the shear with the sample at the hydrophilic wafer.

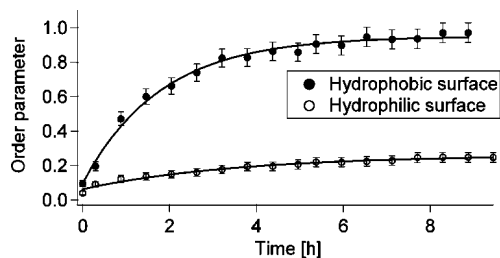


**Figure 4.** Intensity of the narrow component (specular intensity) plotted versus time after stopping the shear taken with the sample in contact with a hydrophilic and a hydrophobic substrate.

(intensity normalized to the peak intensity before shearing the sample) for the two different interfaces is plotted versus time. The micelles rearrange on a time scale of several hours. All measurements were repeated at least once to check for reproducibility of the result. The open and closed symbols represent data for the hydrophilic and the hydrophobic interface, respectively. The lines correspond to an exponential fit ( $1 - e^{-(t/\tau)}$ ) to the data with a decay time  $\tau$ . It turns out that the relaxation of the polymer micelles is dependent on the properties of the solid wall. For the hydrophobic interface,  $\tau$  is found to be about 2 h, whereas for the hydrophilic one, 5 h is extracted. In addition, the extrapolation for infinite times shows that only 25% of the initial (before shearing) intensity is recovered for the hydrophilic interface, whereas at the hydrophobic one the crystal relaxes completely.

(25) Gerstenberger, M. C.; Pedersen, J. S.; Smith, G. S. *Phys. Rev. E* **1998**, *58*, 8028.

The micellar corona is more hydrophilic than the core, and the interaction of the micelles with a hydrophilic interface is stronger.<sup>4,25,26</sup> This implies a tighter binding of micelles at this interface and explains the slower relaxation. On the hydrophobic wall, on the opposite, one expects weaker wall–micelle interactions and thus faster relaxation. This is in line with results that are reported for many systems showing surface slip where generally a larger slip length (faster motion of particles) is found close to an interface with weak interaction.<sup>27</sup>

In summary, we have shown the usefulness in combining rheology with grazing incident small angle neutron scattering and reflectometry. By this technique, new information on the crystallization and rearrangement of polymer micelles in the vicinity of solid–liquid interfaces with different surface treatments becomes accessible. For a strong micelle–surface interaction, we find a slower relaxation than for a weaker one. We expect research following along the presented line to contribute to a deeper understanding of crystallization. Additionally, our work will have an impact on the optimization in templating of nanostructures.

**Acknowledgment.** We gratefully acknowledge financial support from the BMBF (03ZA7BOC) and the DFG grants MA801/12-1 and ZA161/18-1 within the priority program (SPP) 1164.

LA801945Q

(26) Gerstenberger, M. C.; Pedersen, J. S.; Majewski, J.; Smith, G. S. *Langmuir* **2002**, *18*, 4933.

(27) Neto, C.; Evans, D. R.; Bonaccorso, E.; Butt, H.-J.; Craig, V. S. J. *Rep. Prog. Phys.* **2005**, *68*, 2859.

# D. Nanoscale Discontinuities at the Boundary of Flowing Liquids: A Look into Structure

*Journal of Physics: Condensed Matter*, **23**, 184102 (2011)

Authors: M. WOLFF<sup>1</sup>, P. GUTFREUND<sup>2,3</sup>, A. RÜHM<sup>4,5</sup>, B. AKGUN<sup>6,7</sup>, H. ZABEL<sup>2</sup>

<sup>1</sup>Material Science, Department of Physics, Uppsala University, 75121 Uppsala, Sweden

<sup>2</sup>Ruhr-Universität Bochum, 44780 Bochum, Germany

<sup>3</sup>Institut Laue-Langevin, BP 156, 38042 Grenoble, France

<sup>4</sup>Max Planck Institut für Metallforschung, 70569 Stuttgart, Germany

<sup>5</sup>Forschungs-Neutronenquelle Heinz Maier-Leibnitz, 85748 Garching, Germany

<sup>6</sup>National Institute of Standards and Technology, Gaithersburg MD 20899, USA

<sup>7</sup>Department of Material Science and Engineering, University of Maryland - College Park, MD 20742, USA

*Author contributions: M. Wolff and P. Gutfreund designed research. The samples were prepared by B. Akgun and P. Gutfreund. The experiments were performed by P. Gutfreund under the supervision of M. Wolff, B. Akgun and A. Rühm. Data analysis was performed by M. Wolff and P. Gutfreund. The article was written by M. Wolff and P. Gutfreund under the supervision of H. Zabel.*

# Nanoscale discontinuities at the boundary of flowing liquids: a look into structure

Max Wolff<sup>1</sup>, Philipp Gutfreund<sup>2,3</sup>, Adrian Rühm<sup>4,5</sup>,  
Bulent Akgun<sup>6,7</sup> and Hartmut Zabel<sup>2</sup>

<sup>1</sup> Department of Physics and Astronomy, Uppsala University, Uppsala 75121, Sweden

<sup>2</sup> Lehrstuhl für Festkörperphysik/EP IV, Ruhr-Universität Bochum, Bochum 44780, Germany

<sup>3</sup> Institute Laue-Langevin, Grenoble 38042, France

<sup>4</sup> Max Planck Institut für Metallforschung, Stuttgart 70569, Germany

<sup>5</sup> Forschungs-Neutronenquelle Heinz Maier-Leibnitz, Garching 85748, Germany

<sup>6</sup> National Institute of Standards and Technology, Gaithersburg, MD 20899, USA

<sup>7</sup> Department of Material Science and Engineering, University of Maryland—College Park, MD 20742, USA

E-mail: [max.wolff@fysik.uu.se](mailto:max.wolff@fysik.uu.se)

Received 24 May 2010, in final form 12 October 2010

Published 20 April 2011

Online at [stacks.iop.org/JPhysCM/23/184102](http://stacks.iop.org/JPhysCM/23/184102)

## Abstract

When downsizing technology, confinement and interface effects become enormously important. Shear imposes additional anisotropy on a liquid. This may induce inhomogeneities, which may have their origin close to the solid interface. For advancing the understanding of flow, information on structures on all length scales and in particular close to the solid interface is indispensable. Neutron scattering offers an excellent tool to contribute in this context. In this work, surface sensitive scattering techniques were used to resolve the structure of liquids under flow in the vicinity of a solid interface. Our results are summarized as follows. First, for a Newtonian liquid we report a depletion distance on the order of nanometers which is far too small to explain the amount of surface slip, on the order of micrometers, found by complementary techniques. Second, for a grafted polymer brush we find no entanglement–disentanglement transition under shear but the grafted film gets ripped off the surface. Third, by evaluating the local structure factor of a micellar solution close to the solid interface it turns out that the degree of order and local relaxation depends critically on the surface energy of the solid surface.

(Some figures in this article are in colour only in the electronic version)

## 1. Introduction

In classic fluid mechanics flow is described by the Navier–Stokes equation in the bulk and a no-slip boundary condition at the solid interface [1], which is in agreement with many macroscopic experimental observations [2]. However, recently both experiments and theory have shown that on a microscopic scale liquids may undergo significant slip at a solid wall [3, 4]. This boundary slip modifies the velocity profile most drastically within a short distance from the interface given by the slip length  $b$  which is defined as the distance beyond the solid interface where the flow profile of

the liquid extrapolates to zero:

$$b = \lim_{z \rightarrow 0} v(z) (\partial v(z) / \partial z)^{-1}, \quad (1)$$

where  $v$  denotes the velocity of the liquid and  $z$  is the distance from the interface. By now it is accepted that intrinsic slip may exist on a smooth homogeneous solid–liquid interface. For simple liquids the slip length extends at most over some tens of nanometers, but may be up to micrometers for polymers and seems to be larger for a non-wetting surface. However, as yet there is no quantitative understanding of the connection between the structure of the liquid–solid interface and its friction properties.

Two scenarios have to be distinguished. In the case of real slip the liquid slides over the solid interface on an atomic scale. This implies either very high shear rates [4] or a roughness of the solid boundary which is laterally on a vastly different length scale in comparison to the liquid molecules' size [5]. The second scenario for moderate shear is apparent slip over molecularly smooth surfaces. In this case, a microscopic boundary layer is assumed which is different structurally and/or dynamically from the bulk liquid. The boundary layer leads to a different viscosity and is observed as surface slip on a larger length scale, although the no-slip boundary condition is still valid microscopically.

To explain apparent slip two models are under discussion. The first one assumes a microscopic layer with depleted density of the liquid near the solid interface [6]. Depletion layers at liquid/solid interfaces have been observed in various cases [7] using x-ray (XRR) and neutron reflectometry (NR), but have only recently been recorded *in situ* under shear load [8, 9] with NR. An alternative explanation suggests the alignment of the near surface molecules as a consequence of shear stress [10]. This interpretation relates well to a larger slip length observed for hexadecane compared to squalane, which is a more symmetric molecule [11]. The surface-induced molecular layering of flowing liquids has been observed in confined propanol [12] using a surface force apparatus, and in eicosane [13] using an atomic force microscope after quenching the flowing alkane. However, these techniques are either indirect or require direct contact with the interfacial liquid and thus may perturb the system.

In the case of polymers the discussion of the slip length becomes more complicated, as it is known from rheology that the viscosity depends on the shear rate. The measured stress shows a plateau as a function of shear rate. In the stress plateau, the fluid may be inhomogeneous with the shear band structure varying systematically with the applied shear rates. Entangled polymer solutions and melts, however, have been understood to exhibit shear thinning characteristics without becoming inhomogeneous. At a sufficiently high stress (typically ca. 0.3 MPa), well-entangled melts may display an interfacial stick-slip transition (SST) where the apparent flow rate jumps discontinuously, due to a massive wall slip. This behavior also shows up in highly entangled polymer solutions [14]. The molecular origin of SST has been proposed to arise from the disentanglement of adsorbed chains on the wall from the freely flowing chains. In order to verify this proposition we have investigated polystyrene (PS) melts in contact with a grafted PS film. This is an interesting case as the no-slip boundary condition is enforced.

In this contribution our recent findings on the near surface structure of liquids under flow are summarized. In the first part a neutron reflectivity study on the Newtonian liquid hexadecane will be presented, followed by a second study on a polymer melt, PS in contact with a grafted layer of chemically identical polymer. Lastly, we will present results about the structural arrangements of surfactant micelles in contact with the surfaces of different interfacial energies and under shear load. Our results will be compared to the amount of surface slip found by complementary techniques.

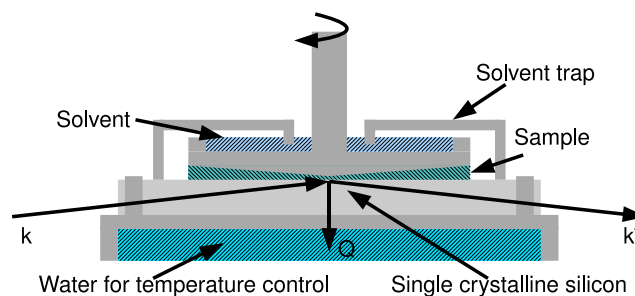


**Figure 1.** Sketch of the experimental setup. Neutrons enter a single crystalline block of silicon on the narrow side and get scattered from the bottom of the solid-liquid interface [15].

## 2. Experimental details

In order to measure the reflectivity of the solid/liquid interface while shearing the liquid *in situ*, a shear device or rheometer with a cone/plate geometry was mounted onto the sample stage of the neutron instruments. We used a scattering geometry in which the neutron beam passes through the silicon substrate and is reflected downwards from the horizontal solid/liquid interface. The sample geometry is sketched in figure 1 and is described in more detail previously [8, 15, 16]. The vertically collimated neutron beam enters a  $70 \times 70 \times 10 \text{ mm}^3$  single crystalline silicon block on the narrow side and then gets reflected from the bottom of the liquid sample.

## 3. Newtonian liquids

In this section the density profile and near surface structure of hexadecane will be brought into context with surface slip.

### 3.1. Samples, measurements and data evaluation

Two functionalized single crystalline silicon (100) substrates ( $70 \text{ mm} \times 70 \text{ mm} \times 10 \text{ mm}$  optically polished, obtained from *CrysTec*<sup>8</sup>, Germany) were used for this experiment. In order to provide a high surface energy one of the two wafers was chemically cleaned in freshly prepared Piranha solution 50/50 v/v  $\text{H}_2\text{SO}_4$  (concentrated) and  $\text{H}_2\text{O}_2$  (30% aqueous)<sup>9</sup> resulting in a completely wetting surface with an interfacial energy of approx.  $\gamma_{sl} = 34.35 \text{ mJ m}^{-2}$  [7, 17]. In order to provide a lower surface energy the second silicon wafer was cleaned by the same method and then chemically grafted with an octadecyl trichlorosilane (OTS) monolayer, resulting in an interfacial energy of  $\gamma_{sl} = 7.2 \text{ mJ m}^{-2}$ . The surface energy was determined from contact angle measurements. The resulting advancing contact angle of hexadecane on the OTS surface was  $40^\circ \pm 2^\circ$  at  $22^\circ\text{C}$ . The contact angle error corresponds to variations on different spots on the surface. The contact angle hysteresis was always smaller than  $2.8^\circ$ .

<sup>8</sup> Commercial materials, instruments and equipment are identified in this paper in order to specify the experimental procedure as completely as possible. In no case does such identification imply a recommendation or endorsement nor does it imply that the materials, instruments, or equipment identified are necessarily the best available for the purpose.

<sup>9</sup> Corrosive. Acid-resistant gloves, protective goggles, and lab coats must be worn when handling the Piranha solution.

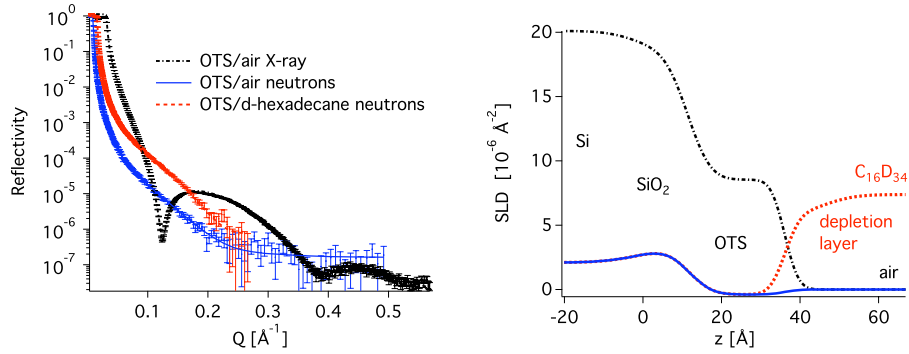


**Figure 2.** Left panel: neutron (blue solid line) and x-ray (black dash-dotted line) reflectivity curves of the bare silicon wafer covered with OTS; NR for the same substrate in contact with static d-hexadecane at 22 °C (red dashed line), with the neutron beam impinging from the silicon side. The straight, dotted and dashed lines represent the best fits to the data points. Right panel: SLD profiles corresponding to fits [9].

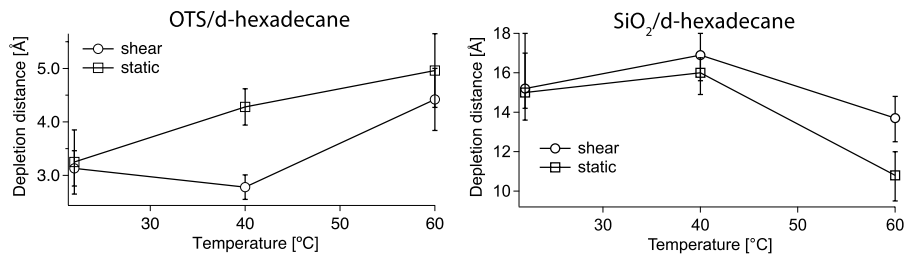


**Figure 3.** Depletion distances calculated from the fitted SLD profiles of the OTS/d-hexadecane and SiO<sub>2</sub>/d-hexadecane interface (left and right panel, respectively) [9].

In most precedent neutron reflectometry studies on surface slip a spin coated PS film was used for the low energy surface, providing a thick layer giving rise to oscillations in the reflectivity at low  $Q$ -values. However, it turns out that directly spin coated physisorbed PS films on a silicon wafer are not stable during a flow experiment and thus chemical grafting is necessary [18].

The NR measurements on fully deuterated hexadecane (deuteration > 98.4%, purity 98.9% from Polymer Source (see footnote 8), Montreal, Canada) were performed on the Liquids Reflectometer at the Spallation Neutron Source in Oak Ridge, Tennessee, USA. The bare substrates were characterized by means of x-ray reflectometry. Fitting of the reflectivity data was accomplished using the co-refinement of a slab model with Motofit [19]. The substrate structures were determined by simultaneously fitting the x-ray and neutron reflectivities of the bare substrates in air. A depletion layer was modeled using an additional layer with reduced liquid density.

### 3.2. Results

The reflectivity curves of the bare substrate as well as the reflectivity curve of the static d-hexadecane/OTS interface at room temperature are shown in figure 2. A two slab model for an OTS layer, consisting of the hydrocarbon tail and the silicon oxide layer was sufficient to obtain a consistent fit for the x-ray and neutron data [20].

According to our fitting the thickness, the scattering length density (SLD) and the contact angle of the OTS layer stayed

invariant throughout the experiment even after two days of exposure to deuterated hexadecane.

In order to fit the reflectivity of the OTS/d-hexadecane interface shown in figure 2, a density depleted layer had to be assumed. For a quantitative comparison of the depletion effect the so called depletion distance  $d_2$  [21] is introduced:

$$d_2 = \int_{\text{liquid phase}} \left( 1 - \frac{\rho(z)}{\rho_{\text{bulk}}} \right) dz, \quad (2)$$

where  $\rho(z)$  denotes the density of the depleted liquid at a distance  $z$  from the interface and  $\rho_{\text{bulk}}$  represents the bulk liquid density.  $d_2$  represents the thickness of an equivalent depleted layer of zero density.

The depletion distance calculated for the case of the OTS interface at 22 °C is  $3.25 \pm 0.6 \text{ \AA}$ . At this temperature the subsequent application of shear at  $500 \text{ s}^{-1}$  does not change the depletion distance within the error. Increasing the temperature to 60 °C enhances the depletion to  $d_2 = 5 \pm 0.69 \text{ \AA}$  as shown in figure 3 (left panel). Here the depletion distance decreases to  $4.4 \pm 0.58 \text{ \AA}$  when shear is applied. On the other hand, at the wetting interface, only a model with a considerably more extended depletion fits the data well. The calculated depletion distances as a function of shear and temperature are plotted in figure 3 (right panel). The reflectivities from which these values were extracted are not shown.

### 3.3. Discussion

At both interfaces we observe a layer with reduced hexadecane density. In the case of the OTS coated surface, the resulting

depletion distances range from 3.25 to 5 Å, whereas at the bare silicon substrate, considerably larger depletion distances of about 10–18 Å are observed. These results match well with previously measured values on similar systems [7, 8].

According to the literature, the slippage of hexadecane should be less pronounced in the case of higher energy surfaces [4]. Surface force apparatus (SFA) based studies even report no slip in the case of complete wetting. Hence the density depletion observed in this study cannot be the origin of the surface slip, as it is significantly larger for hexadecane at the high energy surface. Assuming the interfacial layer as a density depleted layer only, the slip length  $b$ , as introduced in equation (1), can be calculated from the near surface density profile of the liquid [22]:

$$b = \int_{\text{liquid phase}} \left( \frac{\rho_{\text{bulk}}}{\rho(z)} - 1 \right) dz. \quad (3)$$

The calculated slip lengths of flowing hexadecane at 22 °C are  $4.6 \pm 0.6$  Å for the OTS surface and  $41 \pm 7$  Å for the SiO<sub>2</sub> boundary. These values are in sharp contrast to the reported experimental hexadecane slip lengths of 200–4000 Å on OTS and 0–1750 Å on completely wetting surfaces [4]. Thus, in addition to the opposite trend of the depletion effect, the magnitude of the slip length resulting from our data under the assumption of equation (3) is considerably smaller than those reported in the literature.

Consequently our observation, that shear enhances the depletion at the wetting interface and decreases it in the case of low interfacial energy, points at different structural rearrangements, e.g. molecular alignment, that take place at the interface under shear stress.

### 3.4. Grazing incidence diffraction

In order to evaluate the feasibility of grazing incident diffraction (GID) experiments with neutrons [23, 24], to address the structural arrangement of hexadecane molecules close to the solid boundary, we have calculated the expected signal to noise ratio for a typical setup of deuterated liquid in contact with a silicon wafer.

$$\frac{\text{signal}}{\text{noise}} = \frac{\sigma_{\text{hd}}^{\text{coh}} \rho_{\text{hd}}^{\text{At}} V_{\text{hd}}}{\sigma_{\text{hd}}^{\text{inc}} \rho_{\text{hd}}^{\text{At}} V_{\text{hd}} + \sigma_{\text{Si}}^{\text{inc}} \rho_{\text{Si}}^{\text{At}} V_{\text{Si}}}. \quad (4)$$

Here  $\sigma$ ,  $\rho^{\text{At}}$  and  $V$  denote the scattering cross section, atomic density and illuminated volume, respectively. The superscripts coh and inc symbolize values for coherent and incoherent scattering and the indices hd and Si specify values for deuterated hexadecane and silicon, respectively. Calculating the signal to noise ratio for the respective numbers and scattering volumes for an incident beam angle of 0.25°, below the critical angle of total external reflection (penetration depth into the hexadecane: 3.5 nm), and 0.5°, above the critical angle of total external reflection (penetration depth into the hexadecane: 22.4 μm), results in  $5.64 \times 10^{-3}$  and 2.17, respectively.

Figure 4 depicts the result of a grazing incidence neutron scattering study of crystalline hexadecane in contact with a

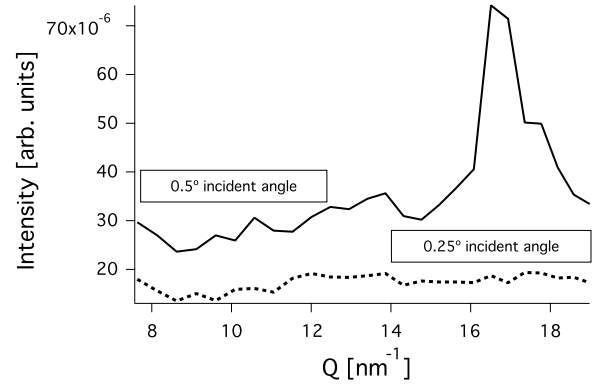


**Figure 4.** Grazing incidence diffraction data recorded with a sample of crystalline hexadecane in contact with a silicon wafer.

silicon wafer for incident beam angles below (0.25°) and above (0.5°) the critical angle of total external reflection. The experiment was done using the instrument N-REX<sup>+</sup> at the FRM-2, Munich (Germany). This instrument allows in-plane scattering up to large  $Q$  values. The peak at 70° arises from the crystalline hexadecane. The intensity of this peak for an incident angle above the critical angle of total reflection is indeed comparable to the background as expected from the calculations. Below the angle of total reflection the background decreases but the peak is not visible any more either. Resolving a peak with a signal to noise ratio of  $10^{-3}$  would be very time consuming on currently available neutron scattering instruments.

## 4. Polymer melts

For polymers the slip length can be much larger than for Newtonian liquids. An interesting case is obtained when the first layer of polymer molecules is grafted to the solid surface and thus the non-slip boundary condition is strictly enforced.

### 4.1. Experimental details

X-ray reflectivity measurements on the grafted PS films were carried out using a Bruker D8 (see footnote 8) Advance x-ray reflectometer (XR), before and after shearing the sample. The beam width was 10 mm and the beam height was 0.1 mm.

Polystyrene was purchased from Polymer Source Inc. (see footnote 8) and used without further characterization. Four PS brushes of high grafting density ( $\approx 0.6$  chains nm<sup>-2</sup>) with different thicknesses were synthesized. A detailed description of the preparation of the PS brushes can be found in the appendix. Here we will only explain the results for two of these samples. The first sample is a 20 nm thick grafted layer of deuterated PS (d8-PS) in contact with a hydrogenated 3 kg mol<sup>-1</sup> PS melt and the second sample has a 33 nm thick grafted hydrogenated PS film in contact with d8-PS with a molecular mass of  $M_n = 2.2$  kg mol<sup>-1</sup>. Deuterated samples were prepared in order to provide a good contrast for neutron scattering studies. However, in this paper we concentrate on the x-ray reflectivity measured before and after shearing the

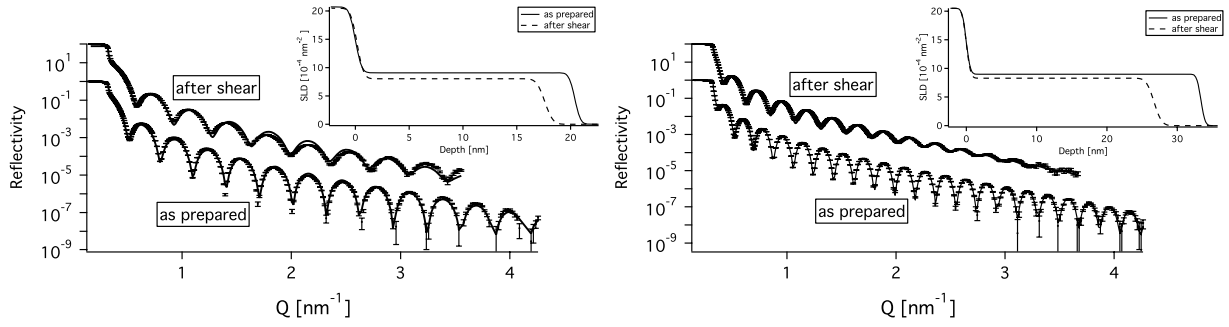


**Figure 5.** X-ray reflectivity as a function of wavevector for a 20 nm thick d-PS brush (left) and 33 nm thick PS brush (right) measured after the synthesis and after applying shear and cleaning the brushes. The solid lines show fits to the data. The corresponding SLD profiles are shown in the insets.

**Table 1.** Result of the x-ray fitting parameters obtained for the two brushes before and after shearing the sample. SLD and  $\rho_n$  PS denote the scattering length density for x-rays and the number density of PS monomers, respectively.

	20 nm		33 nm	
	Before	After	Before	After
Thickness (nm)	$20.4 \pm 0.02$	$17.5 \pm 0.07$	$33.4 \pm 0.02$	$26.5 \pm 0.07$
Roughness (nm)	$0.43 \pm 0.031$	$0.68 \pm 0.053$	$0.47 \pm 0.012$	$0.86 \pm 0.08$
SLD ( $10^{-4} \text{ nm}^{-2}$ )	$9.0 \pm 0.4$	$8.0 \pm 0.4$	$9.0 \pm 0.2$	$8.3 \pm 0.3$
$\rho_n$ PS ( $\text{nm}^{-3}$ )	$5.7 \pm 0.2$	$5.1 \pm 0.2$	$5.7 \pm 0.1$	$5.3 \pm 0.2$

sample. We will discuss the *in situ* neutron measurements in a forthcoming paper.

The experimental procedure was as follows. First, the x-ray reflectivity was measured for all dry brush samples. Then the samples were placed on the plate of the shear device and were heated above the glass transition temperature up to 130 °C. Then the cone was put in place and the first sample was sheared for several hours at a shear rate of 60 s<sup>-1</sup>. Finally, the sample was sheared at 110 °C and then quenched during shear before the final x-ray measurements were done. The second sample was sheared for several hours at a rate of 300 s<sup>-1</sup> but without quenching. At last the x-ray reflectivity was recorded at room temperature. Before taking the final x-ray reflectivity data both substrates were sonicated in toluene at 60 °C for 3 h to remove residual PS melt from the grafted chains.

#### 4.2. Experimental data

In order to characterize the substrates before and after shearing, the x-ray reflectivity of the two films was recorded as depicted in figure 5. The solid line is a fit to the data obtained with Motofit [19]. The extracted SLDs, roughnesses and thicknesses are summarized in table 1. The SLD of the silicon substrate was  $20.5 \times 10^{-4} \text{ nm}^{-2}$  and the roughness was 0.5 nm. It turns out that the film thickness for both samples decreased by about 20% upon shearing while the roughness increased by roughly 50%. The lower quality of the fit for the 20 nm film in the region between 1.5 and 2.5 nm<sup>-1</sup> is attributed to macroscopic roughening of the film. This roughening is optically visible. As the measurements were conducted with a constant beam width, for different  $Q$  values different portions of the sample surface were illuminated. In order to reproduce

the reflectivity even in the presence of macroscopic changes of the film morphology, an incoherent sum of intensities would be necessary which is not included in our model. However, this would only bring minor changes into the quantitative result of our experiment and does not affect the qualitative discussion.

#### 4.3. Result

A possible degradation of polymer melts and solutions under shear stress has been known for some time [25]. For polymer solutions the degradation seems not to depend on the viscosity of the solvent, demonstrating that it is an entanglement effect [26]. Degradation is found for sufficiently high deformations and high shear rates overcoming the local segmental relaxation times of the polymer molecules [27]. However, for our experiments the shear rates of up to 300 s<sup>-1</sup> are far too low to be comparable to the local relaxation time of the molecules being on the order of ns. One may thus assume the solid–liquid interface to be the weak point for fracture, and in fact a huge surface slip is expected for highly entangled polymer systems. Nevertheless in our case polymer chains are chemically grafted to the solid interface through covalent bonds, which enforces the non-slip boundary condition, in comparison to physisorption.

It is important to note that the PS melts used in this study (2.2 and 3 kg mol<sup>-1</sup>) are composed of relatively short chains far below the entanglement length (18 kg mol<sup>-1</sup>, 163 monomers per chain [28]). From our previous experience we know that grafted PS films, prepared in the way described above, are stable in contact with static PS melts.

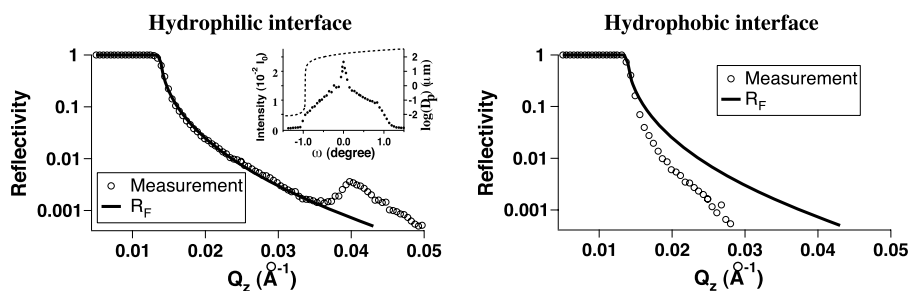


**Figure 6.** Reflectivity data taken with the sample in the liquid phase in contact with a hydrophilic (left panel) and a hydrophobic (right panel) interface compared to the Fresnel-reflectivity  $R_F$ . For the hydrophilic interface a reflection from adsorbed micelle layers is visible at  $Q_z = 0.04 \text{ \AA}^{-1}$ . The inset in the left panel shows a rocking scan of this reflection. The dashed line represents the calculated neutron penetration depth [31].

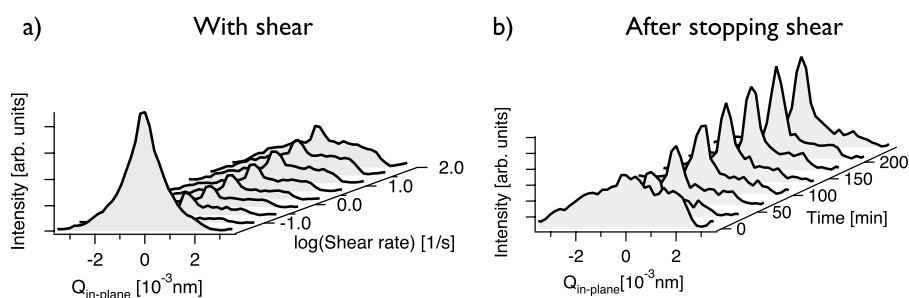


**Figure 7.** The panel on the left side (a) depicts rocking curves for the (111) reflection measured for different shear rates and the panel on the right side (b) shows the change in the rocking curve with time after stopping the shear with the sample at the hydrophilic wafer [15].

## 5. Multiphase systems

Multiphase polymer systems may self-assemble on mesoscopic length scales. This introduces correlations on larger length scales and allows grazing incidence scattering studies at low  $Q$  values.

The sample, Pluronic F127 (EO<sub>99</sub>-PO<sub>65</sub>-EO<sub>99</sub>), was obtained from BASF Wyandotte Corp. (New Jersey, USA) (see footnote 8) and used without further purification. The bulk properties of similar samples are known in great detail [29, 30]. Pluronics have a core of propylene oxide (PO) with two terminations of ethylene oxide (EO) and can self-assemble in aqueous solutions. The resulting aggregations have a hydrophobic core and a hydrophilic shell. For high concentrations or temperatures the micelles crystallize in a fcc structure.

For our experiment F127 was diluted up to 20% (by weight) in deuterated water.

To evaluate the effect of different surface energies on the crystallization, two single crystalline polished silicon discs were investigated as solid interfaces. One was oxidized for 15 min in a 5:1 mixture of H<sub>2</sub>SO<sub>4</sub> and H<sub>2</sub>O<sub>2</sub> resulting in a hydrophilic SiO<sub>2</sub> termination (contact angle of water 33°). The second substrate was cleaned with the same mixture of acids and a deposition by exposure to gaseous HMDS (1,1,1,3,3,3-hexamethyldisilazane) was made for 24 h to achieve a relatively hydrophobic termination (contact angle of water 75°).

### 5.1. Effect of the interface

Figure 6 shows the specular reflected intensity taken with the sample in the liquid phase at 22 °C at the hydrophilic (left panel) and the hydrophobic (right panel) interfaces. Both data sets are compared to the Fresnel-reflectivity. The data are corrected for the small angle scattering. At  $Q_z = 0.04 \text{ \AA}^{-1}$ , the intensity is increased for the hydrophilic interface, showing layers of adsorbed micelles. A similar effect has been reported earlier [32]. For the hydrophobic interface the reflectivity drops faster than  $R_F$  and no peak is visible. This indicates a huge interface roughness and no adsorption of micelles. The inset in the left panel shows the rocking curve, including the small angle scattering, taken at  $Q_z = 0.04 \text{ \AA}^{-1}$ , for the hydrophilic interface. The narrow peak at  $\omega = 0$  is resolution limited and represents in-plane correlations over a length scale exceeding  $60 \mu\text{m}$ . The broad component arises from the liquid structure factor of the bulk sample.

### 5.2. Near surface relaxation of micelles

The left panel (a) in figure 7 shows the rocking curve (normalized to the incident beam intensity) with the Pluronic F127 dissolved in D<sub>2</sub>O, at the hydrophilic silicon wafer. Data of the first order specular reflection ( $Q_z = 0.04 \text{ \AA}^{-1}$ ) were taken in-plane scanning along the Bragg rod found in the diffuse or off specular scattering. From figure 7(a), it is clearly visible that shear has a strong influence on the line shape of the (111) reflection. An initially (without shear) narrow line representing a lateral correlation length of about

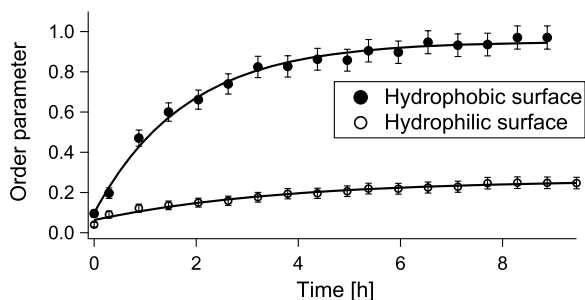


**Figure 8.** Intensity of the narrow component (specular intensity) plotted versus time after stopping the shear taken with the sample in contact with a hydrophilic and a hydrophobic substrate [15].

5  $\mu\text{m}$  becomes clearly broadened under shear as seen from the reduced peak intensity. This fact can be explained by assuming a global alignment of crystallites under shear but at the same time a worse defined lattice constant as the sample is not in equilibrium and relates well to the explanation of secondary Bragg reflections given recently [33]. These secondary Bragg reflections are reflections not lying on the Ewald sphere but can be excited due to the relatively huge broadening of the peaks due to small crystals and large mosaicity.

The right panel (b) in figure 7 depicts the rocking curve (normalized to the incident beam intensity) of the same reflection after stopping shear. It turns out that the specular component increases with time while the diffuse one remains more or less unchanged. This is explained by the fact that the micelles form a more and more layered structure close to the interface without changing the lateral correlations or crystallite size. To extract information on the relaxation of the long range orientational correlations (or layering) after stopping shear at the different interfaces the integrated intensity of the (111) reflection can be defined as an order parameter. The result is depicted in figure 8 where the order parameter (intensity normalized to the peak intensity before shearing the sample) for the two different interfaces is plotted versus time. The micelles rearrange on a timescale of several hours. The open and closed symbols represent data for the hydrophilic and the hydrophobic interface, respectively. It turns out that the relaxation of the polymer micelles is dependent on the properties of the solid wall. For the hydrophobic interface a relaxation time of 2 h is found whereas for the hydrophilic one 5 h are extracted. In addition, the extrapolation for infinite times shows that only 25% of the initial (before shearing) intensity is recovered for the hydrophilic interface whereas at the hydrophobic one the crystal relaxes completely [15]. However, the crystallinity at the hydrophilic interface is generally of a higher quality and the intensities of the Bragg reflections were normalized to the values found before applying any shear. The micellar corona is more hydrophilic than the core and the interaction of the micelles with a hydrophilic interface is stronger [31, 32, 34]. This implies a tighter binding of micelles at this interface and explains the slower relaxation. On the hydrophobic wall, on the contrary, one expects weaker wall–micelle interactions and thus faster relaxation [15].

## 6. Conclusions

Our results relate the near surface structure in liquids to surface slip. The measurements on hexadecane clearly rule out the explanation of surface slip by assuming a density depleted layer only. The experiments on micellar solutions show different structures at surfaces with different surface energies. Additionally the reconstruction of these structures after shear depends on the surface energy of the substrate. To summarize, a microscopic description of surface slip on an atomic length scale has to incorporate the local density of the liquid near the surface as well as the local structure and dynamics of the molecules.

## Acknowledgments

The authors acknowledge the help of S Gerth, H Wacklin, R Campell, J F Ankner, C Halbert, J Browning, S K Satija, G Ugur and R Steitz during the various neutron scattering experiments, M D Foster for the use of his dry box, the DFG (grant no.: Za161-18-2) and the Swedish research council (travel grant no.: 90045401) for financial support.

## Appendix. Grafting of PS brushes

The grafted PS films were prepared following the procedure described earlier [35]. Silicon wafers ( $70 \times 70 \times 10 \text{ mm}^3$ ) were cleaned by treatment with a freshly prepared piranha solution (see footnote 9) (70/30, v/v, concentrated  $\text{H}_2\text{SO}_4$ /30% aqueous  $\text{H}_2\text{O}_2$ ) at 90–100 °C for 1 h and were then rinsed with distilled water and dried in a stream of technical grade nitrogen. The surface-bound initiator was deposited by solution deposition. A  $100 \times 100 \text{ mm}^2$  glass container was used both for the initiator deposition and polymerization. A freshly cleaned silicon wafer was placed inside a custom made Teflon gasket in such a way that the polished face was facing against the solution in the glass container. (11-(2-bromo-2-ethyl) propionyloxy)undecyltrichlorosilane was synthesized according to the literature [36] and utilized as a surface-bound initiator. Dry toluene (30 ml) and a 25 vol% solution of the trichlorosilane initiator in toluene (0.6 ml) were added to the dish via syringe and the dish was subsequently covered with a piece of glass carrying the Teflon gasket and kept for 4 h at 60 °C. The silicon wafer was then removed, sequentially washed with toluene, ethanol and methylene chloride, and then dried in a stream of compressed air. The procedure for surface initiated atom transfer radical polymerization (ATRP) from a flat silicon substrate was as follows: CuBr, anisole and deuterated styrene (d8-S) were added to a 100 ml Schlenk flask with a magnetic stir bar, sealed with a rubber septum and degassed by purging with technical grade nitrogen for 2 h. Three vacuum/purge cycles were applied to the flask and it was subsequently kept under a nitrogen atmosphere. Pentamethyldiethylenetriamine (PMDETA) was added to the mixture via syringe and the solution was stirred at reaction temperature until it became homogeneous ( $\approx 5$  min). Then the flask was sealed and transferred to the dry box along with the free initiator (ethyl-2-bromoisobutyrate, E2Br-iB), the silicon

wafer and a glass container. The polymerization solution was added to the glass container and the silicon wafer was placed into the solution with the Teflon, followed by the addition of the free initiator. The final concentrations were as follows:  $[d8-S]_0 = 3.9$  M,  $[PMDETA]_0 = 25$  mM,  $[CuBr]_0 = 12$  mM and  $[Br - iB]_0 = 5$  mM. The dish was covered with a piece of glass carrying the Teflon gasket to prevent evaporation of the solution. The polymerization proceeded at 90–100 °C for a period of time depending on the thickness targeted. To remove untethered polymer chains, the silicon wafers were sonicated in hot toluene for 8 h.

The density of the grafted layers was determined in the following way:

$\rho = N_A h / M_n$ , where  $M_n$  is the average molecular weight,  $N_A$  is Avogadro's number,  $h$  is the dry thickness of the polymer brush layer and  $\rho$  is the bulk mass density which is  $1.05$  g cm<sup>-3</sup> for PS.  $M_n$  is obtained from the GPC measurements of free polymer chains grown in the solution at the same time when the grafted chains are growing from the initiator immobilized on the substrate. It has already been shown that for ATRP, NMP and RAFT synthesis techniques the molecular weight and polydispersity of grafted and free chains grown at the same time in the same polymerization solution are very close to each other. They found that the difference is usually less than 5% [37–39]. The dry thickness of the brush layer,  $h$ , is determined very accurately using both ellipsometry and x-ray reflectivity.

## References

- [1] Faber T E 1995 *Fluid Dynamics for Physicists* (Cambridge: Cambridge University Press)
- [2] Feynman R 1995 *Lectures on Physics* (Reading, MA: Addison-Wesley)
- [3] Neto C et al 2005 Boundary slip in Newtonian liquids: a review of experimental studies *Rep. Prog. Phys.* **68** 2859
- [4] Lauga E, Brenner M P and Stone H A 2005 *Microfluidics: The No-Slip Boundary Condition* (New York: Springer)
- [5] Galea T M and Attard P 2004 Molecular dynamics study of the effect of atomic roughness on the slip length at the fluid–solid boundary during shear flow *Langmuir* **20** 3477–82
- [6] Trethewey D C and Meinhardt C D 2004 A generating mechanism for apparent fluid slip in hydrophobic microchannels *Phys. Fluids* **16** 1509–15
- [7] Maccarini M, Steitz R, Himmelhaus M, Fick J, Tatur S, Wolff M, Grunze M, Janeczek J and Netz R R 2007 Density depletion at solid–liquid interfaces: a neutron reflectivity study *Langmuir* **23** 598–608
- [8] Wolff M, Akgun B, Walz M, Magerl A and Zabel H 2008 Slip and depletion in a Newtonian liquid *Europhys. Lett.* **82** 1–5
- [9] Gutfreund P, Wolff M, Maccarini M, Gerth S, Ankner J F, Browning J, Halbert C E, Wacklin H and Zabel H 2010 Depletion at solid–liquid interfaces: flowing hexadecane on functionalized surfaces *J. Chem. Phys.* submitted
- [10] Barrat J L and Bocquet L 1999 Influence of wetting properties on hydrodynamic boundary conditions at a fluid/solid interface *Faraday Discuss.* **112** 119–27
- [11] Schmatko T, Hervet H and Leger L 2005 Friction and slip at simple fluid–solid interfaces: the roles of the molecular shape and the solid–liquid interaction *Phys. Rev. Lett.* **94** 980–3
- [12] Sun G X, Bonaccorso E, Franz V and Butt H J 2002 Confined liquid: simultaneous observation of a molecularly layered structure and hydrodynamic slip *J. Chem. Phys.* **117** 10311–4
- [13] Drummond C, Alcantar N and Israelachvili J 2002 Shear alignment of confined hydrocarbon liquid films *Phys. Rev. E* **66** 1–6
- [14] Leger L 2003 Friction mechanisms and interfacial slip at fluid–solid interfaces *J. Phys.: Condens. Matter* **15** S19
- [15] Wolff M, Steitz R, Gutfreund P, Voss N, Gerth S, Walz M, Magerl A and Zabel H 2008 Shear induced relaxation of polymer micelles at the solid–liquid interface *Langmuir* **24** 11331
- [16] Wolff M, Magerl A and Zabel H 2005 Structure of polymer micelles close to the solid interface *Eur. Phys. J. E* **16** 141–5
- [17] Lim S C, Kim S H, Lee J H, Kim M K, Kim D J and Zyung T 2005 Surface-treatment effects on organic thin-film transistors *Synth. Met.* **148** 75–9
- [18] van der Grinten D, Wolff M, Zabel H and Magerl A 2008 Flow cell for grazing incidence neutron scattering *Meas. Sci. Technol.* **19** 034016
- [19] Nelson A 2006 Co-refinement of multiple-contrast neutron/x-ray reflectivity data using MOTOFIT *J. Appl. Crystallogr.* **39** 273
- [20] Tidswell I M, Ocko B M, Pershan P S, Wasserman S R, Whitesides G M and Axe J D 1990 X-ray specular reflection studies of silicon coated by organic monolayers (alkylsiloxanes) *Phys. Rev. B* **41** 1111–28
- [21] Mamatkulov S I, Khabibullaev P K and Netz R R 2004 Water at hydrophobic substrates: curvature, pressure, and temperature effects *Langmuir* **20** 4756–63
- [22] Vinogradova O I 1995 Drainage of a thin liquid film confined between hydrophobic surfaces *Langmuir* **11** 2213
- [23] Ankner J F, Zabel H, Neumann D A and Majkrzak C F 1989 Grazing-angle neutron diffraction *Phys. Rev. B* **40** 7928
- [24] Dosch H 1992 *Springer Tracts Mod. Phys.* vol 126 (Berlin: Springer) p 1
- [25] Bestul A B 1956 Kinetics of capillary shear degradation in concentrated polymer solutions *J. Chem. Phys.* **24** 1196
- [26] Nguyen T Q and Kausch H K 1990 Effects of solvent viscosity on polystyrene degradation in transient elongational flow *Macromolecules* **23** 5137
- [27] Nguyen T Q and Kausch H K 1988 Chain scission in transient extensional flow kinetics and molecular weight dependence *J. Non-Newton. Fluid Mech.* **30** 125
- [28] Rubinstein M and Colby R 2003 *Polymer Physics* (New York: Oxford University Press)
- [29] Mortensen K 2001 Structural properties of self-assembled polymeric aggregates in aqueous solutions *Polym. Adv. Technol.* **12** 2–22
- [30] Mortensen K, Batsberg W and ren Hvidt S 2008 Effects of peo-ppo diblock impurities on the cubic structure of aqueous peo-ppo-peo pluronic . . . *Macromolecules* **41** 1720
- [31] Wolff M, Scholz U, Hock R, Magerl A, Leiner V and Zabel H 2004 Crystallization of micelles at chemically terminated interfaces *Phys. Rev. Lett.* **92** 255501
- [32] Gerstenberg M C, Pedersen J S and Smith G S 1998 Surface induced ordering of micelles at the solid–liquid interface *Phys. Rev. E* **58** 8028–31
- [33] Förster S, Timmann A, Schellbach C, Frömsdorf A, Kornowski A, Weller H, Roth S V and Lindner P 2007 Order causes secondary bragg peaks in soft materials *Nature Mater.* **6** 888–93
- [34] Eiser E, Molino F, Porte G and Diat O 2000 Nonhomogeneous textures and banded flow in a soft cubic phase under shear *Phys. Rev. E* **61** 6759–64
- [35] Akgun B, Ugur G, Brittain W J, Majkrzak C F, Li X, Wu D T, Wang Q and Foster M D 2009 Internal structure of ultrathin diblock copolymer brushes *Macromolecules* **42** 8411

- [36] Matyjaszewski K *et al* 1999 Polymers at interfaces: using atom transfer radical polymerization in the controlled growth of homopolymers and block copolymers from silicon surfaces in the absence of untethered sacrificial initiator *Macromolecules* **32** 8716
- [37] Ejaz M, Yamamoto S, Ohno K, Tsujii Y and Fukuda T 1998 Controlled graft polymerization of methyl methacrylate on silicon substrate by the combined use of the langmuir-blodgett and atom transfer radical polymerization techniques *Macromolecules* **31** 5934
- [38] Husseman M *et al* 1999 Controlled synthesis of polymer brushes by living free radical polymerization techniques *Macromolecules* **32** 1424
- [39] Baum M and Brittain W J 2002 Synthesis of polymer brushes on silicate substrates via reversible addition fragmentation chain transfer technique *Macromolecules* **35** 610

# Acknowledgments

First of all I thank my supervisors Dr. Max Wolff, Dr. Marco MacCarini and Prof. Dr. Dr. h. c. Hartmut Zabel for giving me the possibility to perform this work and for their constant assistance. Special thanks to Dr. Max Wolff for never letting me alone during the *various* neutron scattering experiments and for the good advises that he always gave, not only concerning science.

Next, I thank my co-workers from the University of Erlangen-Nürnberg: Stefan Gerth, Nicole Voss, Marco Walz and Prof. Dr. Andreas Magerl, for their nice collaboration and the fruitful discussions. Especially the neutron and x-ray scattering experiments performed together with Stefan Gerth were very funny and a real pleasure for me.

I acknowledge the productive and very nice collaboration with Dr. Oliver Bäumchen, Dr. Renate Fetzner and Prof. Dr. Karin Jacobs. Their motivation and competent help gave me confidence and broadened my scientific knowledge.

I am also thankful for the sincere assistance of Dr. Roland Steitz, Dr. Adrian Rühm, Dr. Bulent Akgun, Dr. John F. Ankner, Candice E. Halbert, Dr. Jim Browning, Dr. Hanna Wacklin and Dr. Richard Campbell during the NR experiments. Especially the collaboration with Dr. Roland Steitz and Dr. Bulent Akgun was very enjoyable and prosperous.

Moreover I thank my colleagues at the ILL, Kirill Zhernenkov and Dr. Anton Devishvili, who produced a very nice working atmosphere and Dorothee van der Grinten, who introduced me into the subject and to everyday life in Grenoble. I appreciate useful discussions and advices of Prof. Dr. Boris Toperverg, especially concerning off-specular reflection.

Many thanks to my parents Dr. Ludmilla and Waldemar Gutfreund, who gave me the possibility to study physics at all and supported me financially, especially during the first year of my stay in Grenoble.

Finally the biggest thanks to my wife Iryna Gorun, who incredibly ameliorated my life and constantly motivated and supported me in my scientific career and helped me to find the right English words for this thesis.

This work was financed by the BMBF (05K10PC1), the DFG (ZA161/18) within the priority program (SPP) 1164, and by the ILL through the PhD-student fellowship. A portion of this research was performed at Oak Ridge National Laboratory's Spallation Neutron Source, and sponsored by the Scientific User Facilities Division, Office of Basic Energy Sciences, U. S. Department of Energy.



# Curriculum Vitæ

# Philipp Gutfreund

Institut Laue - Langevin  
Large Scale Structures  
B.P. 156  
F - 38042 Grenoble Cedex 9

France

Phone: +33 476 207048  
Mobile: +33 622 235576  
Fax: +33 476 207120  
mail: gutfreund@ill.eu



## Personal

Date of birth: 06/12/1982  
Place of birth: Frankfurt am Main, Germany  
Nationality: German  
Marital status: married

## School

1989 - 1993 Primary School Süd-West Schule in Eschborn, Germany  
1993 - 2002 Albert-Einstein-Gymnasium in Schwalbach/Ts.,  
Germany  
Abitur (Average grade 1,9)

## Military Service

07/2002 - 9/2002 Military service in Schwalmstadt, Germany  
10/2002 - 3/2003 Motocar/tank technician in Mainz, Germany

## Education

4/2003 - 7/2007 Technical University Darmstadt Darmstadt Darmstadt (Germany)

Diploma in physics (Average grade 1)

since 9/2007 Ruhr-University Bochum Bochum (Germany)  
and  
Institut Laue-Langevin Grenoble (France)

PhD in physics (Expected 05/2011)

## Research Experiences

2/2006 - 8/2007

Experimental condensed matter physics group  
Technical University Darmstadt, Germany

### Diploma Student

Responsibilities:

Dynamic and structural investigation of binary glass forming mixtures by means of Dielectric Spectroscopy, DSC and SAXS

since 9/2007

Institut Laue-Langevin Grenoble, France  
and  
Ruhr-University Bochum, Germany

### PhD Student

Responsibilities:

Structural and dynamical investigation of liquids at interfaces. Mainly by means of Neutron and X-Ray Reflectivity, Grazing Incidence Small Angle Neutron Scattering and Grazing Incidence Neutron Diffraction. Inelastic experiments performed on Time-Of-Flight and Three Axis instruments.

Participation in building of the neutron reflectometer Super-ADAM.

### Oral Presentations:

- 'Introduction in soft matter', Technical University Darmstadt, April 2005
- 'Decoherence in quantum systems', TU Darmstadt, December 2005
- 'Complex Dynamics in a Binary Glass Former investigated by Dielectric Spectroscopy', DPG Spring-Meeting Regensburg, March 2007
- 'Data analysis of inhomogeneous thin films investigated by Neutron Reflectometry', Scattering Weekend, Rhein Valley, May 2008
- 'The microscopic origin of surface slip: Shear alignment of Hexadecane', Scattering Weekend, University of Erlangen-Nürnberg, February 2009
- 'The microscopic origin of surface slip: Shear alignment of Hexadecane on solid surfaces', DPG Spring-Meeting Dresden, March 2009
- 'The microscopic origin of surface slip: Shear alignment of Hexadecane on solid surfaces', Soft Matter Café, ILL, Grenoble, June 2009
- 'The microscopic origin of surface slip: Shear alignment of Hexadecane on solid surfaces', Ruhr-University Bochum, June 2009
- 'The microscopic origin of surface slip: A neutron scattering study of flowing Hexadecane on solid surfaces', Ruhr-University Bochum, February 2010
- 'The microscopic origin of surface slip: Shear alignment of Hexadecane on solid surfaces', DPG Spring-Meeting Regensburg, March 2010
- 'The microscopic origin of surface slip: A neutron scattering study of flowing Hexadecane on solid surfaces', Student Clip Session, ILL, Grenoble, April 2010
- 'The microscopic origin of surface slip: A neutron scattering study of flowing Hexadecane on solid surfaces', Uppsala University, May 2010
- 'The microscopic origin of surface slip: A Neutron and X-Ray Reflectivity study of flowing liquids at solid interfaces', Super-ADAM Workshop, ILL, Grenoble, October 2010
- 'The microscopic origin of surface slip: A Neutron and X-Ray Reflectivity study of flowing liquids at solid interfaces', LSS Group Meeting, ILL, Grenoble, March 2011

### Poster Presentations:

- 'The microscopic origin of surface slip', Workshop Micro- and Nanofluidics, Bad Honnef, July 2008
- 'Shear induced relaxation of polymer micelles at the solid-liquid interface', Workshop Micro- and Nanofluidics, Bad Honnef, July 2008
- 'The microscopic origin of surface slip: Shear alignment of Hexadecane on solid surfaces', International Conference on Neutron Scattering, Knoxville, May 2009
- 'The microscopic origin of surface slip', Workshop Micro- and Nanofluidics, Bad Honnef, July 2009
- 'The microscopic origin of surface slip', Conference on Grazing Incident Small Angle Scattering, DESY Hamburg, September 2009
- 'The microscopic origin of surface slip', Workshop Micro- and Nanofluidics, Norderney, February 2010
- 'The microscopic origin of surface slip', Student Poster Session, ILL, March 2010
- 'The microscopic origin of surface slip', Student Poster Session, ILL, March 2011

### Courses:

- 'HERCULES Specialized Courses', ILL Grenoble, November 2008

### Awards:

- 1997 3<sup>rd</sup> place in the Main-Taunus-Kreis within the Mathematics-Competition of Hesse, Germany
- 2001 7<sup>th</sup> place in the group competition of the 'Day of Mathematics' in Rüsselsheim, Germany
- 2002 Award from the German Physical Society for excellence in physics

### Publications:

- 'Shear Induced Relaxation of Polymer Micelles at the Solid-Liquid Interface', M. Wolff, R. Steitz, P. Gutfreund et al., Langmuir, 24 (11331) 2008
- 'Two Glass-Transitions and Secondary Relaxations of Methyl-Tetrahydrofuran in a Binary Mixture', T. Blochowicz, S. Lusceac, P. Gutfreund, et al., J. Phys. Chem. B 115 (1623) 2011
- 'Depletion at Solid-Liquid Interfaces: Flowing Hexadecane on Functionalized Surfaces', P. Gutfreund, M. Wolff et al., J. Chem. Phys. 134 (64711) 2011
- 'Nanoscale discontinuities at the boundary of flowing liquids: A look into structure', M. Wolff, P. Gutfreund et al., J. Phys.: Cond. Mat. 23 (184102) 2011
- 'Surface Correlation Affects Liquid Order and Slip in a Newtonian Liquid', P. Gutfreund, O. Bäumchen, et al., Phys. Rev. Lett. (submitted)

### **IT Expertise**

- Windows, Mac, Linux, Office, iWork
- Java
- gnuplot, IGOR, Origin
- Latex

## **Languages**

- German (native)
- English (fluent)
- Russian (fluent)
- French (advanced)

## **Miscellaneous:**

- Former Member of the Youth Symphony Orchestra of Hesse, Germany



.....  
Name, Vorname

Versicherung gemäß § 7 Abs. 2 Nr. 5 PromO 1987

Hiermit versichere ich, dass ich meine Dissertation selbstständig angefertigt und verfasst und keine anderen als die angegebenen Hilfsmittel und Hilfen benutzt habe. Meine Dissertation habe ich in dieser oder ähnlicher Form noch bei keiner anderen Fakultät der Ruhr-Universität Bochum oder bei einer anderen Hochschule eingereicht.

Bochum, den .....

.....  
Unterschrift